

# Computer simulation of liquid metals

D K Belashchenko

DOI: 10.3367/UFNe.0183.201312b.1281

## Contents

<b>1. Introduction</b>	<b>1176</b>
<b>2. Methods of simulation</b>	<b>1177</b>
2.1 Interparticle interaction potentials; 2.2 Form of the potential in the embedded atom model and the choice of its parameters; 2.3 First principle calculations ( <i>ab initio</i> method)	
<b>3. Simulation of group I metals of the Periodic Table</b>	<b>1182</b>
3.1 Alkali metals; 3.2 Noble metals	
<b>4. Metals of group II of the Periodic Table</b>	<b>1196</b>
4.1 Magnesium; 4.2 Zinc; 4.3 Mercury	
<b>5. Metals of group III of the Periodic Table</b>	<b>1199</b>
5.1 Aluminum; 5.2 Gallium; 5.3 Thallium	
<b>6. Elements of group IV of the Periodic Table</b>	<b>1201</b>
6.1 Carbon; 6.2 Germanium; 6.3 Tin; 6.4 Lead	
<b>7. Elements of group V of the Periodic Table</b>	<b>1203</b>
7.1 Phosphorus; 7.2 Arsenic; 7.3 Antimony; 7.4 Bismuth	
<b>8. Elements of group VI of the Periodic Table</b>	<b>1204</b>
8.1 Selenium; 8.2 Tellurium	
<b>9. Transition metals</b>	<b>1204</b>
9.1 Iron; 9.2 Iron-based solutions. Earth's core; 9.3 Nickel; 9.4 Other metals	
<b>10. Comparison of results of calculated with different potentials</b>	<b>1210</b>
<b>11. Simulation of binary systems</b>	<b>1211</b>
<b>12. Conclusions</b>	<b>1211</b>
<b>References</b>	<b>1212</b>

**Abstract.** Methods for and the results of the computer simulation of liquid metals are reviewed. Two basic methods, classical molecular dynamics with known interparticle potentials and the *ab initio* method, are considered. Most attention is given to the simulated results obtained using the embedded atom model (EAM). The thermodynamic, structural, and diffusion properties of liquid metal models under normal and extreme (shock) pressure conditions are considered. Liquid-metal simulated results for the Groups I–IV elements, a number of transition metals, and some binary systems (Fe–C, Fe–S) are examined. Possibilities for the simulation to account for the thermal contribution of delocalized electrons to energy and pressure are considered. Solidification features of supercooled metals are also discussed.

**D K Belashchenko** National University of Sciences and Technology 'Moscow Institute of Steel and Alloys' (MISIS),  
Leninskii prosp. 4, 119049 Moscow, Russian Federation  
E-mail: dkbel@mail.ru

Received 9 April 2013, revised 26 June 2013  
*Uspekhi Fizicheskikh Nauk* **183** (12) 1281–1322 (2013)  
DOI: 10.3367/UFNr.0183.201312b.1281  
Translated by Yu V Morozov; edited by A Radzig

## 1. Introduction

The history of computer simulation modeling at the atomic level dates back to the 1940s when the first computers were created. However, a very strong impetus for the rapid development of research in this area was given in the 1950s by the advent of the Monte Carlo (MC) simulation method (N Metropolis, A and M Rosenbluth, A and E Teller [1], 1953)<sup>1</sup> and the invention of the molecular dynamics technique (B Alder and T Wainwright [3], 1957). The authors utilized various forms of pair potentials of interparticle interaction. The first computer models were rather small (e.g., 32 particles in the basic cube with periodic boundary conditions) and the interaction potentials rather simple (Lennard-Jones potential, hard-sphere and power potentials). Since then, this line of computer simulation research has been making rapid progress parallel to computer performance enhancement, and the size of up-to-date models amounts to many millions of particles [4]. Classical molecular dynamics (MD) became the principal method of simulation [5–8].

Another approach to computer simulation of condensed matter was proposed much later based on quantum-mechanical calculations. The combination of quantum-mechanical

<sup>1</sup> The invention of the Monte Carlo method is traced to 1949, when Nicholas Metropolis and Stanislaw Ulam published their paper entitled "The Monte Carlo method" [2].

calculations and the MD method (R Car and M Parrinello [9]) made it possible to construct atomic models without tapping specified potentials, because the interparticle forces are calculated from first principles, or *ab initio*. However, such models have thus far been small, containing a few dozen atoms. This method allows, inter alia, approximating interparticle forces by analytical expressions through data processing for a series of atomic models; potentials found in this way can then be used in the framework of MD.

MD simulation of crystalline and liquid (amorphous) metals has some peculiarities. In the case of crystals, it is important to determine a wide spectrum of structure-related properties, such as phase transition energy and energy of lattice defect formation, elasticity, and surface properties of differently oriented facets. Usually, good agreement between calculated and experimentally found properties is achieved at a certain temperature, e.g., absolute zero, but it may be absent at different temperatures. In the simulation of a liquid (isotropic) metal, the number of properties being considered is usually smaller (density, energy, bulk compression modulus, self-diffusion coefficient), but it is desirable that agreement between theory and experiment be obtained for a wide range of temperatures and pressures.

High-quality interparticle interaction potentials are especially needed to simulate melting and crystallization phenomena, when they must equally well describe solid and liquid phases.

The present review is focused on the problems of computer simulation of liquid metals in an equilibrium state. However, rapid changes in parameters are likely to make a system strongly nonequilibrium. Such situations happen when short (femto- or picosecond) laser pulses are incident on a medium or when fast-moving particles produce radiation damage tracks along their paths [10]. In this case, the electron subsystem falls out of equilibrium with the ionic subsystem. Such states may be characterized by two different temperatures: those of electrons and ions, the former being much higher than the latter. The two temperatures are equalized through time. A distinctive feature of this process is that electron temperature determines the effective interatomic potential and, thereby, the properties of the metal itself. The authors of Refs [11, 12] considered peculiarities of MD simulation in such a nonequilibrium system and proposed interparticle interaction potentials calculated from data obtained by the *ab initio* method. By way of example, the dependence of the melting point of gold on electronic temperature was revealed, and the laser ablation of gold and the deceleration of xenon atoms in uranium were investigated.

## 2. Methods of simulation

### 2.1. Interparticle interaction potentials

Computer calculations by the MD and MC methods do not take much time if interparticle interactions are described by the respective analytical or tabulated potentials. An ordinary desktop computer can be used unproblematically to work with models containing tens of thousands of particles. A parallel computing technique is needed to work with models involving over hundreds of thousands of particles. However, such large models are necessary only to solve specific problems, like those of elucidation of phase transition mechanisms, studying extended objects, e.g. dislocations in

crystals, and fast particle tracks in matter, etc. The error in the calculation of properties, attributable to periodic boundary conditions, is on the order of  $1/N$ , where  $N$  is the number of particles in the model [13]. For this reason, the thermodynamic, structural, and diffusion properties of a liquid metal can be calculated using a model containing a few thousand particles in the basic cell.

Historically, pairwise potentials were the first to be used in simulating liquids. The most popular Lennard-Jones potential (or 6–12 *potential*) was successfully applied to simulate liquid argon. However, the utilization of this and other pair potentials for simulating metals is limited, even if they can generate models with a structure very similar to the real one. The structure of liquids is described by correlation functions of different orders, and diffraction studies make it possible to obtain pair correlation functions (PCFs) of a real metal. The theory of liquids predicts that there is always a pair interaction potential allowing the construction of a model of a liquid with a known (real) PCF [14, 15]. Algorithms for this purpose were developed in Refs [16–19]. In the reverse MC method, the agreement between model and real PCF is achieved by virtue of a series of minor atomic displacements in the static model; in this case, such displacements are chosen that decrease the difference between two PCFs. In the algorithms proposed by Schommers [16, 17] and Reatto et al. [18], the pairwise potential itself is varied according to definite rules. The resulting potential in the form of a table generates the prearranged PCF with a desired degree of accuracy.

The Schommers algorithm is as follows. Suppose a diffraction experiment yields a pair correlation function  $g_0(r)$  of a single-component liquid having real density  $n_0$ . It is necessary to calculate such pair potential  $\varphi(r)$  that would generate the preassigned PCF  $g_0(r)$  in simulation by the MD method. Let a certain bare potential generate a model with PCF  $\varphi_1(r)$  when a model of a liquid with density  $n_0$  is constructed by the MD method. As a rule,  $g_1(r) \neq g_0(r)$ . Therefore, correction  $\Delta\varphi(r)$  for the potential is needed to improve the agreement between model and diffraction PCF. It may be chosen in the form  $\Delta\varphi_1(r) = \alpha k_B T \ln [g_1(r)/g_0(r)]$ , where  $\alpha > 0$  is the damping factor found empirically,  $k_B$  is the Boltzmann constant, and  $T$  is the temperature of the liquid. Indeed, the correction will be positive over distance intervals where  $g_1(r) > g_0(r)$ , the potential has to increase and PCF decrease (the higher the potential, the smaller the probability of meeting a neighbor). Conversely, for  $g_1(r) < g_0(r)$ , the correction will be negative, the potential has to decrease, and PCF increase. Then, a new model of a liquid with the pair potential  $\varphi_2(r) = \varphi_1(r) + \Delta\varphi_1(r)$  should be constructed. It will give new PCF  $g_2(r)$  closer to  $g_0(r)$  than a correlation function  $g_1(r)$ . A new correction for the potential,  $\Delta\varphi_2(r) = \alpha k_B T \ln [g_2(r)/g_0(r)]$ , should be calculated, and so forth. Given reasonable model densities, this iteration procedure leads to the pairwise potential being sought. Iterations must continue till the PCF of the model is close enough to  $g_0(r)$ .

Usually, a few dozen such iterations are needed to have the standard deviation between a model PCF and a diffraction PCF below 0.01. These two PCFs are visually indistinguishable. There is no sense in striving to achieve a smaller deviation, because an error in the calculation of the diffraction PCF by the Fourier transform of the structure factor exceeds 0.01. The Schommers procedure does not yield a good result if the densities of the model and real liquids are

different. Moreover, this procedure is suitable only if the temperature is not too low for the models of liquids with real density, the structure of which (i.e. PCF) is determined solely by the  $\varphi(r)/k_B T$  ratio. At low temperatures, when the  $\varphi(r)/k_B T$  ratio becomes not too small at certain distances  $r$ , the system undergoes transition to the amorphous state, and the Schommers algorithm turns out to be inapplicable, because the structure no longer depends on  $\varphi(r)/k_B T$  as  $T \rightarrow 0$  and is determined by the force function  $\beta d\varphi(r)/dr$ , where  $\beta$  is any positive number [20]. The height of the first PCF peak near 3.5–4 forms the provisional boundary between the liquid and solid (amorphous) states. At higher PCF peaks (i.e., at a higher degree of structure ordering), the Schommers algorithm ceases to yield good results; moreover, difficulties emerge with the solution of equations of the statistical theory of liquids (Born–Green–Bogoliubov, Ornstein–Zernike, Percus–Yevick equations), sometimes resulting in nonphysical solutions. The authors of Refs [20–23] proposed algorithms for simulating the amorphous phase as  $T \rightarrow 0$  with a given PCF (‘delta-algorithm’ and ‘comparison of coordination numbers algorithm’). The results of recovery of force functions based on these algorithms are also inconsistent and depend on the choice of the bare potential.

Importantly, the Schommers algorithm is a versatile procedure, i.e., different bare potentials may give rise to different pair interaction potentials generating practically identical PCFs [20, 24]. For example, the PCF of a liquid does not change if the potential generating this correlation function is supplemented by a potential that generates a similar PCF of the amorphous phase at absolute zero.

The Schommers algorithm is both simple and reliable, because it guarantees obtaining the proper pair potential, given the density is specified correctly. The difference between algorithms [16, 17] and [18] is insignificant due to the aforementioned ambiguity of the solution to the problem of reconstructing a pairwise potential from the known PCF. Therefore, it makes no sense to argue which algorithm is better.

Pair interaction potentials can be derived based on pseudopotential calculations [25]. This approach was popular in the 1950s–1960s. An effective pair potential (‘pseudo-potential’) is defined by the formula [25]

$$\varphi(r) = \frac{V}{\pi^2 N} \int_0^\infty F(q) \frac{\sin qr}{qr} q^2 dq. \quad (1)$$

Here,  $N$  is the number of particles in volume  $V$ , and  $F(q)$  is the characteristic function dependent on the Fourier transform of the metal ion pseudopotential. Both first principle and model (parametrized) pseudopotentials are involved in concrete calculations.

Pairwise potentials were extensively used in studies of the static and dynamic properties of liquid metals in the framework of the theory of liquids [5, 13, 26–30]. It is possible to obtain good data on the static and dynamic structure and viscous and diffusion properties of a liquid in the context of pair interparticle interaction. These properties are sensitive to the short-range part of the potential.

The limited scope of this review makes impossible a detailed consideration of voluminous data on the computer simulation modeling of liquid metals in the framework of pairwise interaction. However, one thing is perfectly clear: a serious drawback of pair potentials is that the thermodynamic properties of model metals (pressure, energy) with a correct structure do not agree with experimental findings.

Hence, there is a necessity to step beyond the pair potential paradigm and design rational many-particle potentials.

At present, the embedded atom model (EAM) proposed to describe crystalline metals at temperatures near absolute zero is widely employed to numerically simulate metals [6, 31–37]. The EAM takes advantage of collective interactions. The metal potential energy is expressed in the form

$$U = \sum_i \Phi(\rho_i) + \sum_{i<j} \varphi(r_{ij}). \quad (2)$$

Here,  $\Phi(\rho_i)$  is the ‘embedding potential’ of the  $i$ th atom depending on ‘effective electron density’  $\rho$  in the region where the center of the atom is localized, and the second sum contains the usual pair potential  $\varphi(r)$ . Effective electron density created at the point where a given atom resides by the surrounding atoms is found from formula  $\rho_i = \sum_j \psi(r_{ij})$ , where  $\psi(r_{ij})$  is the contribution of a  $j$ th neighbor to electron density. It was supposed in earlier work using EAM potentials that the effective electron density is a real density and can be calculated, for instance, from the tables of electron wave functions of free atoms. However, later authors ceased to ascribe such a literal sense to  $\Phi(\rho)$  and  $\psi(r)$  functions and began to consider EAM potentials as a sensible mathematical construction. The form of potential (2) is convenient in that the contribution from the embedding potential to the interparticle forces, similar to the pairwise contribution, looks like the sum over atomic pairs and is easy to calculate.

As a result, three adjustable functions,  $\Phi(\rho)$ ,  $\varphi(r)$ , and  $\psi(r)$ , are tapped, which opens up wide opportunities for correlating calculated properties and experimental findings. The choice among these functions is ambivalent. Their transformations by formulas

$$\begin{aligned} \rho^*(r) &\rightarrow \alpha \rho(r), \quad \Phi(\rho) \rightarrow \Phi\left(\frac{\rho^*}{\alpha}\right) \\ \text{and/or } \Phi^*(\rho) &\rightarrow \Phi(\rho) + \beta \rho, \quad \varphi^*(r) \rightarrow \varphi(r) - 2\beta \rho(r) \end{aligned} \quad (3)$$

do not change the magnitude of forces acting on the particles. In the case of crystals, where the set of the nearest-neighbor interatomic distances in equilibrium is not too large, it is possible to accurately adjust density, energy, elastic constants, vacancy formation energy, surface properties, and so forth to the experimental data and arrive at the correct relative stability of various crystallographic modifications of a given metal. Computer simulation with the EAM potential makes it possible to use such software packages as large-scale atomic/molecular massively parallel simulator (LAMMPS) [38]. Modifications of the original EAM scheme were also proposed [36, 39–43], taking into account the directionality of chemical bonds and permitting widening the range of metals adequately described by the EAM scheme. A disadvantage of EAM potentials is the large number of their parameters (normally, up to twenty).

The EAM scheme allows generalization to the case of binary metallic systems. EAM potentials are deemed ‘transferable’: in other words, their application can be extended (following definite rules) to solutions or even compounds. What is only needed is to determine additional pairwise potentials for pairs of different atoms.

Thus far, it is unclear if EAM potentials are accurate enough to describe metallic behavior in wide temperature ranges. Table 1 lists properties of crystalline Al, Cu, and Fe calculated by the MD method on the assumption of real density, choosing EAM potentials in accordance with metal

**Table 1.** Properties of crystalline metals calculated using the EAM potential.\*

Metal	Structure**	$T$ , K	$d$ , g cm <sup>-3</sup>	$p$ , GPa (EAM)	$-U$ , kJ mol <sup>-1</sup>		
					EAM	Experiment	Potential
Al	fcc	0	2.719	0.00	-324.2	-324.2	[44]
Al	fcc	298	2.700	0.23	-316.8	-323.8	[44]
Al	fcc	873	2.585	-0.26	-300.8	-307.1	[44]
Al	liquid	943	2.370	0.32	-288.8	-286.4	[44]
Cu	fcc	0	8.990	0.00	-341.6	-341.6	[45]
Cu	fcc	298	8.920	1.66	-334.1	-331.2	[45]
Cu	fcc	1073	8.518	1.11	-313.7	-310.3	[45]
Cu	liquid	1423	7.969	1.57	-292.0	-286.6	[45]
Fe	bcc	0	7.968	0	-397.7	-416.4	[46]
Fe	bcc	300	7.874	-1.66	-389.6	-411.5	[46]
Fe	bcc	1820	7.299	-0.99	-344.7	-353.0	[46]
Fe	liquid	1820	7.013	-0.38	-330.4	-339.2	[46]

\*  $T$ —temperature,  $d$ —model density,  $p$ —pressure, and  $U$ —internal energy.

\*\* fcc—face-centered cubic, and bcc—body-centered cubic.

properties at  $T = 0$ . At temperatures close to the melting point  $T_m$ , the calculated pressure values are on the order of 0.1–1.0 GPa, even though the real pressure is practically zero on the atomic scale. Given that model and real energies coincide at  $T = 0$ , the latter must be lower than the former for  $T > 0$ , because real thermal capacity at low temperatures tends to vanish, while that of the model is close to  $3R$  (molar gas constant  $R = 8.314 \text{ J mol}^{-1} \text{ K}^{-1}$ ). However, some data from Table 1 are in conflict with this inference. The difference between model and real energies at usual temperatures may reach a few kJ mol<sup>-1</sup>.

Moreover, potentials intended to describe the crystalline phase do not always yield good results in numerical simulations of just liquid metals. In the case of the real density of a liquid metal at temperatures close to the melting point, model pressure may substantially differ from zero (a few GPa). Accordingly, the density of liquid at zero pressure may deviate from the real one by several percent, whereas the difference between the respective energies reaches a few kJ mol<sup>-1</sup>.

The choice of the shape of the EAM potential and its parameters is possible taking advantage of quantum-mechanical methods. These methods [realized, for instance, in Gaussian-9, Vienna *ab initio* simulation package (VASP), or Spanish initiative for electronic simulation with thousands of atoms (SIESTA)] make it possible to calculate forces acting on each particle in the model of a liquid or amorphous metal. Wave functions of collective electrons are described, for example, by a set of plane waves; thereafter, coefficients of expansion in these waves are calculated, and the total forces acting on each atom are found by using the Hellmann–Feynman theorem. Given that all interparticle distances in a model and the forces acting on each atom are known, functions entering the EAM potential expression can be selected (the *force matching method*). The PotFit package may serve as an example implementing such a possibility [47].

Attempts have been undertaken as well to select a potential fairly well describing both crystalline and liquid metals. In Refs [46, 48], parameters of the EAM potential for iron were selected based not only on crystalline properties but also on the PCF of liquid iron at temperatures close to the melting point; also, the Born–Green–Bogoliubov equation was applied. In the simulation of liquid iron ( $T = 1820 \text{ K}$ )

with the EAM potential from Ref. [46], the resulting PCF was close to the real one, but the energy remained different from the experimental values (see Table 1).

As a rule, the currently available EAM potentials do not usually allow simultaneously describing both the crystalline and liquid phases of a metal. Therefore, it is important to develop EAM potentials specially for the description of liquid metals (see Table 1).

EAM potentials in the form of expression (2) do not explicitly contain the angles between the chemical bonds and are suitable for systems in which the contribution from directed (valence) bonds is either absent or very small. Therefore, these potentials cannot be used to describe systems dominated by valence interactions. Modifications of the initial EAM scheme take account of the bond directivity [36, 39–43]. For such systems, many-particle potentials that explicitly include the valence angles have been applied, e.g., Stillinger's and Weber's [49] or Tersoff's [50] three-particle potentials for carbon, germanium, and silicon. The linear combination of the EAM potential (2) and three-particle potentials can be appropriate for simulating systems like Au–Si and Au–Ge [42], the parameters of such a hybrid potential being clarified by the *ab initio* method. In these systems, the contribution of the metallic bonding remains essential.

C, Si, As, and P systems with the predominance of valence bonding make a world of difference due to the absence of a contribution from the metallic bonding at usual densities. The interest in such liquids arises, inter alia, from the fact that they exhibit structural liquid-to-liquid transitions in which the structure itself changes abruptly over a rather narrow density range. Such structural transition in liquid phosphorus (associated with a concurrent density jump) was, for example, revealed by the X-ray scattering technique at a pressure of about 1 GPa and temperatures of 1323–1348 K [51]. *Ab initio* MD calculations showed that such a transition leads to polymerization of molecules with preserved covalent bonding [52]. Such a transformation can hardly be regarded as a first-order phase transition; for my part, I do not believe it, at least till someone demonstrates two layers of liquid phosphorus of different densities in equilibrium. EAM potentials are hardly applicable to the structural description of such systems.

## 2.2 Form of the potential in the embedded atom model and the choice of its parameters

The shape of EAM embedding potentials varies. For example, the authors of Ref. [53] chose potential functions for six metals (Cu, Ag, Au, Nb, Ta, V) in the simple form  $\varphi(r) = A_1(r_{c1} - r) \exp(-c_1 r)$ ,  $\psi(r) = A_2(r_{c2} - r) \exp(-c_2 r)$ ,  $\Phi(\rho) = D \rho \ln \rho$ , where  $A_{1(2)}$ ,  $r_{c1(2)}$ ,  $c_{1(2)}$ , and  $D$  are the parameters. Here, there are only 7 parameters that can be selected based on the known crystal properties at  $T = 0$ . These potentials fairly well describe the metal properties for  $T \sim 0$ ; however, some of them stop working as the temperature rises. For example, the bcc-lattice in a niobium model breaks down even at  $T = 500 \text{ K}$ , and that of vanadium at  $T = 800–1000 \text{ K}$ .

The presence of the embedding potential  $\Phi(\rho)$  in an EAM potential accounts for the additional contribution to the pair force between  $i$  and  $j$  atoms:

$$F_{ij}^{\text{EAM}} = - \left( \frac{\partial \Phi_i}{\partial \rho} \bigg|_{\rho_i} + \frac{\partial \Phi_j}{\partial \rho} \bigg|_{\rho_j} \right) \frac{\partial \psi}{\partial r} \bigg|_{r_{ij}}. \quad (4)$$

**Table 2.** Properties of liquid metals near  $T_m$  obtained by the MD method with the use of the EAM potential.\*

Metal	$T, K$	$d, g\ cm^{-3}$	$p, GPa$ (EAM)	$R_g$	$U, kJ\ mol^{-1}$				$K_T, GPa$		$D \times 10^5, cm^2\ s^{-1}$	
					EAM	$E_{eT}$	EAM + $E_{eT}$	Experiment	EAM	Experiment	EAM	Experiment
Li	463	0.5139	0.014	0.033	–145.87	0.048	–145.4	–145.6	9.90	9.55	9.82	7.34
Na	378	0.9239	–0.019	0.017	–96.03	0.030	–96.00	–96.00	5.20	5.18	4.53	4.32
K	343	0.8278	0.005	0.028	–79.00	0.024	–78.76	–79.09	2.66	2.74	4.92	4.02
Rb	313	1.4785	–0.0045	0.018	–72.47	0.008	–72.46	–72.35	2.05	2.07	3.23	3.91, 2.69
Cs	323	1.8237	0.007	0.031	–65.89	0.017	–65.87	–65.97	1.87	1.40	2.39	2.41
Cu	1423	7.978	0.000	0.022	–287.7	0.524	–287.2	–287.8	75 ± 6	69.0	3.58	4.70, 4.63
Ag	1273	9.261	0.054	0.027	–239.77	0.535	–239.2	–239.7	53.8	53.8	3.45	2.80
Zn	723	6.546	–0.008	0.029	–103.80	0.171	–103.6	–103.6	41.5	41.8	3.39	2.43
Hg	293	13.55	0.009	0.033	–55.28	~ 0	–55.28	–55.32	25.3	24.9	1.02	1.42–1.72
Al	943	2.37	0.321	0.067	–288.80	0.388	–288.8	–286.4	33.4	41.7	3.56	—
Ga	293	6.10	~ 0	0.018	–265.24	~ 0	–265.2	–265.2	48.3	48.1	1.23	1.56
Sn	523	6.93	–0.010	0.041	–288.55	0.131	–288.42	–288.56	36.6	36.6	2.09	2.40–2.60
Pb	613	10.67	–0.008	0.032	–175.41	0.222	–175.19	–175.45	29.5	29.6	2.15	1.14–2.36
Bi	573	10.04	0.002	0.018	–182.04	0.220	–181.82	–182.06	23.2	22.8	3.73	2.03

\*  $R_g$  — discrepancy between PCF of model and real metal,  $U$  (EAM) — model internal energy,  $E_{eT}$  — electron energy calculated by formula (11), and  $K_T$  — isothermal bulk compression modulus.

The derivative  $\partial\psi/\partial r$  is negative in the sense of the  $\psi(r)$  function, because the effective electron density created by an atom must decrease with distance. The derivative  $d\Phi/d\rho$  usually changes the minus sign to plus as  $\rho$  grows. Were the value of  $\rho$  identical in all atoms of a model, the additional pair force would have the form  $F_{ij}^{EAM} = -2(d\Phi/d\rho)(d\psi/dr)$ . If  $d\Phi/d\rho = 0$  for all the atoms at a certain  $\rho$  value, the effective force  $F_{ij}^{EAM}$  disappears, and the behavior of the system is determined by the pair force  $f_{ij} = -d\phi(r)/dr$  alone. Therefore, it is convenient to choose the embedding potential for a liquid in such a form at which the derivative  $d\Phi/d\rho$  disappears at temperatures close to  $T_m$ . The present author takes advantage of the following form for the embedding potential in his work:

$$\psi(r) = p_1 \exp(-p_2 r), \quad (5)$$

$$\Phi(\rho) = a_1 + c_1(\rho - \rho_0)^2 \quad \text{for } \rho_1 \leq \rho \leq \rho_8, \quad (6)$$

$$\Phi(\rho) = a_i + b_i(\rho - \rho_{i-1}) + c_i(\rho - \rho_{i-1})^2 \quad \text{for } \rho_i \leq \rho \leq \rho_{i+1}, \quad i = 2, 3, 4, 5, \quad (7)$$

$$\Phi(\rho) = [a_6 + b_6(\rho - \rho_5) + c_6(\rho - \rho_5)^2] \left[ \frac{2\rho}{\rho_5} - \left( \frac{\rho}{\rho_5} \right)^2 \right] \quad \text{for } \rho \leq \rho_5, \quad (8)$$

$$\Phi(\rho) = a_9 + b_9(\rho - \rho_8) + c_9(\rho - \rho_8)^m \quad \text{for } \rho_8 \leq \rho \leq \rho_9, \quad (9)$$

$$\Phi(\rho) = a_{10} + b_{10}(\rho - \rho_9) + c_{10}(\rho - \rho_9)^n \quad \text{for } \rho > \rho_9, \quad (10)$$

with  $\rho_0 = 1$ ; at  $\rho = \rho_i$ , functions  $\Phi(\rho)$  and  $d\Phi/d\rho$  are continuous. The values of  $\rho_i$  increase in the order  $\rho_5 < \rho_4 < \rho_3 < \rho_2 < \rho_1 < \rho_0 < \rho_8 < \rho_9$ . If for all atoms  $\rho = \rho_0$ , then  $d\Phi/d\rho = 0$ , and the structure depends only on the pair contribution to the potential. This contribution can be calculated, say, with the help of the Schommers algorithm. The number of  $\rho$ -axis divisions at the intercept  $0 < \rho < \rho_0$  can be either greater or smaller than five. As a result, the embedding potential is determined by parameters  $p_1, p_2, a_1, c_1 - c_{10}, \rho_1 - \rho_9, m, n$ , which, in principle, allow adjusting such properties of liquids as density, potential energy (atomization energy), and bulk compression modulus to experimental

values. Parameters  $a_2 - a_{10}$  and  $b_2 - b_{10}$  are deduced from the continuity conditions for  $\Phi(\rho)$  and  $d\Phi/d\rho$ . Expressions (6)–(8) are used to simulate states with normal or reduced density, and expressions (9), (10) to simulate states with enhanced density, e.g., under shock compression.

An advantage of choosing the embedding potential in the form (5)–(10) consists in the fact that the energy of the models is possible to change by simple variation of parameter  $a_1$ , and the bulk compression modulus by varying parameter  $c_2$ . The remaining parameters are selected from the temperature dependence of liquid metal density or (at high pressures) taking into account the form of the shock Hugoniot. In the end, it is possible to attain the accurate description of the properties of a liquid metal at temperatures close to the melting point  $T_m$  (Table 2).

The key issue as regards EAM potentials is their applicability at elevated temperatures, including high enough ones (e.g., under conditions of shock compression). In shock experiments with metals, a shock wave passes through a specimen several millimeters in width with a speed of a few kilometers per second. Transit time equals  $\sim 10^{-6}$  s, i.e., long enough to consider states behind the wave front to be practically equilibrated and resort to ordinary thermodynamics when describing them. The potentials themselves do not contain temperature explicitly; therefore, their adequacy is a matter of their proper shapes. However, this question thus far remains open. Most researchers simulating the crystalline phases show little concern about temperature effects; this accounts for the fact that most data on the influence of temperature on the properties of matter come from liquid metal studies.

In this context, alkali metals well known as heat carriers appear to be most suited. These metals reside in the liquid state between 1500 and 2000 K. When the parameters of an EAM potential are deduced from the known temperature dependence of metal density along the crystal–liquid equilibrium line, the model energy is systematically underestimated at temperatures above 1000 K in comparison with the true energy of the given metal [54–56], and the heat capacity of the model proves to be lower than the real heat capacity of the metal. This can be explained (at least partly) by the contribution from electron thermal capacity.

When taking account of the heat energy of collective electrons, one should bear in mind that it enters the total energy of a metal but has no effect on particle–particle interaction and takes no part in the EAM scheme, being a kinetic contribution similar to the energy of atomic thermal motion. For the purpose of MD simulation, this energy should be subtracted from the total energy of the metal [54–56].

Thermal electron energy can be calculated using two equations of statistical mechanics governing the number of collective electrons  $N_{\text{el}}$  and their energy  $E_{\text{el}}$ :

$$\begin{aligned} N_{\text{el}} &= C \int_0^\infty \frac{\varepsilon^{1/2} d\varepsilon}{1 + \exp[(\varepsilon - \mu)/k_B T]}, \\ E_{\text{el}} &= C \int_0^\infty \frac{\varepsilon^{3/2} d\varepsilon}{1 + \exp[(\varepsilon - \mu)/k_B T]}. \end{aligned} \quad (11)$$

Here,  $\mu$  is the electron chemical potential. In the free-electron model, coefficient  $C = 4\pi(2m)^{3/2}V/h^3$ , where  $m$  is the electron mass,  $V$  is the metal volume, and  $h$  is the Planck constant. Equations (11) are usually well satisfied for simple liquid metals with the isotropic structure. By specifying  $N_{\text{el}}$ ,  $V$ , and  $T$  in the first equation, one can find  $\mu$ , and, then,  $E_{\text{el}}$  is found from the second equation.

Analysis of the results on shock compression are usually performed by a method in which the heat capacity of matter is assumed to equal  $3R$ , and the Grüneisen coefficient  $\gamma = (V/C_V)(\partial p/\partial T)_V$  ( $C_V$  is the heat capacity,  $p$  is the pressure) is considered to depend only on the volume [57]. Electron contributions to energy and pressure are disregarded in such analysis. In what follows, this calculation method will be referred to as ‘standard’. In the case of shock compression, the electron energy should be counted off from the initial compression temperature (usually  $\approx 300$  K). For this reason, a change in the electron thermal energy should be defined as  $E_{eT}(T) = E_{\text{el}}(T) - E_{\text{el}}(300 \text{ K})$ . Subtraction of electron thermal energy from the metal potential energy leads as a rule to a marked decrease in the estimated temperature on the shock Hugoniot. On the same grounds, when subtracting electron thermal energy (contributing to the kinetic energy) from the total metal energy, one should separately identify the electron gas thermal contribution (which must not be involved in the EAM scheme either) to pressure  $p_{\text{el}}$ . The value of  $p_{\text{el}}$  can be calculated from the formula [58]

$$p_{\text{el}} V = \frac{2}{3} E_{\text{el}}. \quad (12)$$

A change in electron thermal pressure, similar to that in electron energy, can be described as  $p_{eT}(T) = p_{\text{el}}(T) - p_{\text{el}}(300 \text{ K})$ . Such a contribution can be rather large. By way of example, for lithium in the case of normal volume, one has  $p_{\text{el}} = 13.97 \text{ GPa}$  and  $17.72 \text{ GPa}$  at  $300 \text{ K}$  and  $15,000 \text{ K}$ , respectively; hence,  $p_{eT}(15,000 \text{ K}) = 3.75 \text{ GPa}$ .

Parameters  $\rho_8, \rho_9, c_9, c_{10}, m, n$  in formulas (9) and (10) are chosen so as to satisfy two conditions: (1) the similarity of calculated pressure to that found on the shock adiabat, and (2) a high enough accuracy of the following relationship for a shock wave [59]:

$$U_2 - U_1 = \frac{1}{2} (p_1 + p_2)(V_1 - V_2), \quad (13)$$

where  $V_i, p_i$ , and  $U_i$  denote the volume in moles, pressure, and total energy of matter, respectively, ahead of the shock wave front ( $i = 1$ ) and behind it ( $i = 2$ ). In this method, tempera-

ture is a determinable quantity [60]. Formula (13) is utilized to choose parameters for the embedding potential, taking into consideration that  $p_1 \approx 0$ .

The possibility of improving the description of metals in terms of EAM potential at high temperatures has so far been checked out only for metals in group I of the Periodic Table. For them, this method yields good results described in Section 3 below, together with the discussion of data on concrete metals.

The author of this review made calculations largely in the  $NVT$ -ensemble, based on the models containing a few thousand particles in the basic cube. Most attention was given to a sufficiently accurate determination of the thermodynamic properties of liquid metals under various conditions. The Verlet integration algorithm was applied without any modifications for the realization of isothermal or isobaric conditions. Isothermicity was ensured by minimal corrections of the particles’ coordinates at each 10th or 20th preceding time step rather than in a continuous manner. Temperature fluctuations in such an MD-run were usually on the order of  $0.1$ – $1.0 \text{ K}$ . For example, temperature fluctuations in an  $NVT$ -run at  $T = 773 \text{ K}$  for mercury were  $\pm 0.32 \text{ K}$ , versus  $\pm 8.4 \text{ K}$  in an  $NVE$ -run. Simulation under constant pressure ( $NpT$ ) was ensured by very small periodic corrections of the edge length of the basic cube (at each 10th step); it was usually performed only in calculations of melting temperature. In the case of aluminum, for instance, the edge length of the basic cube at  $T = 943 \text{ K}$  and near-zero pressure varied in an MD-run within  $33.920 \pm 0.024 \text{ \AA}$ , while the pressure fluctuated within  $\pm 0.052 \text{ GPa}$ .

### 2.3 First principle calculations (*ab initio* method)

The *ab initio* method makes use of the possibility of calculating quantum-mechanical forces acting on each atom of a model (Hellmann–Feynman theorem) and includes them in the MD scheme. This idea was first realized by Car and Parrinello [9] as the Car–Parrinello molecular dynamics (CPMD) method. The first principle method does not require specification of the interparticle interaction potential, but the count rate is very low and high-performance computers are needed to employ it. Accordingly, the models are small in size, usually a few dozen atoms (or slightly more than 100 at the most) in the basic cell. The theory behind the method is described in several review articles, e.g. Refs [6, 61, 62]. Both commercial (VASP [63]) and free (SIESTA) software packages designed specially for use in the *ab initio* method are available. An advantage of this method is the possibility of calculating electron wave functions and the electron spectrum. However, the small size of the models compromises the accuracy of the determination of thermodynamic and structural properties. For example, PCFs can at best be calculated up to the second peak. However, the accuracy of the *ab initio* method awaits systematic evaluation.

A variant of this method is the so-called Born–Oppenheimer molecular dynamics (BOMD) based on the Born–Oppenheimer approximation. It is assumed in this approach that electron wave functions become instantaneously adjusted to the field created by slowly moving nuclei (ions). Also, the BOMD method permits calculating the particles’ trajectories without specification of interparticle interaction potentials (‘nonempirical molecular dynamics’). The method was realized, for instance, in the Gaussian package and was applied to calculate lattice dynamics and sodium melting process [64–66].

### 3. Simulation of group I metals of the Periodic Table

#### 3.1 Alkali metals

In the first decades of alkali metal simulation research, pair interaction potentials were used (see reviews [5, 20]). They were succeeded by studies with EAM potentials and the search for its best shape for lithium [55, 56, 60, 67, 68], sodium [55, 56, 60, 69], potassium [54–56, 60, 70], rubidium [55, 56, 60, 71–73], and cesium [55, 56, 60, 74–78]. The author of the present review calculated the pair-potential contribution to the EAM potential with the use of the Schommers algorithm [16, 17] in the form of a table and thereafter analytically approximated the resultant table of numerical data. In the end, the EAM potential was accepted in the form (5)–(10) with a different number of the  $\rho$ -axis divisions for  $\rho < \rho_0$  in various cases. Expressions (5)–(8) hold true at normal and low densities, while (9) and (10) at enhanced density. The energy of a metal is determined with respect to that of resting gas atoms and calculated from the data on atomization energy and other thermodynamic properties. Knowledge of the energy allows parameter  $a_1$  to be found. Parameter  $c_1$  is defined so as to have the bulk compression modulus of liquid close to the actual one at temperatures near the melting point. Parameters entering formulas (5)–(8) are determined from the temperature dependence of the density, taking into account the continuity of the embedding potential at  $\rho_i$  points of the  $\rho$ -axis division. Parameters in formulas (9) and (10) are determined using results of shock compression.

**3.1.1 Lithium.** The authors of Ref. [79] reported on two methods: (1) the pseudopotential technique, and (2) the pseudoatom model, in calculating two effective pair interaction potentials for lithium atoms, which proved essentially different but generated identical PCFs in MD simulations. However, both the pressure and energy of the models deviated substantially from the respective actual values. For example, calculations in case (1) at 470 K and density 0.0445 atoms per  $\text{\AA}^3$  yielded a pressure of 0.41 GPa and lithium energy of  $-19.00 \text{ kJ mol}^{-1}$  at a real energy of  $-145.6 \text{ kJ mol}^{-1}$ . Despite these discrepancies, the calculated self-diffusion coefficients and viscosity were in excellent

agreement with experimental data. Fairly good agreement with experiment was also obtained for dynamic functions of the melt, such as the autocorrelation velocity function and structure factor. This means that structural concordance for liquid is quite sufficient for calculating dynamic characteristics but insufficient to consider a model to be adequate thermodynamically.

The EAM potential for liquid lithium was computed in works [55, 56, 60, 80]. The initial models in Refs [55, 56, 60] had a bcc-structure and contained 2000 particles each in the basic cube with periodic boundary conditions. The Verlet algorithm with a time step of  $(0.010-0.001)t_0$  was applied, where the internal time unit  $t_0 = 2.682 \times 10^{-14} \text{ s}$ . Most models were constructed in the  $NVT$ -ensemble. Their density was set in accordance with experimental data [81]. The pairwise contribution to the potential was given by the Schommers algorithm and had the form

$$\begin{aligned} \varphi(r) [\text{eV}] = & -0.161539351212 \times 10^1 \\ & + \frac{0.329193195820 \times 10^2}{r} - \frac{0.245830404172 \times 10^3}{r^2} \\ & + \frac{0.840217873656 \times 10^3}{r^3} - \frac{0.136938125679 \times 10^4}{r^4} \\ & + \frac{0.905623694715 \times 10^3}{r^5}, \quad 2.45 < r < 7.50 \text{ \AA}, \\ \varphi(r) [\text{eV}] = & 0.252868 + 0.15252(2.45 - r) \\ & + 0.38 \{ \exp [1.96(2.45 - r)] - 1 \}, \quad r \leq 2.45 \text{ \AA}. \end{aligned} \quad (14)$$

At  $r = 2.45 \text{ \AA}$ , potential (14) and its derivative are continuous (see Fig. 1).

Parameters of embedding potential  $\Phi(\rho)$  (5)–(8) responsible for the state of lithium at low pressures (the last multiplier in square brackets in formula (8) is omitted!) were found from the temperature dependence of liquid lithium density:  $p_1 = 3.0511$ ,  $p_2 = 1.2200 \text{ \AA}^{-1}$ ,  $\rho_0 = 1$ ,  $\rho_1 = 0.900$ ,  $\rho_2 = 0.840$ ,  $\rho_3 = 0.700$ ,  $\rho_4 = 0.550$ ,  $\rho_5 = 0.350$ ,  $a_1 = -0.8948$ ,  $c_1 = 0.0326$ ,  $c_2 = 1.700$ ,  $c_3 = -1.020$ ,  $c_4 = 1.750$ ,  $c_5 = -1.000$ ,  $c_6 = 11.0$ . The remaining parameters were determined from the continuity conditions for  $\Phi(\rho)$  and  $d\Phi/d\rho$  at points  $\rho = \rho_i$ , viz.  $a_2 = -0.894474$ ,  $b_2 = -0.006520$ ,  $a_3 = -0.887963$ ,  $b_3 = -0.210520$ ,  $a_4 = -0.878482$ ,  $b_4 = 0.075080$ ,  $a_5 = -0.850369$ ,  $b_5 = -0.449920$ ,  $a_6 = -0.800385$ ,  $b_6 = -0.049920$ . Parameters  $p_1$  and  $\rho_0, \rho_1, \dots$  are dimensionless, while all the parameters  $a, b$ , and  $c$  have a dimension expressed in eV.

Parameters  $\rho_8, \rho_9, c_9, c_{10}, m$ , and  $n$  responsible for strongly compressed states were determined in Refs [56, 60] taking into consideration the data on static [82] and shock [83–87] compression. The latter data set (shock Hugoniot), shown in Fig. 2, exhibits spreading. These data were approximated in Ref. [60] by the expression

$$\begin{aligned} p [\text{GPa}] = & -8.633981 \times 10^2 Z^3 + 1.962050 \times 10^3 Z^2 \\ & - 1.516047 \times 10^3 Z + 4.028962 \times 10^2. \end{aligned} \quad (15)$$

Here,  $Z = V/V_0$  (the normal lithium volume  $V_0 = 12.998 \text{ cm}^3 \text{ mol}^{-1}$ ). The adequacy criteria for the choice of potential parameters were the two aforementioned conditions: (1) nearness of calculated model pressure to that on the shock Hugoniot, and (2) satisfiability of the following relation for the shock wave:  $U_2 - U_1 = (1/2)(p_1 + p_2)(V_1 - V_2)$ . Parameters of the embedding

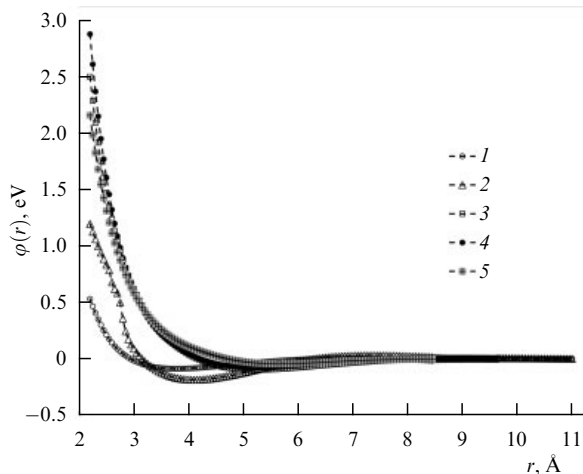


**Figure 1.** Calculated pair contributions to EAM potentials of alkali metals: 1—Li, 2—Na, 3—K, 4—Rb, and 5—Cs.

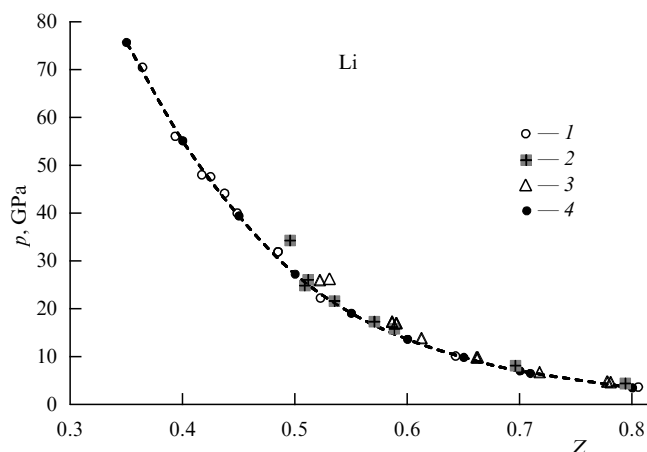


**Figure 2.** Lithium shock Hugoniot: 1—data from Ref. [84], 2—data from Ref. [85], 3—data from Ref. [86], and 4—molecular-dynamic data:  $p_{\text{calc}} = p_M + p_{eT}$ .

potential responsible for compressed states were selected as follows. First, having chosen a definite state on the shock Hugoniot, a model was constructed with a desired degree of compression, along with pressure and energy known from experiment. The calculated metal energy  $E_M$  minus the change in the electron thermal energy was found from the formula

$$E_M = U_0 + U_2 - U_1 - E_{eT}. \quad (16)$$

Here,  $U_0 = -156.8 \text{ kJ mol}^{-1}$  is the bcc-lithium energy at  $T = 300 \text{ K}$  [55, 56] with respect to the energy of resting particles spaced infinitely far apart. The values of  $\Delta U = U_2 - U_1$  were calculated by formula (13), and the electron thermal energy and pressure were calculated by

formulas (11), (12). The actual energy  $E_{MD}$  of the MD model was made equal to  $E_M$  by varying the model temperature. Thereafter, the resulting model pressure was compared with the pressure along the shock Hugoniot, from which changes in electron thermal pressure  $p_{eT}(T)$  were subtracted. Every time the model pressure proved to be other than the experimental one, parameters of the embedding potential responsible for compressed states were varied and the model temperature, thermal energy, and thermal pressure of electrons were recounted.

As a result, the following values of coefficients entering into embedding potential were obtained:  $\rho_8 = 1.10$ ,  $\rho_9 = 3.305$ ,  $c_9 = -0.036 \text{ eV}$ ,  $c_{10} = -0.0745 \text{ eV}$ ,  $m = 1.50$ ,  $n = 2.00$ . The remaining parameters were found from the continuity conditions at the points  $\rho = \rho_i$ , namely  $a_9 = -0.894474 \text{ eV}$ ,  $b_9 = 0.006520 \text{ eV}$ ,  $a_{10} = -0.997971 \text{ eV}$ ,  $b_{10} = -0.073666 \text{ eV}$ . The embedding potential for lithium is represented in Fig. 3.

The properties of the lithium models thus constructed are listed in Tables 3, 4. The proposed EAM potential is not quite suitable for bcc-lithium, since pressure is manifestly nonzero at 298 K and normal density (see the first row in Table 3). The model density of the bcc-lithium is increased by 3.1% at zero pressure. In the case of liquid lithium (states 2–9), model pressure is almost zero. Table 3 also contains root-mean-square deviations  $R_g$  (discrepances) between model and diffraction PCFs [89–91]. They are rather small because two PCFs are visually indistinguishable for  $R_g = 0.01$ –0.03. However, good agreement between the model and experimental energies remains only at temperatures below  $\sim 1000 \text{ K}$ . As temperature increases further, the model energy enhances more slowly than the actual one. According to Ref. [92], this difference is mostly due to the contribution from electron thermal capacity.

An additional possibility of investigating the model structure is provided by calculation of the structure factor

**Table 3.** Properties of liquid lithium and sodium\* obtained by the MD method with EAM potential (5)–(8).

No.	$T, \text{ K}$	$d, \text{ g cm}^{-3}$	$p_{\text{EAM}}, \text{ GPa}$	$\langle \rho \rangle$	$R_g$	$U, \text{ kJ mol}^{-1}$				
						$U_{\text{EAM}}$	$E_{\text{el}}$	$E_{eT}$	$U_{\text{EAM}} + E_{eT}$	Experiment [81]
1	2	3	4	5	6	7	8	9	10	11
Lithium										
1**	298	0.5350	−0.5071	$1.038 \pm 0.044$	—	−154.73	0.113	0	−154.73	−156.8
2	463	0.5139	0.014	$1.000 \pm 0.063$	0.033	−145.87	0.175	0.048	−145.82	−145.6
3	523	0.5090	0.050	$0.991 \pm 0.069$	0.033	−144.14	0.223	0.072	−144.07	−143.8
4	868	0.4777	0.001	$0.922 \pm 0.081$	0.022	−134.63	0.614	0.268	−134.36	−133.7
5	1000	0.4639	−0.019	$0.894 \pm 0.095$	—	−130.99	0.815	0.375	−130.62	−129.9
7	2000	0.3679	−0.012	$0.693 \pm 0.130$	—	−104.64	3.26	1.88	−102.76	−100.4
9	3000	0.2698	0.025	$0.519 \pm 0.169$	—	−75.70	7.34	5.223	−70.48	−65.6
Sodium										
1**	298	0.9664	−0.107	$1.052 \pm 0.055$	—	−100.51	0.06	0	−100.51	−101.30
3	378	0.9239	−0.019	$1.000 \pm 0.073$	0.017	−96.03	0.10	0.030	−96.00	−96.00
4	473	0.9041	−0.003	$0.977 \pm 0.084$	0.028	−93.34	0.15	0.079	−93.26	−93.03
5	573	0.8807	−0.008	$0.946 \pm 0.090$	0.037	−90.58	0.23	0.198	−90.38	−89.00
6	723	0.8439	−0.004	$0.900 \pm 0.106$	0.062	−86.56	0.36	0.266	−86.29	−85.53
9	1500	0.6561	−0.014	$0.699 \pm 0.135$	—	−65.48	1.55	1.564	−63.92	−62.56
10	2000	0.5097	0.014	$0.604 \pm 0.172$	—	−49.98	2.76	3.327	−46.65	−44.83
11	2300	0.3793	0.020	$0.535 \pm 0.179$	—	−40.14	3.65	5.324	−34.82	−31.73

\*  $\langle \rho \rangle$  — mean effective electron density,  $E_{\text{el}} = \gamma_0 T^2/2$  — electron energy, and  $E_{eT}$  — electron energy calculated by formula (11).

\*\* Crystalline state.

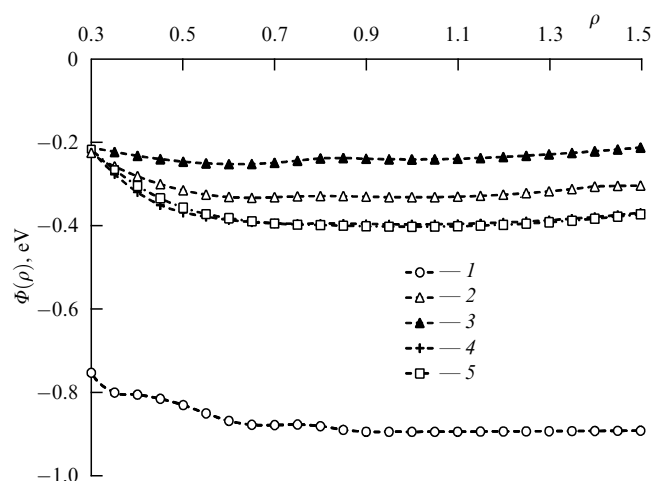


**Table 4.** Properties of lithium and sodium models at shock compression parameters ( $Z$  — degree of compression) [60].

$Z$	$P$ , GPa	$U_2 - U_1$ , kJ mol <sup>-1</sup> , from (13)	$T$ , K (model)	$T$ , K [88]	$\mu$ , eV	$E_{eT}$ , kJ mol <sup>-1</sup> , from (11)	$p_{eT}$ , GPa	$E_M$ , kJ mol <sup>-1</sup> , from (16)	$E_{MD}$ , kJ mol <sup>-1</sup>	$p_M$ , GPa, model	$p_M + p_{eT}$ , GPa
1	2	3	4	5	6	7	8	9	10	11	12
Lithium											
1.00*	0	0	300	300	4.704	0.000	0	-156.80	-156.94	~ 0	~ 0
0.80*	3.71	4.823	300	424	5.458	0.000	0	-151.98	-151.13	3.41	3.41
0.70*	6.92	13.496	370	623	5.966	0.013	0	-143.32	-143.88	6.94	6.94
0.60	13.1	34.086	550	1170	6.612	0.057	0.01	-122.77	-123.49	13.55	13.56
0.50	27.5	89.232	1800	—	7.464	0.745	0.08	-68.31	-68.06	27.15	27.23
0.40	55.1	215.04	5490	—	8.643	6.103	0.78	52.14	53.18	54.08	54.86
0.30	101.4	461.1	13,880	—	10.382	31.74	5.42	272.55	272.44	96.65	102.07
Sodium											
1.00*	0	0	298	300	3.147	0.000	0	-101.35	-100.56	-0.094	0
0.75*	2.57	7.64	300	531	3.812	0.000	0	-93.70	-93.67	3.47	3.47
0.70*	5.03	17.92	580	682	3.992	0.090	0.01	-83.53	-83.81	4.90	4.91
0.60*	9.57	45.47	1180	1392	4.422	0.557	0.03	-56.39	-56.87	9.52	9.55
0.50	22.3	132.5	2640	3768	4.996	2.430	0.13	28.72	28.26	23.71	23.84
0.45	38.4	250.9	6400	6670**	5.312	13.250	0.82	136.3	137.05	37.82	38.64
0.40	66.4	472.75	14,250	—	5.565	56.815	3.99	314.58	315.13	62.28	66.27

\* Crystalline state.

\*\* Extrapolated value.

**Figure 3.** Calculated embedding potentials of alkali metals: 1 — Li, 2 — Na, 3 — K, 4 — Rb, and 5 — Cs.

$S(\mathbf{K})$  of the entire model for a set of scattering vectors  $\mathbf{K}$ . The value of  $S(\mathbf{K})$  may be calculated by the formula

$$S(\mathbf{K}) = \frac{1}{N} \left| \sum_j \exp(i\mathbf{K}\mathbf{R}_j) \right|^2.$$

Here,  $\mathbf{R}_j$  is the radius vector of the  $j$ th particle, with the sum taken over all particles of the model. In an ideal crystal, the structure factor  $S(\mathbf{K})$  equals the number of particles in the crystal for reciprocal lattice site vectors and is zero for other vectors  $\mathbf{K}$ . Because simulation implies the use of periodic boundary conditions,  $\mathbf{K}$ -vector components must be equal to  $(2\pi/l)m$ , where  $l$  is the edge length of the basic cube, and  $m$  is any integer or nil. Scanning reciprocal lattice space requires sorting out hundreds of thousands of combinations of  $\mathbf{K}$ -vector projections with a small enough step size.

Table 3 collates electron thermal energies calculated in two variants: at the constant coefficient  $\gamma_0$  of bcc-lithium low-temperature electron thermal capacity, when  $E_{el} = \gamma_0 T^2/2$  ( $\gamma_0 = 1.63$  mJ mol<sup>-1</sup> K<sup>-2</sup> [93, 94]) (column 8), and with regard to formulas (11) ( $E_{eT}$ , column 9). The difference between  $E_{el}$  and  $E_{eT}$  is rather significant. Column 10 contains sums  $U_{EAM} + E_{eT}$  for lithium models ( $U_{EAM}$  is the model energy with respect to the energy of an ideal lithium gas at rest). Column 11 presents actual values of lithium energy with the same point of reference. Taking account of the electron thermal energy substantially improves the agreement between simulated and actual lithium energies; nonetheless, the discrepancy between theory and experiment still persists for  $T > 1000$  K.

The authors of Ref. [95] tapped the EAM potential from work [86] to simulate a two-phase liquid–vapor system. Each lithium model contained 16,000 atoms in the basic cell for  $T = 2000$ –5100 K. The liquid phase formed a plane layer, while the gaseous phase showed some evidence of atomic clusterization. No signs of stratification were observed in the transition layer. The temperature dependence of phase density was employed to estimate the critical temperature (5649 K), density (0.1553 g cm<sup>-3</sup>), and pressure (1686 bar) of lithium. The estimated viscosity of lithium was almost 20% lower than the actual value, and the self-diffusion coefficient was proportionally higher.

Table 4 demonstrates the results of MD calculations for lithium under shock conditions. The electron contributions to the energy and pressure were calculated by formulas (11) and (12). The models were found to reside in the liquid state when the compression was  $Z < 0.7$ , as appears from calculations of the structure factor. A comparison of the entries in columns 2 and 12 or 9 and 10 demonstrates excellent agreement between energies and pressures in the model predictions and shock compression experiments (see Fig. 2). The standard deviation for pressure and energy was only 0.43 GPa and 0.57 kJ mol<sup>-1</sup>, respectively. Thus, the

above EAM potential is quite acceptable for describing strongly compressed lithium states.

The electron contribution to the energy increases with a rise in temperature, and the electron thermal energy ( $31.74 \text{ kJ mol}^{-1}$ ) at  $Z = 0.30$  is  $\approx 10\%$  of the total lithium energy ( $31.74 + 272.44 = 304.18 \text{ kJ mol}^{-1}$ ).

MD calculations of the liquid metal properties at high pressures may be instrumental for the elucidation of the cause behind the maxima on the crystal–liquid equilibrium lines in the phase diagrams of all alkali metals. The lithium phase diagram displays a high maximum on the bcc-structure–liquid equilibrium line at a pressure of  $\approx 8 \text{ GPa}$  and temperature of  $530 \text{ K}$  [96]. A further increase in pressure causes the equilibrium line to rapidly drop to  $T \approx 200 \text{ K}$  at  $\approx 42 \text{ GPa}$ . The presence of the maximum indicates that the liquid density within the pressure interval to the right of the maximum is higher than that of the equilibrium solid phase (an anomaly like those of water, bismuth, antimony, etc.). There are reports on the theoretical evaluation of lithium phase diagrams. In Ref. [97], the lithium melting temperature was determined by preliminary calculation of the vibrational spectrum based on the linear response method of the density functional theory, which was followed by the application of Lindemann's melting criterion, according to which melting occurs only after the average atomic vibrational displacement makes up a certain fraction (usually  $0.10$ – $0.15$ ) of the interatomic distance. This calculation revealed a maximum on the solid (bcc and fcc)–liquid lithium equilibrium line, in agreement with experiment.

The MD method also allows the calculation of model melting temperatures  $T_m$  and the construction of a melting line. The following methods for calculating  $T_m$  appear to be best substantiated from the thermodynamic standpoint: (1) from the temperature at the intersection point of temperature dependence plots for crystal and liquid Gibbs energies, and (2) from the temperature at which the crystal–liquid interface velocity vanishes in a two-phase MD-model with the plane interphase boundary. It is believed that the difference between model and real  $T_m$  on the order of a few dozen kelvins is quite acceptable and testifies to the sufficiently high quality of the potential involved. However, these are rather laborious methods.

The melting temperature of a lithium model with the EAM potential was determined in Ref. [68] by the 'heat-up method' [98] based on the fact that MD models of a crystalline metal having defects melt at slight (within  $5$ – $10 \text{ K}$ ) overheating. A solid phase model with defects can be constructed either by removing one or a few atoms from a regular crystal model (i.e., creating vacancies) or by cooling and crystallization of a liquid-phase model. The melting temperature of lithium models was determined by staged heating and prolonged isothermal holding at each temperature. Melting occurrence was established from a sharp decrease in the maximum value of the structure factor. The melting temperature of a model under normal pressure was  $428 \pm 2 \text{ K}$ , or somewhat lower than that of actual lithium ( $453.69 \text{ K}$ ). Melting under a pressure of  $10 \text{ GPa}$  occurred at  $T_m = 688 \text{ K}$ . The melting temperature in experiments under such pressure [96, 99] was around  $530 \text{ K}$ , i.e., much lower than the model temperature.

The discrepancy between theory and experiment was attributed to the fact that the EAM potential is not quite suitable for crystalline lithium. The pressure in a bcc-lithium model with the potential (5)–(10) and actual density

**Table 5.** Density and CN of liquid lithium models at  $550 \text{ K}$ .

$p$ , GPa	0	10	20	30	40	50
Density, $\text{g cm}^{-3}$	0.508	0.829	1.003	1.148	1.277	1.461
CN	13.5	13.9	13.8	13.8	13.6	13.6

$0.535 \text{ g cm}^{-3}$  equaled  $-0.507 \text{ GPa}$  (see Table 3), and that in an fcc-lithium model was  $-0.270 \text{ GPa}$ . Under these conditions, the actual lithium pressure at  $300 \text{ K}$  and a density of  $0.535 \text{ g cm}^{-3}$  was close to zero. An interesting behavior is exhibited by fcc-lithium models within the pressure range in which the fcc-lattice remains stable. When fcc-lithium models with the EAM potential are heated from  $100$  to  $700 \text{ K}$ , the volume on the  $p = 25 \text{ GPa}$  isobar where the fcc-phase is stable [96] first *decreases* from  $6.522 \text{ cm}^3 \text{ mol}^{-1}$  (at  $T = 100 \text{ K}$ ) to  $6.447 \text{ cm}^3 \text{ mol}^{-1}$  (at  $T = 400 \text{ K}$ ) (i.e.  $(\partial V/\partial T)_p < 0$ , thus exhibiting water type anomaly) and begins to increase only during subsequent heating (to  $6.471 \text{ cm}^3 \text{ mol}^{-1}$  at  $T = 700 \text{ K}$ ). A similar case for solid Na is considered below in Section 3.1.2. As concerns liquid lithium, no structural anomalies were observed in its models built with the EAM potential. For example, the behavior of density and coordination number (CN) in a series of liquid lithium models at  $550 \text{ K}$  and  $0$ – $50 \text{ GPa}$  is illustrated in Table 5.

The model density of liquid lithium under isobaric heating ( $p = 25.0 \text{ GPa}$ ) monotonically decreases from  $1.074 \text{ cm}^3 \text{ mol}^{-1}$  at  $T = 700 \text{ K}$  to  $1.057 \text{ cm}^3 \text{ mol}^{-1}$  at  $T = 1200 \text{ K}$ . This means that liquid lithium does not undergo structural transformations as its density increases from  $0.535$  to  $1.46 \text{ g cm}^{-3}$ . At the same time, the density of fcc-lithium models at  $T = 550 \text{ K}$  and  $p = 20 \text{ GPa}$  amounts to  $1.008 \text{ g cm}^{-3}$ , i.e., only  $0.5\%$  higher than that of liquid models under the same conditions; in other words, melting elicits only a slight enlargement of the volume.

Liquid lithium models with 64 atoms in the basic cube were constructed by the *ab initio* method [100]. Publications on the simulation of liquids by this method do not usually contain information about energy, being focused on electronic properties, structural characteristics (PCF), and the self-diffusion coefficient (viscosity). A self-diffusion coefficient of  $7 \times 10^{-5} \text{ cm}^2 \text{ s}^{-1}$  at  $T = 470 \text{ K}$ , consistent with the experimental value, was reported.

The potential from work [80] was employed in Ref. [101] to simulate cavitation in liquid lithium under negative pressures.

**3.1.2 Sodium.** Certain data on liquid sodium simulation can be found in Ref. [5]. In paper [102], the effective pair interaction potential for sodium atoms was calculated by the pseudopotential method, and liquid and amorphous Na models under  $0$  and  $2 \text{ GPa}$  were constructed and their structural characteristics determined. Liquid sodium models containing 54 and 60 atoms at  $378 \text{ K}$  were developed by the *ab initio* method [100].

The EAM potential for liquid sodium was calculated in Refs [55, 56, 60]. For  $r > r_1 = 2.55 \text{ Å}$ , the pair contribution to the potential was described by the piecewise continuous function in the form

$$\varphi(r) [\text{eV}] = \sum_{i=1}^k \sum_{n=0}^L a_{in}(r - r_{i+1})^n H(r_i, r_{i+1}) \quad \text{for } r > r_1. \quad (17)$$

Here,  $k = 10$ ,  $L = 6$ , and function  $H(r_i, r_{i+1})$  is unity in the  $r_i < r \leq r_{i+1}$  interval, and nil in the remaining intervals. The zero interval starts as  $r < r_1$ . Formula (17) describes the pair contribution to the potential for 1–10 intervals. Coefficients  $a_{in}$  are reported in Refs [55, 56]. The potential is truncated at  $r = 10.78$  Å. The  $r_1$  is determined by a minimal distance between particles at temperatures close to melting point. The Schommers algorithm provides no information about the potential for  $r < r_1$ . Therefore, the potential for  $r < r_1$  was specified by the formula

$$\varphi(r) [\text{eV}] = 0.786149 \exp [1.2(2.55 - r)],$$

where  $r$  is expressed in angströms. The slope of the potential in this region was found empirically, and the pair contribution  $\varphi(r)$  thus obtained is depicted in Fig. 1.

The sodium embedding potential [55, 56] was chosen in the form (5)–(10), the coefficients entering formulas (6)–(8) were fitted from liquid sodium density, and coefficients in formulas (9) and (10) from the form of the shock Hugoniot for sodium. The Na embedding potential is plotted in Fig. 3.

Similar to lithium, sodium was simulated in the temperature range 298–2300 K. The properties of sodium models close to the melting point under normal pressure are presented in Table 2, and at temperatures up to 2300 K in Table 3. The models have near-zero pressure, so that the EAM potential fairly well describes the temperature–density relationship. Discrepancies  $R_g$  between model and diffraction PCFs [89, 90] are small; therefore, the model structure resembles the actual one. Model energy, bulk compression modulus  $K_T$ , and self-diffusion coefficient  $D$  are consistent with experimental values. Electron contribution  $E_{el}$  was estimated on the assumption that electron thermal capacity coefficient  $\gamma_0 = 1.38 \text{ mJ K}^{-2}$  [93, 94];  $E_{eT}$  was calculated by formulas (11). Accounting for the electron energy improves the agreement with experiment for the energy at high temperatures.

The two-phase liquid–vapor system at 400–2000 K was simulated in Ref. [95] using the EAM potential from Ref. [69]. Each sodium model contained 8,000 atoms in the basic cell. The liquid phase formed a flat layer. Atomic aggregation occurred in the gaseous phase. The transition layer did not undergo stratification. The critical temperature (2462 K), density ( $0.3493 \text{ g cm}^{-3}$ ), and pressure (113 bar) of sodium were deduced from the temperature dependence of the phase density. The calculated values of the sodium self-diffusion and viscosity coefficients were consistent with experimental findings.

The results of shock experiments were utilized to calculate parameters of the embedding potential for strongly compressed Na [83–87]. Figure 4 shows the sodium shock Hugoniot. These data can be approximated by the polynomial

$$p [\text{GPa}] = 6024.30Z^4 - 17101.3Z^3 + 18119.7Z^2 - 8539.23Z + 1523.15. \quad (18)$$

Expression (18) was tapped to calculate the parameters of the embedding potential (5)–(10) (see Fig. 3). The properties of the constructed sodium models are collected in Table 4. The models had a crystalline structure for  $Z > 0.55$ . Figure 4 shows evaluated pressure  $p_{\text{calc}} = p_M + p_{eT}$ . Calculated and experimental values are in excellent agreement; the mean deviation is 0.41 GPa. Equally good agreement was

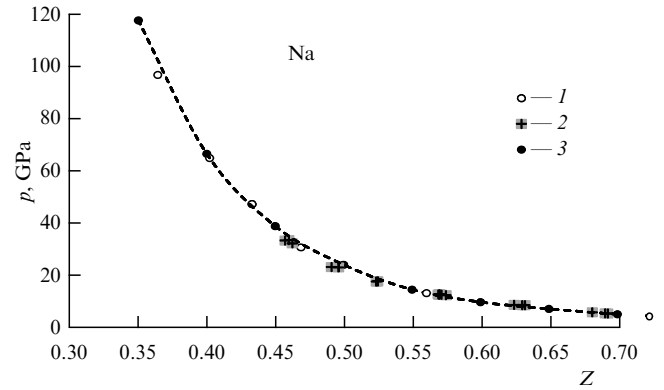


Figure 4. Sodium shock Hugoniot: 1 — data from Ref. [84], 2 — data from Ref. [86], and 3 — molecular-dynamic data:  $p_{\text{calc}} = p_M + p_{eT}$ .

documented between calculated and MD energies (mean deviation of  $0.39 \text{ kJ mol}^{-1}$ ).

Thus, the EAM potential reported in this section is quite acceptable to describe strongly compressed sodium states.

The electron contribution to the energy increases with temperature; at  $Z = 0.35$ , the thermal energy of electrons amounts to 22% of the total energy. Subtraction of electron thermal energy from the potential energy of a metal lowers the temperature in comparison with its value calculated by the standard method [88].

The sodium phase diagram in Ref. [103] was constructed at pressures of up to  $\sim 140$  GPa. It showed a high peak at  $\approx 32$  GPa and 1000 K. As pressure grew further, the equilibrium line rapidly went down to 300 K at  $\approx 120$  GPa. In Refs [64, 65, 97], the sodium phase diagram was calculated by two quantum MD methods (density functional theory+Lindemann's criterion and BOMD). The former method revealed an excellent agreement with experiment for the shape of the equilibrium line at pressures of up to 100 GPa. The BOMD method yielded less convincing results.

In Ref. [69], the bcc-sodium melting was simulated by the heat-up method. The melting temperature of the models was 358 K at standard pressure (real value is 371 K). At 10 GPa and the EAM potential taken from Refs [55, 56], the calculated  $T_m$  was close to 1200 K and proved overestimated in comparison with the value for real sodium ( $\sim 750$  K [96, 99]). MD calculations with the use of the EAM potential yielded similar results in a pressure range of 35–50 GPa [69]. The cause behind the discrepancy appears to be the inadequacy of the EAM potential for crystalline Na. At 298 K, the pressure of the bcc-sodium model at a real density of  $0.966 \text{ g cm}^{-3}$  is  $-0.107$  GPa, i.e., differs considerably from zero, even if not so much as in the case of lithium.

Table 6 presents structural characteristics of sodium models, viz. coordinate  $r_{00}$  of the point at which PCF vanishes, coordinate  $r_1$  of the first PCF peak and its height  $g(r_1)$ , coordination number, and topological parameter  $\rho_t = r_1(N/V)^{1/3}$  that serves as a measure of structural looseness. For dense noncrystalline structures, it was reported that  $\rho_t = 1.08 \pm 0.02$  [20], and for the loose structure of vitreous silica,  $\rho_t = 0.930$ . The coordination number was calculated up to the coordinate of the PCF minimum when it was identified. Generally, parameters of the sodium structure along isobar  $p \approx 0$  show smooth dependence on temperature. The liquid structure is somewhat loose and contains voids (pores) at temperatures above 573 K. The error in CN determination in states 4–8 is great (see Table 6) due to the

**Table 6.** Structural characteristics of sodium models obtained by the MD method with EAM potential ( $r_{00}$ —coordinate of the point at which PCF vanishes).

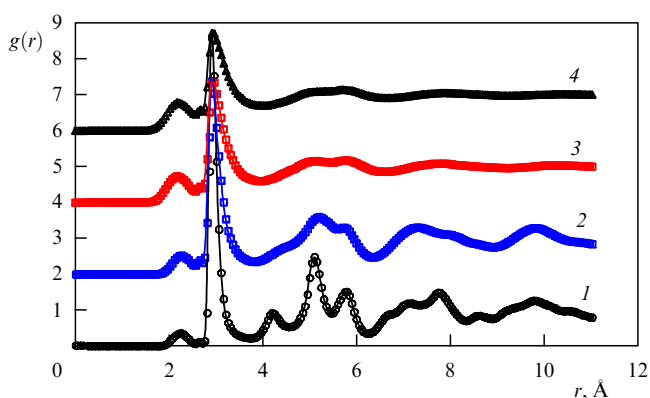
State	$T$ , K	$d$ , g cm <sup>-3</sup>	$r_{00}$ , Å	First PCF peak		Coordination number	$\rho_t$
				$r_1$ , Å	$g(r_1)$		
1	378	0.9239	2.84	3.69	2.50	13.5 ± 1.1	1.083
2	473	0.9041	2.80	3.69	2.28	13.3 ± 1.2	1.046
3	573	0.8688	2.80	3.73	2.10	13.0 ± 1.3	1.061
4	823	0.8196	2.75	3.70	1.86	?	1.043
5	1200	0.7309	2.65	3.91	1.66	?	1.004
6	1500	0.6561	2.35	3.80	2.31	?	0.997
7	2000	0.5097	2.30	3.95	1.68	?	0.844
8	2300	0.3793	1.90	3.75	2.07	?	0.762
9	400	2.148	1.85	2.25; 2.91*	0.035; 8.55	0.48 ± 0.6**	1.042
10	700	2.148	1.75	2.25; 2.90*	0.521; 5.37	0.82 ± 0.7**	—
11	1000	2.148	1.55	2.15; 2.86*	0.737; 3.34	1.34 ± 0.8**	—
12	1300	2.148	1.55	2.15; 2.90*	0.779; 2.72	1.60 ± 0.8**	—

\* Pre-peak and main peak.  
 \*\* Pre-peak coordination number.

insufficiently deep minimum of PCF to the right of the first peak or its absence for  $T > 2000$  K.

MD calculations for liquid sodium with densities 2.00–2.75 times the standard value revealed state regions in which the derivative  $(\partial p/\partial T)_V$  was negative (water type anomaly) [69]. Heat capacity  $C_V$  in this pressure interval (25–65 GPa) was abnormally high (up to 56 J mol<sup>-1</sup> K<sup>-1</sup>) and reflected endothermal effects of the structural modification of liquid Na. Visual analysis of atomic arrangement in liquid sodium models showed that the regular crystalline bcc-structure at  $T = 300$  K is conserved under compression up to  $Z = 0.6$  ( $Z = V/V_0$ , where  $V$  is the volume, and  $V_0 = 23.79$  cm<sup>3</sup> mol<sup>-1</sup> is the normal sodium volume). Further compression causes atomic rows to bend and the structure factor to decrease; as a result, the lattice loses stability at  $Z = 0.45$  and the model becomes amorphous. The structure of Na changes substantially in the region of anomalous properties.

Figure 5 presents the PCF of sodium models at  $Z = 0.45$  and  $T = 400, 700, 1000, 1300$  K [69]. At  $T = 400$  K, the model retains the crystalline structure with the maximum value of the structure factor  $S_{\max}(\mathbf{K}) = 1072$  ( $\mathbf{K}$  is the scattering vector; for an ideal crystal at absolute zero,  $S_{\max}(\mathbf{K}) = N = 2000$ ); however, a small pre-peak at a distance of 2.25 Å appears on the PCF. At 700 K, the structure factor  $S_{\max}(\mathbf{K}) = 1026$  still

**Figure 5.** Pair correlation functions of strongly compressed sodium at  $Z = 0.45$ : 1— $T = 400$  K, 2— $T = 700$  K, 3— $T = 1000$  K, and 4— $T = 1300$  K.

suggests a high degree of model crystallinity. When  $T = 1000$  and 1300 K,  $S_{\max}(\mathbf{K})$  sharply decreases to 17–18 and the models undergo transition to the liquid state. Isochoric heating increases the PCF pre-peak. Table 6 gives coordinates and heights of both the pre-peak and the main peak, as well as coordination numbers of pre-peak atoms. It can be seen that the pre-peak reflects groups of closely located atoms with low CN, largely 1–3. However, at  $T = 1300$  K, the model involves as many as 19 atoms with CN = 4. The effective diameter of ‘pre-peak’ atoms can be estimated from coordinate  $r_1$  (see Table 6); it is  $\approx 0.57$  of the ‘normal’ atom diameter.

In order to analyze the spatial distribution of the atoms contributing to the PCF pre-peak (pre-peak atoms), a search for connected groups (clusters) formed by the pre-peak atoms was undertaken. A cluster had to meet the condition that each of its members have a neighbor from the same group spaced less than 2.55 Å apart. An appreciable increase in the number of pre-peak atoms and their clusterization occurred in the interval  $Z = 0.45 - 0.40$ . A rise in temperature stimulated formation of pre-peak atoms. For example, their total number increased in the case of  $Z = 0.450$  from 835 at  $T = 400$  K to 1838 at  $T = 1300$  K. Because this processes drew atoms closer together, it was responsible for the anomalous temperature dependence of density, negative values of derivatives  $(\partial V/\partial T)_p$ ,  $(\partial p/\partial T)_V$  in the temperature range from 500 to 1300 K, and enhanced thermal capacity. At  $Z = 0.363$ , almost all atoms of the model occupy states of pre-peak atoms and were brought together into a single large cluster.

Increased concentration of pre-peak atoms under compression results in a decrease of their average size. This leads to enhanced diffusion mobility imposed on the usual decrease in mobility under the effect of compression. As a result, intermediate maxima appear on temperature and density dependences of the self-diffusion coefficient over the interval  $0.4 < Z < 0.6$  [69].

The possibility of transition from a highly symmetric crystalline structure to a less symmetric one under high pressures is theoretically discussed in Ref. [66].

**3.1.3 Potassium.** The pseudopotential pairwise potential was utilized in Ref. [104] to calculate the structural characteristics of liquid potassium using integral equations of the theory of

**Table 7.** Calculated properties of potassium, rubidium, and cesium obtained by the MD method with EAM potential.

No.	$T$ , K	$d$ , g cm <sup>-3</sup>	$p_{\text{EAM}}$ , GPa	$\langle \rho \rangle$	$R_g$	$U$ , kJ mol <sup>-1</sup>				
						EAM	$E_{\text{el}}$	$E_{\text{eT}}$	EAM + $E_{\text{eT}}$	Experiment [81]
1	2	3	4	5	6	7	8	9	10	11
Potassium										
1	343	0.8278	0.005	$0.994 \pm 0.069$	0.028	-79.00	0.12	0.024	-78.76	-79.09
2	473	0.7986	-0.029	$0.954 \pm 0.090$	0.040	-75.32	0.23	0.121	-75.21	-75.01
3	723	0.7401	-0.008	$0.873 \pm 0.117$	0.072	-68.13	0.54	0.412	-67.72	-67.44
4	1000	0.6735	-0.002	$0.779 \pm 0.131$	—	-60.93	1.04	0.920	-60.01	-59.11
5	1500	0.5455	-0.031	$0.616 \pm 0.130$	—	-44.94	2.34	2.495	-42.44	-42.13
6	2200	0.2712	0.031	$0.366 \pm 0.189$	—	-14.94	5.03	8.195	-6.74	-7.69
Rubidium										
1*	250	1.532	0.003	$1.035 \pm 0.058$	—	-76.60	0.11	-0.028	-76.63	-74.70
2	313	1.4785	-0.0045	$1.000 \pm 0.078$	0.018	-72.47	0.12	0.008	-72.46	-72.35
3	500	1.4065	-0.0004	$0.949 \pm 0.101$	0.018	-66.75	0.30	0.168	-66.58	-66.55
4	1000	1.1826	-0.0004	$0.794 \pm 0.135$	—	-52.48	1.20	1.068	-51.41	-51.2
6	1600	0.8702	-0.0150	$0.632 \pm 0.172$	0.068	-34.56	3.08	3.500	-31.06	-30.2
7	2000	0.5220	0.0124	$0.557 \pm 0.216$	—	-21.45	4.82	7.379	-14.07	-10.9
Cesium										
1*	298	1.8790	0.086	$1.022 \pm 0.055$	—	-68.89	0.16	0	-68.89	-70.31
2	323	1.8237	0.007	$1.001 \pm 0.087$	0.031	-65.89	0.17	0.017	-65.87	-65.97
3	573	1.6783	-0.016	$0.924 \pm 0.117$	0.029	-57.93	0.52	0.298	-57.63	-58.05
4	773	1.5684	-0.008	$0.869 \pm 0.132$	0.022	-52.10	0.96	0.664	-51.44	-52.16
5	1173	1.3286	-0.011	$0.745 \pm 0.154$	0.018	-40.85	2.20	1.865	-38.98	-40.17
6	1673	0.9550	0.007	$0.653 \pm 0.235$	0.099	-26.32	4.48	4.760	-21.56	-20.94
7	1923	0.5894	0.011	$0.520 \pm 0.251$	0.270	-14.51	5.92	8.153	-6.36	-7.62

\* Crystalline state.

liquids, such as the modified hyperchain and mean spherical equations. Calculated structure factors of potassium at  $T = 338$ – $973$  K are in excellent agreement with diffraction ones. Certain data on the simulation of liquid potassium are presented in Ref. [5]. MD simulation of liquid potassium and potassium–oxygen solutions with the employment of pair potentials is reported in Ref. [105].

The authors of Refs [54, 70] proposed the EAM potential and performed liquid potassium simulation along the  $p \sim 0$  isobar at temperatures of up to 2200 K. The pair contribution to the interaction potential was evaluated by applying the Schommers algorithm in the form of a data table. In Refs [55, 56], it was approximated for  $r > 3.60$  Å by a power series of interparticle distances. The cutoff radius of interaction was put to 9.57 Å. Accordingly, for  $r \leq 3.60$  Å, the potential was described by an exponent, in analogy with potentials for Li and Na. The pair contribution to the potassium potential is demonstrated in Fig. 1. Parameters of the embedding potential (5)–(8) for liquid potassium under low pressure were determined from the temperature dependence of its density in Refs [55, 56, 60]. The potassium embedding potential is displayed in Fig. 3.

Potassium simulation [55, 56] was performed at  $T = 200$ – $2200$  K, similar to Li and Na cases. Results of MD calculations are presented in Tables 2 and 7. They are consistent with experimental data for pressure, energy, and bulk compression modulus, whereas theoretical and experimental self-diffusion coefficients are markedly different. The diffraction PCFs needed for comparison with model values were borrowed from Refs [89, 90]. In the case of potassium, the discrepancy between the model and diffraction PCFs is

insignificant at  $T = 343$  K but markedly increases upon heating to  $T = 723$  K.

Electron contribution  $E_{\text{el}}$  to the total potassium energy was estimated on the assumption that electron thermal capacity coefficient  $\gamma_0 = 0.28$  mJ K<sup>-2</sup> [93, 94], and  $E_{\text{eT}}$  was calculated by formula (11). Accounting for the electron contribution permits obtaining good agreement of model pressure and energy (column 10, Table 7) with experimental data (column 11) at all temperatures up to 2200 K.

Results of the static compression of potassium at 4.5 GPa are reported in Refs [82, 106], and at up to 52.9 GPa in Ref. [107]. The EAM potential selected in Ref. [54] enabled us to fairly well describe the data on static compression of crystalline potassium ('potential A'). In Ref. [60], we used results of shock tests of potassium under 50 GPa [84–87]. Figure 6 depicts the potassium shock Hugoniot. These data can be approximated by the polynomial

$$p \text{ [GPa]} = -0.633756 \times 10^3 + \frac{0.145929 \times 10^4}{Z} - \frac{0.131948 \times 10^4}{Z^2} + \frac{0.585789 \times 10^3}{Z^3} - \frac{0.127078 \times 10^3}{Z^4} + \frac{0.109280 \times 10^2}{Z^5} \quad (19)$$

( $Z = V/V_0$ , where  $V_0 = 45.56$  cm<sup>3</sup> mol<sup>-1</sup>). The embedding potential was given by expressions (5)–(10). The parameters of the potential responsible for compressed states were calculated by analogy with the Li and Na cases. The potassium embedding potential is plotted in Fig. 3.

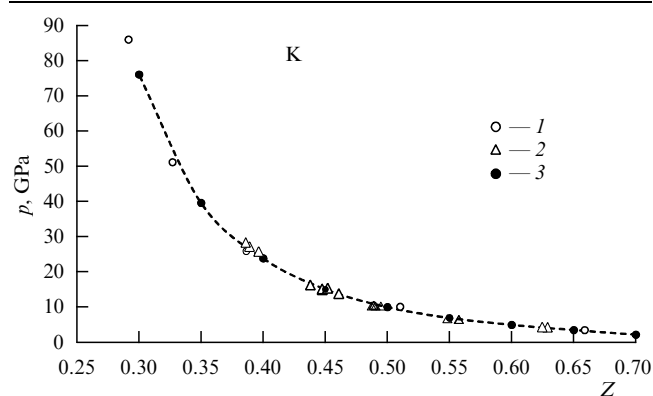
**Table 8.** Properties of potassium, rubidium, and cesium models under shock compression [60].

$Z$	$p$ , GPa, Expt.	$U_2 - U_1$ , kJ mol <sup>-1</sup> , from (13)	$T$ , K, model	$T$ , K [88]	$\mu$ , eV	$E_{eT}$ , kJ mol <sup>-1</sup> , from (11)	$p_{eT}$ , GPa	$E_M$ , kJ mol <sup>-1</sup> , from (16)	$E_{MD}$ , kJ mol <sup>-1</sup>	$p_M$ , GPa, model	$p_M + p_{eT}$ , GPa
1	2	3	4	5	6	7	8	9	10	11	12
Potassium											
1.00*	0	0	298	300	2.041	0.080	0	-82.88	-82.01	0.134	0
0.70*	1.72	11.71	300	640	2.589	0.000	0.00	-71.17	-71.10	2.02	2.02
0.60	5.15	46.85	1090	1220	2.867	0.675	0.02	-36.70	-36.51	4.78	4.80
0.50	9.66	109.84	2560	3048	3.228	3.501	0.11	23.46	23.44	9.73	9.84
0.40	23.87	325.63	9340	9715	3.606	37.580	1.38	205.17	205.75	22.30	23.68
0.35	39.41	582.37	17,800	—	3.546	106.40	4.45	393.09	392.81	35.00	39.45
0.30	74.02	1177.8	38,250	—	2.063	313.7	15.33	781.22	780.7	60.60	75.93
Rubidium											
1.00*	0	0	300	300	1.779	0.000	0.00	-74.67	—	0.00	—
0.60*	1.71	19.17	300	1202	2.501	0.000	0.00	-55.50	-54.77	2.84	2.84
0.50	8.08	112.89	3340	2980	2.800	6.809	0.17	31.41	31.53	7.74	7.91
0.40	19.36	324.42	10,170	10185	3.060	48.62	1.45	201.13	201.60	18.85	20.30
0.37	32.19	566.52	18,600	—	2.695	125.60	4.05	366.25	366.50	28.37	32.42
0.35**	48.39	878.54	29,520	—	1.695	240.70	8.21	563.18	564.10	39.40	47.61
Cesium											
1.00*	0	0	300	—	1.517	0.000	0	-70.40	-69.83	0.05	0.05
0.45	5.87	115.1	3300	—	2.557	7.244	0.16	37.46	37.22	5.88	6.04
0.40	12.9	275.0	9240	—	2.581	46.20	1.09	158.4	158.3	12.18	12.27
0.36	27.1	616.3	21,400	—	1.815	164.8	4.30	381.0	380.23	22.64	26.94
0.32**	49.1	1184	40,280	—	-0.516	374.05	10.99	739.55	709.42	38.15	49.14

\* Crystalline state. \*\* Extrapolated.

Results of calculations are collected in Table 8. Figure 6 shows calculated potassium pressure  $p_{\text{calc}} = p_M + p_{eT}$ . This is consistent with experimental values taking into account electron thermal pressure (columns 2 and 12), with an average discrepancy of 0.22 GPa between the two. An equally good agreement is documented between actual and model energies, bearing in mind electron thermal energy (columns 9 and 10, with an average discrepancy of 0.26 GPa). This means that the EAM potential reported in Ref. [60] is well acceptable in describing strongly compressed potassium states.

Electron contribution to the total energy increases with temperature and at  $Z = 0.30$  the thermal energy of conduction electrons (313.7 kJ mol<sup>-1</sup>) comprises 29% of

**Figure 6.** Potassium shock Hugoniot: 1—data from Ref. [84], 2—data from Ref. [86], and 3—molecular-dynamic data:  $p_{\text{calc}} = p_M + p_{eT}$ .**Table 9.** Melting temperature of potassium models.

$p$ , GPa	0.0	2.35	4.60	8.60	17.5	30.0	41.2
$T_m$ , K	319	466	581	681	794	994	1231

the total energy (the latter amounts to  $313.7 + 781.2 = 1094.9$  kJ mol<sup>-1</sup>). Temperature on the shock Hugoniot is evidently lower than that calculated using the standard method [88].

The melting temperature was evaluated by the heat-up method. For potassium models at standard pressure, it was  $(319 \pm 1)$  K versus real  $T_m = 336.4$  K and monotonically increased with increasing pressure (Table 9). Agreement with experiment [99] was reached at pressures of up to 5 GPa; at higher pressures, the calculated curve was somewhat above the actual one.

**3.1.4 Rubidium.** The effective pair interaction potential for rubidium at 350–2000 K was calculated in Ref. [108] from the structure factor by the Reatto method [18] with the involvement of the Ornstein–Zernike equation for a disordered fluid. The slope of the repulsive potential curve became less steep with decreasing density, whereas the long-range character of the attractive part of the interaction potential was more pronounced. The nearly free electron model stops working at about 2000 K. The pair potential fairly well describes particle dynamics over the temperature range from the triple point to the vicinity of the critical temperature [109].

The author of this review performed the simulation of crystalline and liquid rubidium by the MD method using EAM potentials [55, 56, 71, 73]. Pair contribution to the

interaction potential was obtained with the help of the Schommers algorithm. Liquid rubidium was simulated along the  $p = 0$  isobar at 2000 K in Ref. [71], and correction of the potential for the description of strongly compressed states was undertaken in paper [73]. In Refs [55, 56, 60], the pair contribution to the potential was approximated by a power series of interparticle distance for  $r > 3.70$  Å. The cutoff radius of interaction was put to 14.35 Å. Accordingly, for  $r \leq 3.70$  Å, the potential was described by an exponent. The pair contribution to the rubidium EAM potential is shown in Fig. 1. The embedding potential was given by expressions (5)–(8).

The results of simulation near the melting point are presented in Table 2, and at temperatures up to 2000 K in Table 7. The structures were compared using diffraction PCFs taken from Refs [89, 90, 110]. Discrepancies  $R_g$  turned out to be relatively small, even at  $T = 1600$  K. The electron thermal capacity coefficient was assumed to be  $\gamma_0 = 2.41 \text{ mJ mol}^{-1} \text{ K}^{-2}$  [93, 94]. Calculations by formulas (11) gave the values of thermal energy  $E_{eT}$  rather close to  $E_{el}$  at temperatures up to 1400 K. The consideration of electron contribution substantially improved the agreement between theoretical (column 10, Table 7) and experimental (column 11, Table 7) data for rubidium energy at temperatures of up to 1600 K.

For rubidium, the volume dependence of pressure was demonstrated both under static conditions at pressures up to 4.5 GPa [82, 106], and 48 GPa [107] and under shock compression (up to 39 GPa) [83, 86, 87]. The shock Hugoniot for rubidium is depicted in Fig. 7. It is approximated by the formula

$$p [\text{GPa}] = \frac{13.429}{Z^4} - \frac{67.088}{Z^3} + \frac{75.031}{Z^2} + \frac{88.590}{Z} - 147.38. \quad (20)$$

Accounting for these data allows one to calculate the rubidium embedding potential (see Fig. 3). Figure 7 shows the calculated pressure  $p_{\text{calc}} = p_M + p_{eT}$ . There is a good agreement between theoretical and experimental pressures (columns 2 and 12, Table 8), the average discrepancy being 0.46 GPa. Real and simulated energies satisfactorily agree as well, taking account of electron thermal energy (columns 9 and 10; average discrepancy  $0.43 \text{ kJ mol}^{-1}$ ). In other words, the EAM potential proposed in Refs [55, 56, 60] may well be accepted to describe strongly compressed rubidium states. Model temperatures are rather similar to those calculated by

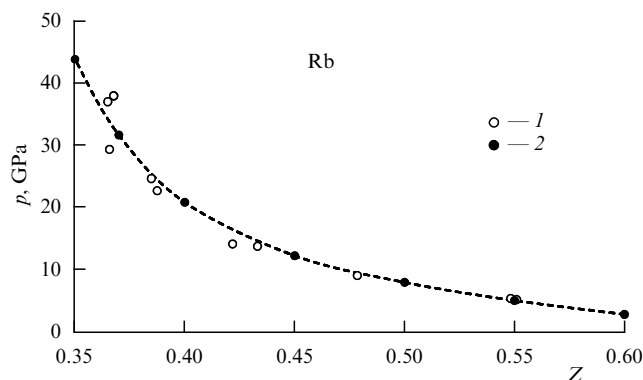


**Figure 7.** Rubidium shock Hugoniot: 1—data from Ref. [86], and 2—molecular-dynamic data:  $p_{\text{calc}} = p_M + p_{eT}$ .

the standard method [88]. The electron contribution to the total energy increases with temperature. At  $Z = 0.37$ , the thermal energy of conduction electrons ( $125.60 \text{ kJ mol}^{-1}$ ) comprises 26% of the total energy ( $125.60 + 366.50 = 491.10 \text{ kJ mol}^{-1}$ ).

A rubidium phase diagram was constructed in Ref. [111] under pressures of up to 15 GPa. The crystal–liquid equilibrium line passes through a maximum at  $p = 5$  GPa ( $T = 553$  K). The melting temperature at different degrees of compression was determined in Ref. [73] by the heat-up method. Model temperature  $T_m \approx 328$  K at a near-zero pressure was close to the real one for rubidium (312.46 K). As the pressure increased, the temperature passed through a flat maximum ( $\approx 480$  K) in the vicinity of  $p = 2$  GPa, then slightly decreased, and increased again thereafter to  $(841 \pm 2)$  K at  $p = 9$  GPa. These results are consistent with experimental findings [99, 111] for  $p < 2$  GPa. The MD method does not permit determining melting temperature at a pressure above 10 GPa, because the models undergo amorphization even at moderate temperatures.

The mechanism of crystallization of liquid rubidium with the pairwise interaction potential from Ref. [113] (corrected for distances smaller than 3.75 Å) was elucidated in Refs [72, 112]. Equilibrium crystallization temperature  $T_m$  of the models, determined by the heat-up method, run to  $(313 \pm 1)$  K versus actual  $T_m \approx 312.46$  K. The structure was described in terms of the number of atoms with type 0608 and 0446 Voronoi polyhedrons (VPs) and the formation of connected groups (clusters) from such atoms. Strong overcooling down to 70.0–182.5 K (but not higher!) led to solidification of the liquid largely into the bcc-structure. Atoms of the liquid with type 0608 and 0446 VPs serve as some sort of ‘catalyst’ for the rubidium crystallization process. Atoms emerging in the overcooled state with such coordination are energetically preferable as compared to other atoms. At first, they are chaotically distributed in the liquid (or amorphous phase) but gradually aggregate into clusters with a moderate gain of energy. Initially, connected atomic groups have a loose structure, including many atoms with other types of VPs, the linear size of the largest group rapidly approaching the size of the basic cube. Type 0608 clusters grow by attracting smaller aggregates in a process resembling coagulation of an admixture from an oversaturated solution [114–116]. In this process, part of the model atoms pass into the realm of the 0608 atoms. Further cluster growth occurs through the alignment of ‘extraneous’ atoms located inside and near the cluster into the desired coordination with transformation of their VPs into types 0608 or 0446. No relationship between the probability of formation of a connected group of a given size and the size of the model was documented.

The length of MD-runs prior to the onset of crystallization is usually a few dozen thousand time steps but may be different in individual experiments at the same temperature. An important role in the formation of a 0608-cluster of the threshold (‘critical’) size is played by fluctuations of cluster size, especially pronounced in the temperature range from 180 to 185 K (Fig. 8). The onset of solidification is apparent from the appearance of a large connected group having the threshold size  $N_c$  that does not decrease (may only increase) in the course of further simulation, and from the fact that the structure factor exceeds a certain threshold value  $S_c$  in any direction. The threshold size of a 0608-cluster (nucleus) covers 120–150 atoms and shows no regular dependence on

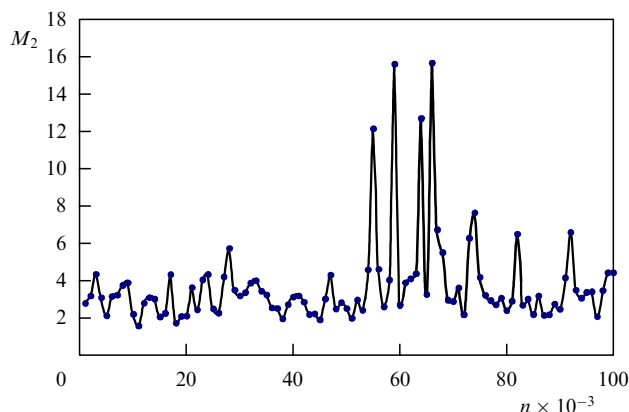


**Figure 8.** Time-dependent behavior of the mean size of 0608-clusters in an Rb model. The number of atoms  $N = 1968$ ,  $T = 185$  K;  $n$ —number of time steps.

temperature. Also, the maximum values of structure factors in the threshold state (104–130) are roughly identical. This result is at variance with the classical nucleation theory, where the critical nucleus size decreases with overcooling.

Thus, the mechanism of rubidium solidification caused by strong overcooling is different from that postulated by the classical nucleation theory. Solidification is mediated through an avalanching increase in the number of atoms with type 0608 and 0446 VPs, the clusterization of these atoms, and the growth of the clusters. This ‘cluster’ mechanism (see Ref. [72]) is inherent in strongly overcooled liquids. It was also observed in cooled MD-models of silver and nickel (see Sections 3.2.2 and 9.3). In the case of rubidium, it is realized at temperatures below 183 K, which is, therefore, the *lower overcooling limit* ( $T_b$ ). Solidification by this mechanism ends in crystallization, given that the system remains long enough in a temperature range below  $T_b$  and its atoms display diffusion mobility needed for structure transformation. If this time is not long enough, rapid cooling leads to amorphization.

The *ab initio* method was applied in Ref. [171] for liquid rubidium simulation at 350–1400 K (54 atoms in the basic cube having the edge from 17.38 to 19.92 Å in length). The PCF was consistent with diffraction data. The authors managed to evaluate self-diffusion coefficients and obtain electron density profiles. At  $T = 35$  K, electrons were smeared out over the entire volume, except regions around ions. At  $T = 1400$  K, electrons tended to be localized due to developed fluctuations of atomic density. They accumulated in the regions occupied by closely approached atoms. The density of states was very similar to that in the free electron model. The fraction of d-states in the total electron density increased appreciably at 520–570 K as pressure enhanced to 6.1 GPa.

*Ab initio* simulation of rubidium at different densities between 350 and 2000 K is described in Ref. [118]. The models contained either 54 or 250 atoms per cell. Static structure factors and PCFs were calculated. The coordination number decreased upon heating from 8.0 (density of  $1.45 \text{ g cm}^{-3}$ ) to 2.5 (density of  $0.61 \text{ g cm}^{-3}$ ). Certain pairs of atoms approached to each other were revealed, serving as dimer precursors. The electron concentration between these atoms was elevated.

In Ref. [119], rubidium was simulated by *ab initio* and LMTO (linear muffin-tin orbitals) methods at temperatures up to 2200 K. The self-diffusion coefficient was consistent

with the viscosity-assisted estimate obtained using the Stokes–Einstein formula. Also, an agreement was achieved with the results of electrical conductivity experiments.

**3.1.5 Cesium.** In Refs [78, 120], the pair contribution to the cesium EAM potential was evaluated using the Schommers algorithm in the form of a table. In Refs [55, 56, 60], this pair contribution was represented in an analytical form. The cutoff radius of interaction was put on 13.15 Å. The pair contribution to cesium EAM potential is shown in Fig. 1. The parameters of the cesium embedding potential were selected from the temperature dependence of metal density.

Cesium models were constructed at temperatures ranging 298–1923 K [55, 56]. The results of calculations by the MD method near  $T_m$  are presented in Table 2. Low enough pressure values and discrepancies  $R_g$  between diffraction [121] and model PCFs were obtained at all temperatures up to 1600 K (see Table 7). Accounting for the electron contribution significantly improved the agreement with experimental data on the energy.

The properties of liquid cesium under high pressures were studied by static (up to 9.8 GPa in Ref. [122] and 5 GPa in Ref. [123]) and shock (up to about 40–43 GPa [83, 87]) compression techniques. In Ref. [78], the EAM potential was applied to simulate strongly compressed cesium. The volume dependence of pressure along the shock Hugoniot presented in Fig. 9 is well approximated by the expression

$$p [\text{GPa}] = -4.579855 \times 10^2 Z^3 + 2.923059 \times 10^3 Z^2 - 2.377560 \times 10^3 Z + 5.255829 \times 10^2. \quad (21)$$

The embedding potential of liquid cesium in Ref. [60] was chosen in the form (5)–(10) (see Fig. 3).

The results of calculations are displayed in Fig. 8. Figure 9 also shows calculated pressure:  $p_{\text{calc}} = p_M + p_{eT}$ . The agreement between real and model pressures was almost anywhere good (columns 2 and 12, the average discrepancy being 0.32 GPa). Actual and simulated energies were in equally good agreement (columns 9 and 10; average discrepancy being  $0.78 \text{ kJ mol}^{-1}$ ). The electron thermal energy at  $Z = 0.33$  equaled  $322.2 \text{ kJ mol}^{-1}$  and accounted for 33% of the total cesium energy ( $627.0 + 322.2 = 949.2 \text{ kJ mol}^{-1}$ ).

The melting temperature of cesium models may be determined by the heat-up method. The results obtained using the EAM potential from Ref. [78] are given in Table 10. The melting temperature passes through a minimum at a pressure of roughly 1 GPa. The actual melting

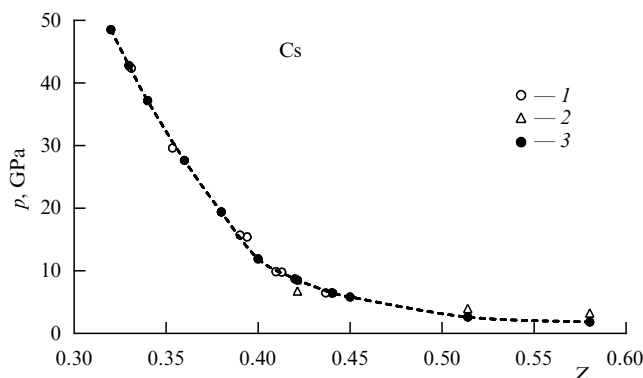


**Figure 9.** Cesium shock Hugoniot: 1—data from Ref. [83], 2—static data [122], and 3—molecular-dynamic data:  $p_{\text{calc}} = p_M + p_{eT}$ .



**Table 10.** Melting temperature of cesium models.

$Z = V/V_0$	1	0.90	0.80	0.70	0.60	0.50	0.40	0.35
Pressure, GPa	0	0.32	0.68	1.07	1.63	2.78	7.22	14.00
$T_m$ , K	363	338	165	96	143	160	250	473

temperature under standard pressure equals 301.8 K; it passes through two maxima (473 and 471 K) under 2 and 3 GPa, and thereafter through a minimum (360 K) at  $p = 4.1$  GPa. Finally, the temperature rises again to 498 K at  $p = 5.5$  GPa [99]. Calculations with the EAM potential considerably underestimate  $T_m$  at pressures above 0.5 GPa, even though they reveal the minimum.

The *ab initio* method was employed to simulate cesium in Refs [124, 125]. In paper [124], simulation was performed for  $T = 323$ – $1673$  K and densities from  $1.83$  to  $0.96$  g cm $^{-3}$  (125 atoms per cell); also, structural and diffusion characteristics were calculated. Good agreement of structure factors with experiment was obtained, while the coordination number decreased almost linearly with increasing temperature from  $6.6$ – $7.5$  to  $3.1$ – $4.0$ . Models reported in paper [125] contained 54 atoms in the cell (total of 378 electrons). On the whole, these data were consistent with the results of classical simulation using the pair potential derived by the Schommers algorithm and the EAM potential. However, self-diffusion coefficients  $D$  were different in magnitude. In Ref. [125], coefficient  $D$  almost linearly increased with temperature and equaled  $40 \times 10^{-5}$  cm $^2$  s $^{-1}$  at 1600 K, while simulation with the EAM potential yielded  $D \sim 70 \times 10^{-5}$  cm $^2$  s $^{-1}$  [78]. These data allow one to verify the satisfiability of the Stokes–Einstein relation

$$D = \frac{k_B T}{6\pi\eta r_i}, \quad (22)$$

where  $r_i$  is the effective ion radius, and  $\eta$  is dynamic viscosity. Usually, relation (22) is fairly well satisfied if the radius of a singly-charged ion (1.65 Å for cesium) is taken as  $r_i$ . The values of  $D$  calculated in Ref. [78] from viscosity data (see Ref. [81]) are in excellent agreement with those obtained by the MD method using the EAM potential. *Ab initio* calculations underestimate  $D$  at  $T = 1600$  K by roughly 1.8-fold, while the ion effective radius entering into formula (22) increases with temperature.

**3.1.6 Main results for liquid alkali metals.** It follows from Table 1 that the EAM potential selected with regard to solid phase properties may not be quite suitable for the liquid phase. Conversely, the EAM potential selected taking into consideration the properties of the liquid phase alone, may prove unsuitable for the calculation of solid phase properties, melting temperature  $T_m$ , and other characteristics of a two-phase equilibrium. Table 11 collates calculated  $T_m^{\text{EAM}}$  values of alkali metals (involving EAM potential) with experimental  $T_m^{\text{exp}}$  values. The values of  $T_m^{\text{EAM}}$  are, on the average, 15–25 K higher or lower than  $T_m^{\text{exp}}$ . This discrepancy strongly increases at higher pressures for all metals, besides potassium (see Section 3.1.3). Melting temperatures inevitably differ if the interaction potential leads to incorrect values of melting heat  $\Delta H$  and volume change  $\Delta V$  during melting. For example, in sodium simulation with the EAM potential under zero pressure [55, 56], the difference in energy between the liquid state model and the bcc-model at  $T \approx 375$  K is  $2.35$  kJ mol $^{-1}$

**Table 11.** Calculated  $T_m$  of alkali metal models with the EAM potential.

Metal	$T_m^{\text{EAM}}$	$T_m^{\text{exp}}$
Li	428	453.7
Na	358	371.0
K	319	336.0
Rb	328	312.5
Cs	363	301.8

(real melting heat  $\Delta H = \Delta U = 2.70$  kJ mol $^{-1}$ ), while the densities of the bcc and liquid phases are  $0.9663$  and  $0.2966$  g cm $^{-3}$ , respectively. Therefore, the change in the volume during melting amounts to  $1.019$  cm $^3$  mol $^{-1}$ , compared with the actual value of  $0.64$  cm $^3$  mol $^{-1}$ . Using the Clausius–Clapeyron equation, one arrives at  $dT_m/dp = T\Delta V/\Delta H = 164$  K GPa $^{-1}$ . The real value of  $dT_m/dp$  equals  $85$  K GPa $^{-1}$  [99]. In other words, each additional 1-GPa increment of pressure increases the discrepancy between theoretically predicted and experimental melting temperatures by approximately 85 K.

Running sodium simulation revealed the anomalous behavior of models with a bcc-lattice, which is analogous to the anomalous behavior of water under high pressure. In a range of  $Z = 0.45$ – $0.50$ , the structural transformation of the model resulted in the appearance of groups of closely positioned atoms having a reduced effective diameter. The number of such atoms gradually increased in response to heating and compression. At  $T = 300$  K, the regular bcc-structure was retained at  $Z$  values down to  $0.6$ . Stronger compression caused atomic rows to bend and the model structure factor to diminish; as a result at  $Z = 0.45$  the lattice lost stability, and the model underwent amorphization. A rise in temperature stimulated the formation of pre-peak atoms accompanied by their approaching to each other, which resulted in the anomalous temperature dependence of density, negative derivatives  $(\partial V/\partial T)_p$ ,  $(\partial p/\partial T)_V$  for  $T = 500$ – $1300$  K, and enhanced heat capacity. At  $Z = 0.363$ , almost all atoms of the model passed into the state of pre-peak atoms and aggregated into one large cluster.

Simulation with the EAM potential was not associated with a marked reduction in the coordination number in liquid cesium at  $T = 623$  K and high pressures, as described in Ref. [122]. Such an effect is rather unusual in itself; in Refs [122, 123, 126], it was explained by 6s–5d hybridization and the appearance of type  $dsp^3$  directed bonds.

Self-diffusion coefficients in liquid metals are usually deduced from the slope of the time ( $t$ )-dependence of the mean square atomic displacement  $\langle(\Delta r)^2\rangle$  using the formula  $\langle(\Delta r)^2\rangle = 6Dt$ . The following self-diffusion coefficients of alkali metals were calculated (involving EAM potential) under standard pressure:

- $D = 2.688 \times 10^{-9} T^{1.7182}$  [cm $^2$  s $^{-1}$ ] in lithium for  $T < 3400$  K;
- $D = 2.861 \times 10^{-9} T^{1.6546}$  [cm $^2$  s $^{-1}$ ] in sodium for  $T < 2300$  K;
- $D = 3.233 \times 10^{-5} \exp(0.001941T)$  [cm $^2$  s $^{-1}$ ] in potassium for  $T < 2200$  K;
- $D = 9.605 \times 10^{-10} T^{1.81035}$  [cm $^2$  s $^{-1}$ ] in rubidium for  $T < 2000$  K;
- $D = 1.4896 \times 10^{-10} T^{2.0820}$  [cm $^2$  s $^{-1}$ ] in cesium for  $T < 1923$  K.

Diffusion in liquid metals occurs through the drift mechanism [127]. The error in a  $D$  prediction is usually small. For example, the ratio of calculated values to

**Table 12.** Mean square width of VP volume distribution  $\sigma_V$  for rubidium.

$T, \text{K}$	1900	1950	1975	2000	2025	2050	2100	2150
$\sigma_V, \text{\AA}^3$	338	341	356	394	351	357	344	317

experimental ones,  $D_{\text{MD}}/D_{\text{exp}}$ , at  $T \approx T_m$  for Li, Na, K, and Rb models with the EAM potential comprises 1.34, 1.05, 1.22, and 0.83, respectively. These deviations are insignificant, bearing in mind the usual experimental error of 10–15%. As a rule, the relationship between diffusion and viscosity is well described by the Stokes–Einstein equation (22).

The possibility of calculating the metal critical temperature by the MD method is rather doubtful, because matter loses its metallic properties near the critical point, and the potential is likely to change. Still, some attempts to check such a possibility have been reported. Specifically, critical temperature  $T_c$  for rubidium was estimated [71] in a series of models at a temperature ranging 1900–2150 K and a constant density of  $0.3631 \text{ g cm}^{-3}$  close to the critical density of rubidium. The mean square width of VP volume distribution  $\sigma_V$  (Table 12) passes through a maximum at  $T \approx 2000 \text{ K}$ . It is difficult to more accurately determine the critical temperature due to marked fluctuations of the structure and large deviations of volume distribution from the Gaussian one.

Another series of models was constructed for  $T = 773$ – $2500 \text{ K}$  and a constant density of  $0.431 \text{ g cm}^{-3}$  (close to the critical density) to estimate the critical temperature of cesium [78]. The temperature dependence of  $\sigma_V$  has the form of two linear segments intersecting at temperatures around 2000 K. The intersection point lies near cesium  $T_c$  (2043 K). Attempts to more accurately determine  $T_c$  have failed.

Our EAM potentials fairly well describe the behavior of liquid alkaline metals under shock compression. They can be chosen to build models of crystalline metals at temperatures near absolute zero and calculate the ‘cold pressure’ for comparison with the data of ‘standard’ calculations. The results are collated in Table 13. It was hardly possible to expect good agreement because the potentials were selected based on the properties of liquid phases and did not necessarily fit the crystalline phases. Nevertheless, in the majority of cases, the results of direct simulation and standard calculations agreed fairly well, especially for Li, K, and Rb. Taking account of electron contributions has to

increase the cold pressure, and this effect was well pronounced under strong compression for sodium, and less so for lithium.

The *ab initio* method permits us to calculate the electronic properties (spectra, density of states, conductivity, etc.), which is impossible applying the classical MD technique. As regards structural properties (PCFs, structure factors), this method yields results similar to those obtained with the use of EAM and pair interaction potentials. However, publications based on the application of the *ab initio* method suffer from a lack of data on the thermodynamic properties of the models. Therefore, the best strategy is to combine both techniques. This inference refers in the first place to construction of EAM potentials fitted to describe both crystalline and liquid phases.

### 3.2 Noble metals

The structure factors and thermodynamic properties of liquid Cu, Ag, Au, and Ni were calculated in Ref. [128] with the use of EAM potentials at temperatures close to the respective melting points; they proved consistent with the diffraction data. Analogous calculations for liquid Cu, Ag, Au, Ni, Pd, and Pt were made in Ref. [129]. Agreement between theoretical and experimental values was documented for structure factors, energy, and entropy of fluids at temperatures close to the melting point.

**3.2.1 Copper.** A few EAM potentials for copper are reported in the literature. Some of them are proposed to describe the crystalline phase (e.g., in paper [130]), but in papers [35, 131–136] the EAM potential was applied to describe a liquid metal. Reference [35] reports on a good agreement between theoretical and observed structures. Known EAM potentials were modified in Ref. [136], so as to improve the agreement with experiment for liquid Cu PCFs at  $T = 1373 \text{ K}$ .

EAM potentials for liquid copper constructed with the involvement of diffraction data on the metal structure near the melting point were calculated in Refs [135, 137]. Excellent agreement with experiment for the shape of PCF at 1573–1873 K was reached in paper [137]. The proposed potential fairly well described the properties of liquid copper under both low pressures and strong compression. In Ref. [131], the pair contribution to the interparticle interaction potential from Ref. [135] was approximated by function (17) with  $k = 4$  and  $L = 6$  (Fig. 10). The cutoff radius of interaction was put

**Table 13.** Cold pressure in alkali metals (bcc-lattice).

Metal	Data*	Degree of compression $Z$							
		0.9	0.8	0.7	0.6	0.5	0.45	0.4	0.35
Li	[88]	0.99	3.09	6.60	12.78	22.84**	—	—	—
Li	[84]	0.89	3.34	6.80	11.9	20.9	28.0	37.7	50.6
Li	EAM	1.39	2.44	6.03	11.30	23.42	29.27	37.79	61.24
Na	[88]	0.46	1.80	3.74	7.67	14.95	20.28	26.97**	—
Na	[84]	0.55	1.72	4.12	7.45	14.45	20.85	30.31	43.88
Na	EAM	0.66	2.52	3.87	5.22	18.67	37.97	50.64	71.69
K	[88]	0.28	0.97	1.86	3.52	6.91	9.56	13.01	17.38**
K	[84]	0.20	0.61	2.08	3.62	6.40	9.11	13.36	19.80
K	EAM	0.49	1.10	1.81	3.14	6.31	10.59	15.73	19.24
Rb	[88]	—	0.65	1.33	2.39	4.78	6.85	9.68	13.42
Rb	EAM	0.23	0.67	1.61	2.65	5.23	6.78	9.21	14.00
Cs	EAM	0.31	0.69	1.15	1.72	2.68	3.80	5.92	11.53

\* Interpolated data from Ref. [88]. EAM data are calculated at  $T = 10 \text{ K}$  with the use of EAM potentials from Refs [55, 56, 60].

\*\* Extrapolated value.

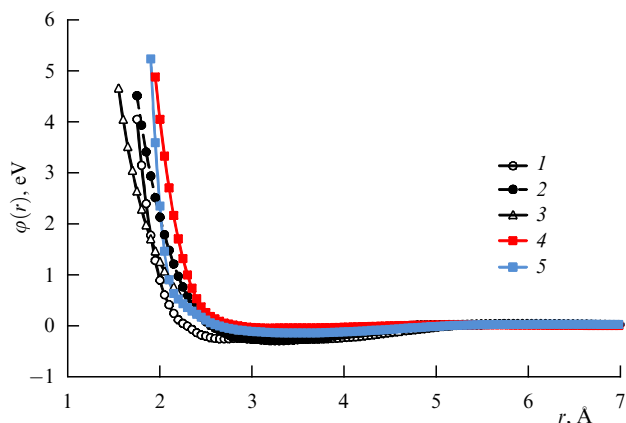


**Figure 10.** Pair contributions  $\phi(r)$  to EAM potentials: 1—Cu [131], 2—Ag [138], 3—Zn [139], 4—Hg [140], and 5—Ga [141].

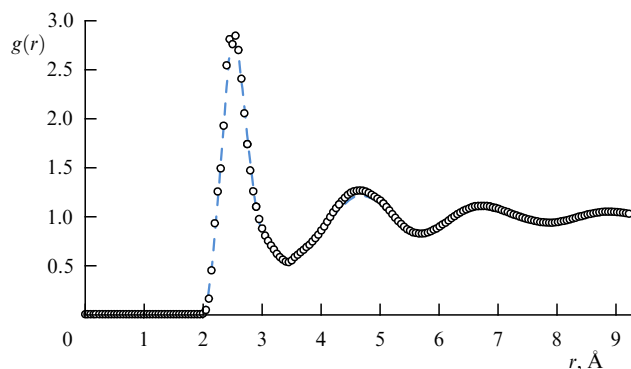


**Figure 12.** Pair correlation function  $g(r)$  of liquid copper at  $T = 1423$  K. Dashed curve—diffraction data [89, 90], and circles—model with EAM potential.

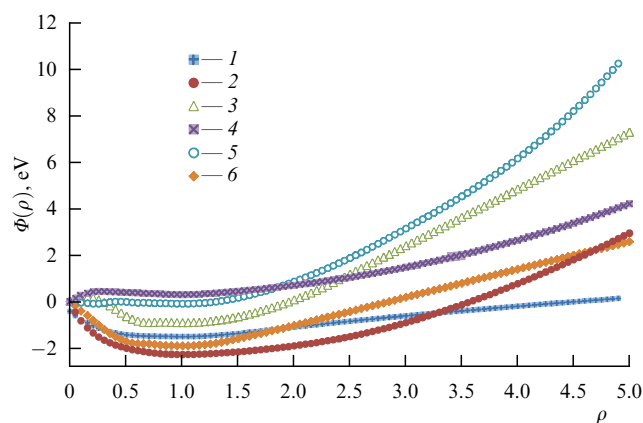


**Figure 11.** Embedding potentials  $\Phi(\rho)$ : 1—Cu [131], 2—Cu [138], 3—Ag [138], 4—Zn [139], 5—Hg [140], and 6—Ga [141].

in simulation to 8.10 Å. At distances smaller than 2.10 Å, the pair contribution was described by an exponential formula. The embedding potential for copper was also borrowed from paper [135] (Fig. 11). The original copper models had an fcc-structure and comprised 2048 particles. The models were constructed for 298–4500 K applying the Verlet algorithm with a time step of  $(0.010\text{--}0.002)t_0$  and internal time unit  $t_0 = 8.116 \times 10^{-14}$  s.

The results of MD simulation of liquid Cu near  $T_m$  are given in Table 2. Model PCFs at 1423–1773 K are consistent with diffraction ones [89, 90] (Table 14). By way of example, Fig. 12 depicts model and diffraction PCFs of copper at  $T = 1423$  K. Model densities near zero pressure also agree with experiment at all temperatures up to  $T = 4500$  K, although they are always slightly lower than those measured by the pulse heating method at high temperatures [142, 143].

The energy of liquid copper models at temperatures below 1873 K is consistent with experiment [142, 143] (see Table 14). At higher temperatures, the model energy is systematically

**Table 14.** Calculated properties of copper and silver\* obtained by the MD method with EAM potential [131].

No.	$T$ , K	$d$ , g cm $^{-3}$		$p$ , GPa, expt.	$\langle \rho \rangle$	$R_g$	$U$ , kJ mol $^{-1}$				$K_T$ , GPa		$D \times 10^5$ , cm $^2$ s $^{-1}$	
		model	expt.				EAM	$E_{eT}$	EAM + $E_{eT}$	expt.	EAM	expt.	EAM	expt.
Copper														
1	298	8.758	8.920	$\sim 0$	1.10	—	−339.96	0	−339.96	−331.2	—	—	—	—
2	1423	7.978	7.978	$\sim 0$	1.00	0.0215	−287.70	0.517	−287.2	−287.8	75 ± 6	69.0	3.58	4.63, 4.70
3	1773	7.686	7.681	$\sim 0$	0.96	0.0328	−275.81	0.837	−275.0	−274.9	—	—	—	—
4	1873	7.611	7.618	$\sim 0$	0.95	0.0671	−272.67	0.943	−271.7	−271.3	65 ± 3	—	7.16	7.29, 10.7
5	3500	6.404	6.437	$\sim 0.3$	0.77	—	−223.64	3.752	−219.9	−218.4	37 ± 8	—	26.1	—
6	4500	5.719	5.854	$\sim 0.3$	0.67	—	−194.03	6.679	−187.4	−191.3	9.3 ± 0.1	—	42.4	—
Silver														
1	298	10.026	10.49	$\sim 0$	1.09	—	−271.08	0	−271.1	−278.70	—	100	—	—
2	1273	9.261	9.261	$\sim 0$	1.00	0.0269	−239.77	0.535	−239.2	−239.69	53.8	53.8	3.45	2.80
3	1423	9.155	9.118	$\sim 0$	0.99	0.0434	−235.53	0.680	−234.8	−233.41	48.54	50.5**	4.68	3.86
4	1673	8.980	8.885	$\sim 0$	0.96	0.0594	−228.56	0.965	−227.6	−225.92	35.91	45.3**	6.47	5.78
5	2000	8.683	8.651	$\sim 10^{-5}$	0.93	—	−218.51	1.423	−217.1	−216.87	23.91	—	8.16	—
6	2400	8.279	8.289	$\sim 10^{-4}$	0.87	—	−207.0	2.128	−204.9	−204.31	17.49	—	11.56	—

\* Data on energy, density [135, 142–144], and diffusion [145–148]. Data for Cu pulse heating were obtained under  $\sim 0.3$  GPa [142, 143]. In Cu simulation, near-ambient pressure was maintained.

\*\* Calculated from the data Ref. [149] on the assumption that  $C_p/C_V = \text{const}$ . Distribution width  $\langle \rho \rangle$  increases from top to bottom of the column from  $\pm 0.03$  to  $\pm 0.10$ .

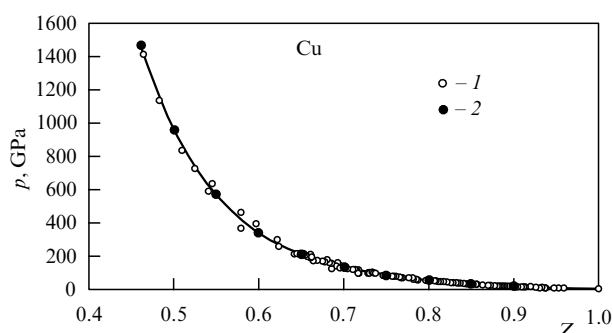


**Figure 13.** Copper shock Hugoniot: 1—experiment [86, 150], and 2—MD calculations [138].

underestimated and a relevant scarcity reaches  $\approx 5.1 \text{ kJ mol}^{-1}$  at  $T = 4000 \text{ K}$ . The discrepancy is eliminated for  $T < 4500 \text{ K}$  by taking into account the contribution from electron thermal energy. Table 14 contains data on bulk compression modulus  $K_T$  and copper self-diffusion coefficient  $D$ .

Each copper fcc-model in Ref. [131] contained 2048 atoms in the basic cube. Calculated near-zero pressure occurred at a density 1.8% lower than the actual one. The energy of crystalline copper models at  $T = 298$  K was by  $\approx 8.7$  kJ mol<sup>-1</sup> lower than the real one. This means that the EAM potential selected based on liquid copper properties is not good enough to describe crystalline Cu (see Table 14).

The shock compression of copper was studied up to a pressure of several thousand GPa. Figure 13 depicts the shock Hugoniot for Cu based on the data from Refs [85, 86, 150–152], which are well approximated by the series expansion

$$p \text{ [GPa]} = -148420.8915Z^5 + 610577.1637Z^4 \\ - 1006240.4673Z^3 + 832344.6559Z^2 \\ - 346818.4603Z + 58547.3376.$$

Here,  $Z = V/V_0$ , where  $V$  is the molar volume in the compressed region,  $V_0$  is the volume under normal conditions, and  $V_0 = 7.115 \text{ cm}^3 \text{ mol}^{-1}$ .

Melting of the copper metal model under shock compression occurred only for  $Z < 0.65$ , when the temperature reached 6000–7000 K. Therefore, it was convenient to use the potential calculated for crystalline copper, when simulating compressed states. In Ref. [138], the shock compression of copper was described using the EAM potential from Ref. [45]. The pair contribution to the potential resembles the function from Ref. [131] (see Fig. 10). The use of this EAM potential yields good results when the degree of compression  $Z = 1.0 - 0.7$ . However, the pressure at the shock Hugoniot is overestimated by several GPa at  $Z = 0.65$  and  $0.60$ , and underestimated by several dozen GPa for  $Z < 0.60$ . For this reason, the embedding potential from Ref. [45] was corrected in Ref. [138] for use in high pressure regions. Correction for the embedding potential from Ref. [45] has the form

$$\Delta\Phi(\rho) = 0.215(\rho - 2.35)^2 H(\rho - 2.35) \text{ [eV]}, \quad (23)$$

with function  $H(x) = 0$  for  $x < 0$ , and  $H(x) = 1$  for  $x \geq 0$ . This correction affects the properties of only those models in which  $\rho > 2.35$ , i.e., for  $Z > 0.60$ . The copper embedding potential with correction (23) included is shown in Fig. 11.

The results of MD calculations of copper properties with this potential under shock compression are presented in Table 15. At 300 K (when correction (23) is insignificant), the agreement with experiment is not very good. In the case of real Cu density, the pressure is 1.82 GPa instead of zero, and the energy is somewhat different from the actual value of  $-331.2 \text{ kJ mol}^{-1}$ . However, the employment of the potential from Ref. [45] with correction (23) leads to overall good agreement of model energy and pressure with the respective

**Table 15.** Properties of copper and silver models at shock compression parameters.

Z	Density, g cm <sup>-3</sup>	$p$ , GPa, expt.	$U_2 - U_1$ , kJ mol <sup>-1</sup>	$T$ , K, model	$\langle \rho \rangle$	$\mu$ , eV	$E_{cT}$ , kJ mol <sup>-1</sup>	$p_{cT}$ , GPa	$E_M$ , kJ mol <sup>-1</sup> , from (16)	$E_{MD}$ , kJ mol <sup>-1</sup>	$p_M$ , GPa, model	$p_M + p_{cT}$ , GPa
1	2	3	4	5	6	7	8	9	10	11	12	13
Copper												
1.00*	8.929	0	0	300	1.00	7.029	0	0	-331.20	-334.10	1.82	1.82
0.90*	9.922	19.22	6.837	300	1.18	7.541	0.00	0	-327.26	-328.4	20.20	20.2
0.80*	11.161	55.88	39.76	600	1.41	8.157	0.058	0.01	-294.40	-297.37	56.49	56.5
0.70*	12.756	137.29	146.53	2590	1.72	8.912	1.31	0.18	-188.88	-189.05	137.3	137.5
0.65*	13.738	212.87	265.05	3920	1.92	8.912	2.880	0.41	-71.93	-72.39	217.3	217.7
0.60	14.883	341.99	486.65	8720	2.15	9.834	13.46	2.11	139.1	138.1	344.8	346.9
0.50	17.86	967.13	1720.3	40,800	2.78	10.098	218.87	41.02	1167.3	1167.2	922.7	963.7
0.46	19.413	1472.9	2829.6	71,100	3.11	8.519	505.68	103.01	1989.8	1989.4	1379	1482
0.46**	19.413	1472.9	2829.6	71,400	3.12	8.490	508.80	103.64	1986.7	1984.5	1345	1449
Silver												
1.00*	10.490	0	0	300	1.00	5.499	0.000	0	-271.08	-271.24	3.42	3.42
0.90*	11.656	17.9	9.22	330	1.36	5.899	0.006	0	-261.87	-262.32	18.03	18.0
0.80*	13.112	44.2	45.49	640	1.62	6.381	0.088	0.01	-225.68	-225.78	44.5	44.5
0.70*	14.986	121.2	186.97	3420	1.79	6.965	2.932	0.27	-87.04	-86.70	120.35	120.7
0.60	17.483	315.8	649.48	11,060	2.48	7.632	27.25	2.94	351.15	351.98	308.64	311.5
0.55	19.073	478.1	1106.2	19,670	2.82	7.880	76.95	9.07	758.17	758.84	468.9	478.0

\* Crystalline states.

\*\* Calculated without correction (23) for the potential from Ref. [45].

experimental findings if electron thermal contributions are taken into account.

Table 15 also lists the results of calculations with the use of the potential from Ref. [45] without correction (23). In this case, the model pressures at  $Z = 0.50$  and  $0.46$  are underestimated compared with experiment by approximately 20 GPa (with good agreement between calculated and experimental energies).

**3.2.2 Silver.** EAM potentials for silver proposed in Refs [35, 53] were applicable to calculations of the liquid structure [35]. In Ref. [138], the pair contribution to the EAM potential was calculated from diffraction data by the Schommers algorithm and approximated by formula (17) with  $k = 4$ ,  $L = 6$ . The cutoff radius of interaction was put to 8.40 Å. This potential is shown in Fig. 10. The embedding potential in the form (5)–(10) was calculated in Ref. [131] taking account of the properties of liquid silver at temperatures of up to 3000 K (see Fig. 11).

Silver models containing 2048 particles were constructed at temperature ranging 298–3000 K by applying the Verlet algorithm. The results are shown in Tables 2 and 8. Good agreement of the liquid structure with experiment was reached even at  $T = 1673$  K ( $R_g = 0.0594$ ). The discrepancy between calculated and experimental energies over the entire temperature range did not exceed  $2 \text{ kJ mol}^{-1}$ , given that corrections for electron thermal energy are considered. The calculated energy of fcc-silver at  $T = 298$  K, similar to that of copper, is much higher than the actual one.

The calculated self-diffusion coefficient is roughly 15–20% higher than the one measured in Ref. [148]. The isothermal bulk compression modulus  $K_T$  is in good agreement with the experimental one at  $T = 1273$  K, but decreases under heating faster than the latter.

The shock Hugoniot for silver calculated from the results of many shock tests under pressures of up to 441 GPa [86, 150] is depicted in Fig. 14. The data presented are well described by the formula

$$p [\text{GPa}] = -11156.739Z^3 + 29309.836Z^2 - 25879.621Z + 7701.890,$$

where  $Z = V/V_0$ , and  $V_0 = 10.283 \text{ cm}^3 \text{ mol}^{-1}$ . The EAM potential was calculated by a method similar to that used to calculate the copper EAM potential, taking into considera-

tion the thermal contribution from collective electrons to energy and pressure. The embedding potential for silver is plotted in Fig. 11.

The results of calculations of silver compressed states are listed in Table 15. In all cases, they agreed well with experimental energy and pressure values along the shock Hugoniot. The mean deviation of theoretical MD-values from experiment was 0.18% for energy, and 0.38% for pressure.

The process of homogeneous crystallization (at zero pressure) in silver models containing 2048 atoms in the basic cube was investigated by the MD method in Ref. [153]. The EAM potential was borrowed from Ref. [53]. The model structure was analyzed checking the local order parameter, structure factor, number of ‘solid-like’ particles (surrounded by local neighbours alike to the fcc-lattice), and energy. Solidification through the cluster mechanism similar to that considered for rubidium in Section 3.1.4 occurred during isothermal MD-runs at temperatures below 802 K. This process was accompanied by a gradual increase in the number of solid-like atoms and the formation and growth of their clusters. In the beginning, the clusters had a very loose structure, and their linear size rapidly reached the size of the basic cube. The process ended in the formation of the fcc-phase. Solid-like atoms played a key role in the solidification process. The lower overcooling limit for silver was found to be near 803 K. The cluster mechanism does not work when this limit is exceeded.

**3.2.3 Gold.** The structure factors and certain thermodynamic properties of liquid gold near the melting point were calculated in Refs [35, 128, 129] with the utilization of EAM potentials. The results were consistent with the diffraction data.

## 4. Metals of group II of the Periodic Table

Up to now, electron thermal contributions to pressure and energy have not been taken into consideration when determining the parameters of EAM potentials for group II metals of the Periodic Table, because the accuracy of formulas (11) and (12) remains unclear.

### 4.1 Magnesium

Liquid magnesium models near the melting point were constructed by the *ab initio* method in Ref. [154]. The structure factor was consistent with experimental data including the asymmetry of the second peak. The dynamics of particle motion were analyzed and transport coefficients calculated.

### 4.2 Zinc

Different variants of the EAM potential for zinc were proposed in Refs [155–159]. The potential derived in paper [139] permits calculating the properties of liquid zinc by the MD method both under standard pressure and in a strongly compressed state. The potential was evaluated based on data on the density, energy, compressibility, and shock compression of liquid zinc. The pair contribution to the potential had the form

$$\varphi(r) [\text{eV}] = g_0 + \frac{g_1}{r} + \frac{g_2}{r^2} + \frac{g_3}{r^3} + \frac{g_4}{r^4},$$

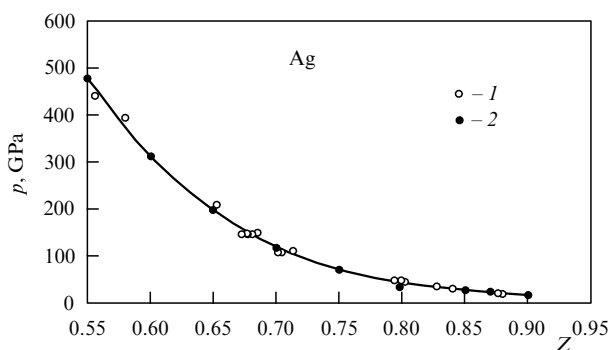


**Figure 14.** Silver shock Hugoniot: 1—experiment [86, 150], and 2—molecular-dynamic data [138].

**Table 16.** Calculated properties of zinc and mercury obtained by the MD method with EAM potential [139, 140]. Density data are taken from Refs [160–162], energy from [160, 163], compressibility from [160, 164], and diffusion from [165].

$T$ , K	$d$ , g cm <sup>−3</sup>		$p$ , GPa	$\langle\rho\rangle$	$R_g$	$-U$ , kJ mol <sup>−1</sup>		$K_T$ , GPa		$D \times 10^5$ , cm <sup>2</sup> s <sup>−1</sup>	
	Model	Expt.				EAM	Expt.	EAM	Expt.	EAM	Expt.
Zinc											
300*	7.140	7.14	−2.69	1.080	—	122.52	124.2	—	70	—	—
723	6.546	6.546	−0.008	1.001	0.029	103.80	103.6	41.5	—	3.39	2.43
933	6.340	6.340	−0.076	0.965	0.042	97.43	97.0	—	—	6.42	—
933	6.362	6.340	0.004	0.975	0.043	97.60	—	35.4	—	6.60	5.84
1200	6.156	—	−0.004	0.935	—	90.35	88.6**	—	—	10.6	11.4
1500	5.949	—	0.008	0.900	—	82.56	79.2**	—	—	14.9	18.3
Mercury											
293	13.55	13.55	1.00	0.009	0.0334	55.28	55.32	25.3	24.9	1.02	1.42–1.72
523	13.04	12.87	0.96	0.010	0.0825	49.17	49.02	19.7	19.0	2.81	—
773	12.38	12.37	0.90	0.021	0.0800	42.52	42.17*	11.13	13.9	4.58	—
1073	11.42	11.42	0.82	−0.026	0.105	34.22	32.79**	6.98	9.34**	7.64	—
1273	10.81	10.82	0.77	0.028	0.0859	28.61	26.9***	5.22	5.51**	10.1	—
1473	10.12	10.13	0.72	0.038	0.0974	22.69	19.8***	—	—	12.3	—
1673	8.63	89.63	0.62	0.159	0.118	14.46	9.4***	—	—	17.7	—
1773	8.26	8.26	0.60	0.285	0.121	12.29	—	—	—	—	—
* At 10 bars.											
** At 500 bars.											
*** With the use of thermal capacity data [166].											

\* At 10 bars.

\*\* At 500 bars.

\*\*\* With the use of thermal capacity data [166].

where distance  $r$  is expressed in angströms. Coefficients have the following values:

$$\begin{aligned}
 g_0 &= 0.72001055937877 \times 10^1, \\
 g_1 &= -0.80150841136324 \times 10^2, \\
 g_2 &= 0.31892147780205 \times 10^3, \\
 g_3 &= -0.57541465681597 \times 10^3, \\
 g_4 &= 0.42163547603305 \times 10^3 \text{ for } 2.15 \leq r < 4.50; \\
 g_0 &= 0.12841892080241 \times 10^2, \\
 g_1 &= -0.30964955609560 \times 10^3, \\
 g_2 &= 0.2736980719079 \times 10^4, \\
 g_3 &= -0.10473860807972 \times 10^5, \\
 g_4 &= 0.14598307517979 \times 10^5 \text{ for } 4.50 < r < 7.62.
 \end{aligned}$$

For  $r < 2.15$ , the pair potential takes the form

$$\begin{aligned}
 \varphi(r) [\text{eV}] &= 0.748224 + 0.63277(2.15 - r) \\
 &+ 0.72 \{ \exp [2.96(2.15 - r)] - 1 \}.
 \end{aligned}$$

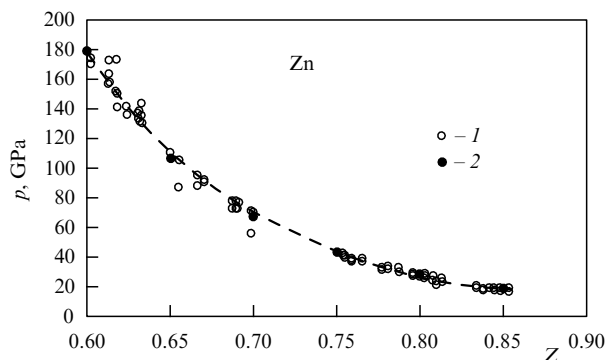
Function  $\varphi(r)$  and its first derivative are continuous at conjugation points. The cutoff radius of the pair potential reaches 7.62 Å. The pair potential for zinc is shown in Fig. 10. The embedding potential in the form (5)–(10) was calculated from the temperature dependence of liquid zinc density (see Fig. 11). It was utilized to determine the properties of liquid zinc at temperatures ranging up to 1500 K (Table 16). The calculated parameters of liquid zinc at  $T \approx T_m$  are listed in Table 2. The bulk compression modulus, self-diffusion coefficient, and PCF agree well with experiment for  $T < 1000$  K. Electron contribution to the energy at these temperatures is small (0.914 kJ mol<sup>-1</sup> at  $T = 1500$  K, assuming the zinc ion charge to be 2). Taking account of this contribution leads to good agreement with experiment for the energy at all temperatures up to 1500 K.

The shock Hugoniot for zinc was obtained by the shock compression technique in Refs [85, 86, 150, 167–172]. At maximum compression achieved in Ref. [170],  $Z = V/V_0 = 0.4474$  and pressure equals 794 GPa. Experimental values at the degree of compression of up to  $Z = 0.6$  and pressure of up to  $\approx 170$  GPa shown in Fig. 15 were approximated by the formula

$$\begin{aligned}
 p [\text{GPa}] &= 4.521984 \times 10^4 Z^4 - 1.387623 \times 10^5 Z^3 \\
 &+ 1.612700 \times 10^5 Z^2 - 8.448182 \times 10^4 Z + 1.692306 \times 10^4
 \end{aligned} \quad (24)$$

with  $V_0 = 9.158 \text{ cm}^3 \text{ mol}^{-1}$ . Figure 11 shows the  $\rho$ -dependence of calculated  $\Phi$ .

Zinc properties in strongly compressed states are listed in Table 17 [139]. Under shock conditions, melting in zinc models occurs for  $Z < 0.7$  and temperatures above 1900 K. For comparison, Table 17 also contains data on electron thermal energy and pressure calculated by formulas (11) and

**Figure 15.** Zinc shock Hugoniot: 1—experiment [85, 86, 150, 167–172], and 2—calculations by MD method [139].

**Table 17.** Properties of zinc and mercury models under shock compression [139, 140].

$Z$	$p$ , GPa, expt.	$U_2 - U_1$ , kJ mol <sup>-1</sup> , from (13)	$T$ , K, model	$T$ , K [57]	$\mu$ , eV	$E_{eT}$ , kJ mol <sup>-1</sup> , from (11)	$p_{eT}$ , GPa	$E_M$ , kJ mol <sup>-1</sup> , from (16)	$E_{MD}$ , kJ mol <sup>-1</sup>	$p_m$ , GPa, model
Zinc										
1.00*	0	0	300	300	9.43	0.000	0.00	-123.14	-123.14	—
0.80*	28.4	26.02	595	730	10.94	0.086	0.01	-97.12	-96.88	28.4
0.70*	67.1	92.13	1855	2260	11.96	0.990	0.10	-31.01	-30.80	67.1
0.65	106.8	171.26	2520	4590	12.56	1.760	0.20	48.12	47.68	107.0
0.60	179.0	327.86	7050	9840	13.233	13.19	1.60	204.72	205.3	176.7
0.55	293.6	604.88	16,020	—	13.93	63.58	8.41	481.74	481.3	293.6
0.50	480.4	1100.3	31,300	—	14.55	217.00	31.58	977.16	905.9	480.7
0.45	773.0	1946.8	52,560	—	14.95	488.38	79.01	1823.66	1497	773.1
Mercury										
1.00*	0	0	298	298	6.85	0	0	-55.28	-55.28	0
0.886	13.4	11.3	725	—	7.42	0.207	0.01	-43.96	-43.51	7.63
0.794	20.62	31.49	1030	—	7.98	0.430	0.03	-23.79	-23.80	20.6
0.779	22.66	37.11	1106	—	8.09	0.495	0.03	-18.17	-18.37	23.5
0.751	32.01	58.98	1702	—	8.28	1.20	0.07	3.70	3.67	31.8
0.721	46.40	95.88	2816	—	8.51	3.25	0.20	40.60	40.69	44.8
0.714	46.45	98.49	2780	—	8.56	3.15	0.20	43.21	43.25	46.6

\* Crystalline state.

(12). For  $Z \geq 0.65$ , the calculated properties are consistent with the experimental ones regardless of electron contributions. However, electron contributions need to be considered at lower  $Z$  values.

### 4.3 Mercury

In the past, interparticle interaction potentials for liquid mercury were calculated by a variety of methods. The Ornstein–Zernike equation with the use of structure-related diffraction data and the pseudopotential technique were tapped for this purpose in Ref. [173]. These two approaches yielded different pair potentials. The authors of Refs [174, 175] demonstrated that a theoretical description of mercury requires explicit consideration of d-electrons and taking account of relativistic effects. The potential obtained in Ref. [174] was used in the MD simulation of mercury.

The effective pair interaction potential for mercury atoms was calculated in Ref. [176] from structural data at temperatures of up to 1823 K using the Ornstein–Zernike equation. Then, an MD simulation modeling of static and dynamic mercury structure was carried out, revealing good agreement between theory and experiment for the speed of sound. The shape of the potentials found showed strong temperature dependence. In Refs [177, 178], the MD models of mercury were constructed applying the potential derived by the molecular orbital method for Hg<sub>2</sub> dimer molecules. Good agreement with diffraction data was achieved only at temperatures of up to 1273 K; the discrepancy considerably increased at higher temperatures. The authors of Ref. [179] applied a simple pair potential in the form of the sum of an exponent and Gaussian potential well, with the parameters selected taking into account the data from Ref. [176]. The correct temperature dependence of the liquid phase density was arrived at in Ref. [179].

MD simulation of liquid mercury in Ref. [180] was performed by the *ab initio* method along the liquid–vapor phase equilibrium curve up to the critical point; simultaneously, the mechanism of metal–nonmetal transition was analyzed. Liquid Hg models contained 50 particles in the

basic cube. With this number of particles, the PCF of the liquid could be calculated only for the first two peaks.

The pair contribution to the EAM potential for mercury was calculated in Ref. [181] from known PCFs applying the Schommers algorithm. The embedding potential was derived in Ref. [163] where Hg models having real density at 293–1803 K were constructed. The theoretical model structure for  $T > 1000$  K was significantly different from the actual one. Nevertheless, both the calculated energy and self-diffusion coefficient were consistent with their experimental values at all temperatures of up to 1673 K.

The EAM potential for Hg was improved and presented in an analytical form in Ref. [140]. The pair contribution was chosen in the form of function (17) with  $k = 5$ ,  $L = 8$  (see Fig. 10). The embedding potential  $\Phi(\rho)$ , i.e., a piecewise continuous function of  $\rho$ , was taken in the form (5)–(10) with the addition of one more  $\rho$ -axis division at  $\rho = \rho_7$ . Coefficients were selected so as to obtain near-normal pressures at all temperatures from 293 to 1673 K and real mercury densities (either at liquid–vapor equilibrium or under specified pressure). The embedding potential is plotted in Fig. 11, and the results of calculations are given in Tables 2 and 14. The density at temperatures of up to 1773 K and the bulk compression modulus (up to 1273 K) were consistent with the respective experimental parameters. The discrepancy among PCFs was rather high ( $\approx 0.08$ ) at all temperatures above 293 K due to the 10–20% difference in the heights of the first peak. The model energy fairly well agreed with experimental values at temperatures of up to 1273 K (discrepancy  $\leq 1.7$  kJ mol<sup>-1</sup>); however, the real energy was much higher than the model one at higher temperatures. The estimates obtained by formulas (11) explain almost half of the discrepancies between real and calculated Hg energies by the electron contribution effect. The main cause of the discrepancies appears to be the metal–nonmetal phase transition initiated by a decrease in density by 25% or more.

To recall, the relationship between the discrepancies of the model and real energy and bulk compression modulus  $K_T$  must exist by virtue of thermodynamic expression

$C_p = C_V + VT\alpha^2 K_T$ , where  $C_p$  and  $C_V$  are heat capacities, and  $\alpha$  is the volume expansion coefficient. Theoretical and actual thermal capacities  $C_V$  at a constant volume are usually similar. Because the model volume expansion coefficient is close to the real one, the underestimation of  $C_p$  inevitably leads to the underestimation of modulus  $K_T$ , as is observed in mercury (see Table 16).

The mercury self-diffusion coefficient at temperatures of up to 1673 K is described by formula  $D = 8.73 \times 10^{-10} T^{1.63963} \text{ [cm}^2 \text{ s}^{-1}\text{]}$ .

References [85–87] report data on the dependence of pressure on the Hg volume along the shock Hugoniot, which were obtained by the shock compression method. In the case of a maximum degree of compression,  $Z = V/V_0 = 0.7138$  (where  $V_0 = 14.815 \text{ cm}^3 \text{ mol}^{-1}$  is the initial volume), the Hg pressure reaches 46.4 GPa. The embedding potential was calculated by the above-described method in Ref. [140] (see Fig. 11). Results of calculations for strongly compressed mercury are presented in Table 17. For the interval of  $0.7138 < Z < 0.7943$ , the discrepancy between the model and real energies does not exceed  $0.2 \text{ kJ mol}^{-1}$ , while for the pressure it is no more than 0.8 GPa. Calculated temperatures at the shock Hugoniot increase with decreasing  $Z$ , but remain below 2900 K. They are not high enough to make the role of electron thermal capacity meaningful.

## 5. Metals of group III of the Periodic Table

The parameters of EAM potentials for group III metals of the Periodic Table were determined taking no account of electron thermal contributions to pressure and energy, because the accuracy of formulas (11) and (12) remains unclear.

### 5.1 Aluminum

Several EAM potentials for aluminum are proposed in the literature. The employment of the pair potential calculated by the pseudopotential method in Ref. [182] overestimated the height of the first PCF peak near the melting point in comparison with the diffraction PCF peak; the melting temperature (1530 K) was overestimated, too. The authors

of Ref. [183] developed the EAM potential for aluminum based on lattice parameters, binding energy, elasticity constants, and vacancy formation energy. Potentials for  $\text{Ni}_3\text{Al}$  were obtained in Ref. [31]. Later on, the short-range and long-range EAM potentials for aluminum were proposed (see Ref. [184] and Ref. [130], respectively). The author of paper [185] proposed a new set of aluminum potentials (for ternary  $\text{Al-Cu-Ag}$  alloys) that give correct values of elastic constants and stacking fault energy but are not accurate enough to calculate surface properties. The EAM potential devised in Ref. [186] permits describing various crystalline phases of aluminum. The same potential was utilized in Ref. [187] to simulate crystallization of overcooled aluminum.

Reference [188] considers the role of temperature in developing different potentials and shows that they do not adequately describe thermal expansion and melting temperature. The known EAM potentials were modified in Ref. [136] in order to improve the agreement between model and diffraction PCFs for liquid aluminum at  $T = 973$  K. Certain data on the liquid aluminum simulation are reported in monograph [5].

The EAM potential for fcc-aluminum proposed in paper [44] was selected based on the data for interparticle forces in the *ab initio* method and various experimental parameters (binding energy, lattice constant, elastic constants, stacking fault energy, etc.). On the whole, the potential is parametrized by 43 parameters. The cutoff radius of all contributions to the potential reached 6.063 Å. This potential ensures good agreement with experiment for aluminum properties at absolute zero. At  $T = 298$  K, the potential from paper [44] leads to an energy error of  $\approx 2\%$  ( $7.0 \text{ kJ mol}^{-1}$ ) (see Table 1). The agreement between theory and experiment for liquid aluminum is much worse (Table 18), and electron thermal contributions are small here. Calculations by formulas (11) with ionic charge 3 yield at 3000 K and zero model pressure the values of electron pressure and thermal energy [ $0.25 \text{ GPa}$  in all and  $4.92 \text{ kJ mol}^{-1}$  (2.1% of the total energy), respectively].

Data on shock compression of aluminum reported in Refs [85–87, 151, 192–195] are presented in Fig. 16. The

**Table 18.** Calculated properties of aluminum and gallium obtained by the MD method with EAM potential.

$T$ , K	Density, g cm <sup>-3</sup>		$\langle \rho \rangle$	$p$ , GPa	$R_g$	$-U$ , kJ mol <sup>-1</sup>		$K_T$ , GPa		$D \times 10^5$ , cm <sup>2</sup> s <sup>-1</sup>	
	EAM	Expt. [143, 189]				EAM	Expt. [143, 190]	EAM	Expt.	EAM	Expt. [191]
Aluminum											
943	2.370	2.370	—	0.44	0.065	−288.63	−297.14	—	—	—	—
1023	2.348	2.348	—	0.48	0.083	−286.09	−294.71	—	—	—	—
1323	2.271	2.328	—	0.48	0.101	−277.15	−285.60	—	—	—	—
2500	2.084	2.077	—	−0.03	—	−246.66	−248.80	—	—	—	—
Gallium											
293	6.103	6.1015	1.000	0.000	0.0176	265.24	265.2	48.3	48.1	1.23	1.56
473	5.976	5.974	0.978	0.000	0.0719	260.31	260.5*	40.3	—	3.10	—
823	5.727	5.720	0.932	0.003	0.0444	251.02	251.4*	28.4	—	7.11	—
1073	5.591	5.604	0.906	−0.001	0.0335	244.85	244.9*	27.8	—	10.7	—
1273	5.491	5.500	0.893	0.001	0.0240	239.97	239.6*	25.0	—	12.9	—
1500	5.387	5.378	0.874	0.000	—	234.64	233.7*	22.7	—	16.8	—
2000	5.094	5.068**	0.818	−0.005	—	222.08	220.7*	16.8	—	22.5	—
3000	4.417	4.448**	0.715	0.006	—	196.70	194.6*	6.70	—	40.4	—
* Calculated in the approximation of constant gallium heat capacity of 26.07 J mol <sup>−1</sup> K <sup>−1</sup> . ** Extrapolated value.											



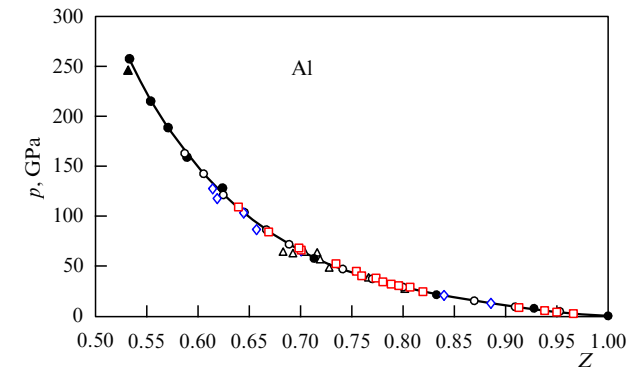


**Figure 16.** Aluminum shock Hugoniot. Light symbols mark experimental data [85–87, 151, 192–195], and dark symbols denote results obtained by the MD method [196].

smoothed dependence of pressure on the degree of compression along the shock Hugoniot for  $0.526 < Z < 1$  has the form

$$p \text{ [GPa]} = -\frac{133.1269}{Z^4} + \frac{902.4080}{Z^3} - \frac{1893.434}{Z^2} + \frac{1702.105}{Z} - 578.1931, \quad (25)$$

where  $Z = V/V_0$ , and  $V_0 = 9.9926 \text{ cm}^3 \text{ mol}^{-1}$  is the normal volume at 300 K.

In Ref. [196], the interatomic potential from Ref. [44] was utilized to calculate aluminum properties under high pressures. The embedding potential  $\Phi(\rho)$  (see Ref. [44]) is a smooth function of effective electron density  $\rho$ ; it equals  $-2.6358$  at  $\rho = 1.20$  and does not change thereafter, i.e.,  $\Phi(\rho) = -2.6358$  as  $\rho \geq 1.20$ . Because calculated model pressures at a high degree of compression were much higher than experimental values, the authors of Ref. [196] introduced a correction into the potential from Ref. [44] in the form of addition valid for  $\rho \geq 1.20$ :  $\Phi(\rho) = -2.6358 + a(\rho - 1.2)^b$ , where  $a = -1.301 \text{ eV}$  and  $b = 2.500$ . These calculations disregarded electron contributions to energy and pressure.

Aluminum models in paper [196] contained 2048 particles in the basic cube. The cutoff radius of all contributions to the potential was put to 6.063 Å. Table 19 lists pressure values along the shock Hugoniot, which were calculated with the use of the corrected EAM potential. Electron corrections for energy and pressure were disregarded, because it was unclear to what extent the free electron model is applicable to group

III–V metals. The correction significantly improved the agreement of model calculations with experiment and resulted in a six-fold reduction in standard deviation of calculated data from experimental ones. Model temperatures along the shock Hugoniot turned out to be lower than those calculated by the standard method [57]. Simulation showed that aluminum remained in the crystalline state at temperatures of up to 6130 K, the degree of compression  $Z = 0.588$ , and pressure 160–165 GPa. Melting occurred at higher temperatures. The consideration of electron corrections in strongly compressed states would be significant (see Table 19).

The properties of aluminum models at temperatures below 10,000 K and the degrees of compression smaller than  $Z = 0.534$  were calculated in Ref. [196], along with melting temperatures (6806 K at 150 GPa, and 7156 K at 200 GPa). The critical parameters of aluminum were determined from the form of a volume dependence of pressure: temperature  $(7050 \pm 20) \text{ K}$ , pressure  $(0.325 \pm 0.020) \text{ GPa}$ , volume  $(40.0 \pm 2.0) \text{ cm}^3 \text{ mol}^{-1}$ , and density  $(0.675 \pm 0.034) \text{ g cm}^{-3}$ .

Simulation by the *ab initio* method was applied to estimate melting temperature [197, 198] and viscosity [199] (64 atoms per cell). At  $T = 1000 \text{ K}$  and density  $2.47 \text{ g cm}^{-3}$  (5% higher than real one), viscosity turned out equal to  $(2.2 \pm 0.1) \text{ mPa s}$ , compared with the actual value of  $1.25 \text{ mPa s}$ . The calculated aluminum melting temperatures reported in Ref. [198] were lower than those in Ref. [196]. For example,  $T_m = 5000 \text{ K}$  at a pressure of 150 GPa [198] instead of  $T_m = 6806 \text{ K}$  with the EAM potential.

**5.2 Gallium**

The pair interaction potential for liquid gallium was first calculated in Ref. [17] from the known PCF by applying the Schommers algorithm. The same algorithm was utilized to generate gallium models in the temperature range 293–1273 K from diffraction data and to reconstruct effective pair potentials (in the form of tables) [200]. The calculated self-diffusion coefficients were consistent with experiment and the Stokes–Einstein equation was fulfilled fairly well. The strong temperature dependence of pair potentials was revealed.

This potential was tapped in Ref. [201] as the pair contribution to the EAM potential for gallium; also, the gallium embedding potential was calculated and gallium models were constructed for 293–5300 K. Good agreement with experiment was achieved for the density and energy (at temperatures of up to 4000 K), structure (PCF), and self-diffusion coefficients (up to 1273 K). The critical temperature

**Table 19.** Properties of aluminum models under shock compression [196].

$Z$	$p$ , GPa, expt.*	$U_2 - U_1$ , kJ mol <sup>−1</sup> , from (13)	$T$ , K, model	$T$ , K [192]	$\mu$ , eV	$E_{eT}$ , kJ mol <sup>−1</sup> , from (11)	$p_{eT}$ , GPa	$E_M$ , kJ mol <sup>−1</sup> , from (16)	$E_{MD}$ , kJ mol <sup>−1</sup>	$p_M$ , GPa, model
1.00**	0	0	298	298	11.66	0	0	−323.8***	−316.84	0
0.833**	21.10	17.66	425	488	13.17	0.036	0.00	−299.18	−299.20	21.86
0.714**	58.41	83.66	1590	1476	14.59	0.089	0.08	−233.18	−233.99	58.48
0.625**	128.79	228.18	4600	4410	15.94	7.00	0.75	−88.66	−87.32	118.5
0.571	189.61	407.85	7850	8180	16.92	19.00	2.24	91.01	93.69	186.7
0.534	258.52	601.44	12,290	—	17.66	44.95	5.61	284.6	260.64	259.5

\* Experimental values smoothed with the use of formula (25).  
\*\* Crystalline state.  
\*\*\* Energy assumed to equal model energy, and electron contributions disregarded.

of gallium was estimated as  $\sim 5000$  K from heat capacity maxima and the dispersion of pressure fluctuations.

The pair contribution to the EAM potential was described by formula (17) with  $k = 5$ ,  $L = 5$  in Ref. [141] (see Fig. 10). Parameters of the embedding potential were selected so as to obtain near-zero values of pressure at all temperatures up to 1500 K. The gallium embedding potential is depicted in Fig. 11.

Liquid gallium models contained 2000 atoms in the basic cube. MD calculations were done using the Verlet integration algorithm. The cutoff radius of interaction was put to 8.30 Å, and MD-runs usually varied from 10,000 to 100,000 time steps (one step lasted  $0.010t_0 - 0.005t_0$ , where  $t_0 = 8.501 \times 10^{-14}$  s is the internal time unit). The results are presented in Table 18. The deviation of the gallium model density from the real one at zero pressure and temperatures  $\leq 1500$  K did not exceed  $\sim 0.2\%$ . Discrepancies  $R_g$  in the temperature range from 293 to 1273 K were insignificant. The model energy is also consistent with actual values, the discrepancy between theoretical and experimental findings at  $T = 2000$  K being only  $1.3 \text{ kJ mol}^{-1}$  [141]. The temperature dependence of the gallium self-diffusion coefficient in the 293–3000 K interval is well described by the expression

$$D \times 10^5 [\text{cm}^2 \text{ s}^{-1}] = -1.679 + 0.009688T \\ + 1.42466 \times 10^{-6} T^2.$$

The electron thermal contribution to pressure and energy of liquid gallium was disregarded in Refs [141, 201]. However, calculations by formulas (11) with ionic charge 3 made relatively small contributions to electron pressure and energy [0.11 GPa and  $2.23 \text{ kJ mol}^{-1}$  (1.0% of the total energy), respectively, at 2000 K, and 0.23 GPa and  $5.61 \text{ kJ mol}^{-1}$  (2.8% of the total value) at 3000 K].

The authors of Ref. [202] proposed the EAM potential for gallium and calculated properties of its crystalline phase, together with the PCF, density, self-diffusion coefficient, and viscosity of the liquid at temperatures of up to 1000 K. Good agreement with experiment was documented for density alone.

### 5.3 Thallium

The authors of Ref. [182] calculated the pair interaction potential for thallium atoms by the pseudopotential method and constructed a liquid model at 577 K. The model structure factor and melting temperature were consistent with experiment.

## 6. Elements of group IV of the Periodic Table

Parameters of EAM potentials for group IV elements of the Periodic Table were determined taking no account of electron thermal contributions to pressure and energy, because the accuracy of formulas (11) and (12) remains unclear.

### 6.1 Carbon

The pressure dependence of liquid carbon structure was studied in Ref. [203] by utilizing the *ab initio* method. A rise in temperature from 5000 to 12000 K at constant density  $2.9 \text{ g cm}^{-3}$  resulted in an increase in pressure from 7.4 to 18 GPa. Elevation of the pressure from 16 GPa (density  $2.9 \text{ g cm}^{-3}$ ) to 2000 GPa (density  $11.6 \text{ g cm}^{-3}$ ) at 9000 K led to a dramatic change in the liquid structure; the first PCF peak grew in height and shifted toward smaller distances, while the

mean coordination number increased from 4 to 8. The form of the structure factor (SF) became similar to that for liquid silicon and germanium under standard pressure.

In order to analyze the carbon structure, it is desirable to estimate the relation  $\rho_1 = r_1(N/V)^{1/3}$ , where  $r_1$  is the coordinate of the first PCF peak. The quantity  $\rho_1$  for dense disordered structures is close to  $1.08 \pm 0.02$  (see the *first topological rule* in book [20]). At a temperature of 9000 K and a density of  $2.9 \text{ g cm}^{-3}$ ,  $\rho_1 = 0.74$  for liquid carbon (as for silica with the structure in the form of a continuous random network). At a density of  $11.6 \text{ g cm}^{-3}$ ,  $\rho_1 = 1.00$ , i.e., the liquid carbon structure remains somewhat loose even at maximum density. The *ab initio* method was also employed to simulate carbon under high pressures in Ref. [204].

### 6.2 Germanium

It is worthwhile to mention *ab initio* calculations of the liquid Ge structure at 1253 K in Ref. [205], where static and dynamic structure factors were found, and the character of the diffusion processes was highlighted.

### 6.3 Tin

Effective pair interaction potentials for tin were calculated in Ref. [206] in the form of tables from available diffraction data using the Born–Green–Bogoliubov equation at 673 and 1973 K. Good results for PCFs and self-diffusion coefficients were obtained, but model pressure differed from zero.

Various diffraction data in the temperature range of 523–1923 K were invoked to develop a liquid tin model with the aid of the Schommers algorithm and reconstruct effective pair interparticle potentials. These potentials are characterized by a steep ascending repulsive part at small interparticle distances and a relatively weak oscillating attractive part at large distances. No regular potential changes with increasing temperature were observed. Calculated self-diffusion coefficients of liquid tin were consistent with experimental values obtained under microgravity. These pair potentials were applied in Ref. [67] to calculate the isotopic effect during self-diffusion ( $^{113}\text{Sn}$  and  $^{125}\text{Sn}$  isotopes).

The use of the Schommers algorithm to treat diffraction data [89, 90] made it possible to achieve an excellent agreement between the model and actual PCFs for tin at  $T = 523$  K, with the discrepancy  $R_g = 0.015$ . Thereafter, the tabulated pair potential data obtained in this way were approximated by formula (17) with  $k = 5$  and  $L = 8$ ;  $r$ -axis division coordinates  $r_i$  were put to 2.65, 3.00, 3.40, 5.45, 7.50, and 8.50 Å. The cutoff radius of interaction reached 8.50 Å. Coefficients  $a_{in}$  are presented in Table 20. For distances  $r < 2.65$  Å, the potential is expressed as

$$\varphi(r) [\text{eV}] = 0.302706 \times 10^{-1} - 6.23244 (2.65 - r) \\ + 3.05 \{ \exp [2.96 (2.65 - r)] - 1 \},$$

where distance  $r$  is taken in angströms. Moreover, addition  $\Delta\varphi(r)$  was introduced into the potential. For all  $r < 8.50$  Å, it is given by

$$\Delta\varphi(r) [\text{eV}] = - \frac{0.0132(r_c - r)^2}{1 + 10(r_c - r)},$$

where  $r_c = 8.50$  Å. The pair contribution to the EAM potential is depicted in Fig. 17. Simulation at 523 K with the interaction potential in the form (17) leads to the discrepancy

**Table 20.** Serial expansion coefficients of the pair contribution to the tin potential.

$a_{im}$	Interval number $i$ /interval boundary $r_i - r_{i+1}$ , Å				
	1 2.65–3.00	2 3.00–3.40	3 3.40–5.45	4 5.45–7.50	5 7.50–8.50
$a_{i0}$	$-0.33106768131256 \times 10^0$	$-0.41096881031990 \times 10^0$	$0.47654975205660 \times 10^{-1}$	$0.22879535332322 \times 10^{-1}$	0
$a_{i1}$	$-0.48710763454437 \times 10^0$	$0.30007066205144 \times 10^{-1}$	$0.14828810095787 \times 10^0$	$-0.28597315773368 \times 10^{-1}$	0
$a_{i2}$	$0.73051608198480 \times 10^1$	$-0.11913647759856 \times 10^1$	$0.37681420549854 \times 10^{-1}$	$0.86736796909025 \times 10^{-1}$	$-0.16480555234605 \times 10^0$
$a_{i3}$	$0.17566696341141 \times 10^3$	$-0.35525441525311 \times 10^2$	$0.92885382042840 \times 10^0$	$0.21374987066953 \times 10^0$	$-0.22990000922706 \times 10^1$
$a_{i4}$	$0.16738880892739 \times 10^4$	$-0.31058274355591 \times 10^3$	$0.20927957423544 \times 10^1$	$0.36381108189423 \times 10^0$	$-0.92156038929245 \times 10^1$
$a_{i5}$	$0.76502392003637 \times 10^4$	$-0.13463118233280 \times 10^4$	$0.23058378948296 \times 10^1$	$0.37353610158349 \times 10^0$	$-0.17672737566504 \times 10^2$
$a_{i6}$	$0.18127859936692 \times 10^5$	$-0.30288034782816 \times 10^4$	$0.13647846975519 \times 10^1$	$0.21467007473032 \times 10^0$	$-0.17783100643326 \times 10^2$
$a_{i7}$	$0.21096194926789 \times 10^5$	$-0.33940974414758 \times 10^4$	$0.41013594462625 \times 10^0$	$0.64954924498744 \times 10^{-1}$	$-0.90586784211199 \times 10^1$
$a_{i8}$	$0.94975016835125 \times 10^4$	$-0.14973915397130 \times 10^4$	$0.49114643645453 \times 10^{-1}$	$0.79890145283860 \times 10^{-2}$	$-0.18440259147500 \times 10^1$

**Table 21.** Calculated properties of tin, lead, and bismuth\* obtained by the MD method with EAM potential at  $p \approx 0$ .

$T$ , K	$d$ , g cm $^{-3}$		$\langle\rho\rangle^{**}$	$p$ , GPa	$R_g$	$-U$ , kJ mol $^{-1}$		$K_T$ , GPa		$D\times 10^5$ , cm $^2$ s $^{-1}$	
	Model	Expt.				EAM	Expt.	EAM	Expt.	EAM	Expt.
Tin											
523	6.93	6.93	1.000	$-0.002$	0.037	288.53	288.56	36.6	36.6	2.09	2.63
573	6.913	6.900–6.958	0.999	$-0.22$	0.044	287.23	287.04	—	—	2.40	—
973	6.767	6.643–6.71	0.977	$\sim 0$	0.076	277.40	274.82	15.3	—	5.34	7.72
1373	6.533	6.468	0.949	$-0.27$	0.054	267.93	262.60	—	—	8.25	10.8
1500	6.454	6.390	0.939	$-0.026$	—	264.79	—	—	—	9.80	—
2000	6.084	6.084	0.907	0.005	—	253.33	—	—	—	11.9	$\sim 14$
3000	5.181	5.471***	0.861	0.005	—	229.44	—	—	—	19.9	—
Lead											
823	10.39	10.39	0.975	$-0.009$	0.036	169.60	169.1	24.1	—	3.91	4.05, 6.01
1023	10.15	10.15	0.956	0.065	0.046	164.28	163.2	17.8	—	5.58	10.2***
1023	10.13	10.15	0.954	$-0.003$	0.047	164.16	163.2	—	—	—	—
1173	9.875	9.875	0.928	$-0.026$	0.035	159.82	158.8	15.0	—	6.92	7.23
2000	8.172	8.172	0.769	0.038	—	135.00	136.0	2.97	—	19.7	19.4
3000	4.969	4.969	0.506	$-0.002$	—	98.44	—	—	—	72.1	51.4
Bismuth											
700	9.880	9.85	0.990	$-0.003$	—	$-178.56$	$-178.1$	—	—	—	—
773	9.785	9.76	0.984	0.002	0.068	$-176.62$	$-175.8$	19.3	—	5.71	3.31
1073	9.396	9.38	0.952	$-0.007$	0.065	$-169.17$	$-166.4$	13.7	—	9.84	11.5
1223	9.207	9.19	0.932	$-0.005$	0.072	$-165.61$	$-161.7$	11.4	—	12.2	—
1500	8.879	8.89	0.910	0.016	—	$-159.45$	$-153.0$	9.29	—	15.3	—
1800	8.513	8.54	0.875	$-0.013$	—	$-152.75$	$-143.6$	—	—	20.0	—
<p>* Density for tin is taken from Refs [89, 290, 209], for lead from [89, 209, 210], for bismuth from [209, 211], for energy from [212, 213], and for diffusion from [191, 214–217].</p> <p>** Standard deviation for each metal increases (from top to bottom of the column) from <math>\sim 0.06</math> to <math>\sim 0.16</math>.</p> <p>*** Extrapolated value.</p>											

$R_g = 0.03–0.04$ . It is relatively small, but the first PCF peak of the model is higher by 0.2–0.3 than the diffraction-assisted PCF peak.

Parameters of the embedding potential were selected so as to obtain the correct values of liquid tin density under near-zero pressure. When the embedding potential is chosen in the form (5)–(10), the optimal potential parameters are as follows:  $p_1 = 4.0244$ ,  $p_2 = 1.2000$  Å $^{-1}$ ,  $\rho_1 = 0.90$ ,  $\rho_2 = 0.78$ ,  $\rho_3 = 0.70$ ,  $\rho_4 = 0.50$ ,  $\rho_5 = 0.28$ ,  $\rho_6 = 1.40$ ,  $a_1 = -1.800$  eV,  $c_1 = 1.1832$ ,  $c_2 = 1.602$  eV,  $c_3 = 1.200$  eV,  $c_4 = 4.000$  eV,  $c_5 = 1.000$  eV, and  $c_6 = 0$ . The remaining parameters are  $a_2 = -1.788168$  eV,  $b_2 = -0.236640$  eV,  $a_3 = -1.736731$  eV,  $b_3 = -0.620640$  eV,  $a_4 = -1.679400$  eV,  $b_4 = -0.812640$  eV,  $a_5 = -1.356872$  eV,  $b_5 = -2.412640$  eV,  $a_6 = -0.777691$  eV, and  $b_6 = -2.852640$  eV. The embedding potential is depicted in Fig. 18.

The properties of a tin model with the EAM potential are listed in Table 21. At all temperatures of up to 3000 K, density values satisfactorily agree with experiment. Discrepancies among PCFs are small only at 523 and 573 K, but increase at higher temperatures. They are largely due to the difference between theoretical and experimental heights of the first PCF peaks (Table 22).

Heating also enhances the difference between calculated and actual energies, which amounts to 5 kJ mol $^{-1}$  at 1373 K. This difference is due to different heat capacities of the models ( $\sim 24$  J mol $^{-1}$  K $^{-1}$ ) and natural tin ( $\approx 34$  J mol $^{-1}$  K $^{-1}$ ). Assuming the tin ion charge to be 4, formula (11) gives an electron thermal energy of 1.339 kJ mol $^{-1}$  and a pressure of 0.05 GPa at  $T = 1373$  K, whereas the appropriate values are 7.47 kJ mol $^{-1}$  and 0.23 GPa at  $T = 3000$  K. This means that taking account of the electron contribution in formula

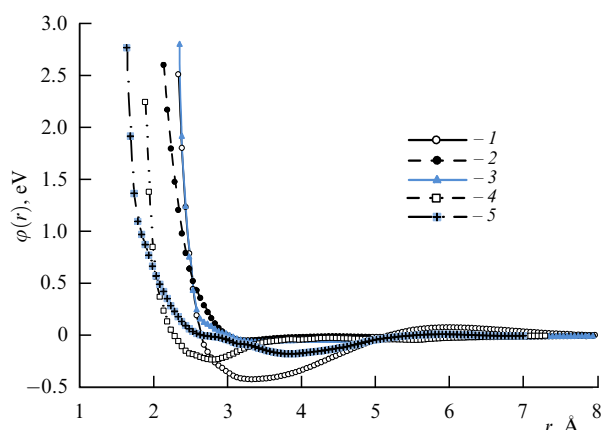


**Figure 17.** Pair contributions  $\phi(r)$  to EAM potentials: 1—Sn, 2—Pb [141], 3—Bi [141], 4—Fe [208], and 5—Ni [208].

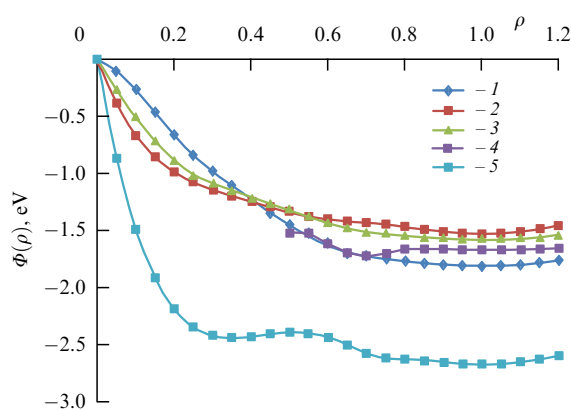


**Figure 18.** Embedding potentials  $\Phi(\rho)$ : 1—Sn, 2—Pb [141], 3—Bi [141], 4—Fe [208], and 5—Ni [208].

**Table 22.** The height of the first PCF peaks in liquid tin.

$T, K$	523	573	973	1173	1973
$g(r_1)$ , diffraction [89, 90]	2.66	2.65	2.08	1.92	—
$g(r_1)$ , diffraction [218]	—	—	—	—	2.05
$g(r_1)$ , model	2.87	2.77	2.32	2.23	2.02

(11) does not eliminate the discrepancy between the results of MD calculations and experiment.

Self-diffusion coefficients of the models presented in Table 21 are described by the formula  $D \times 10^5 = (7.088 \times 10^{-3} T - 1.4948) [\text{cm}^2 \text{s}^{-1}]$ .

A liquid tin model (64 atoms in the basic cell) was constructed by the *ab initio* method at 1873 K in Ref. [219]. The small size of the cell accounts for the underestimation of the tin self-diffusion coefficient at any temperature by a factor of 1.5–2.0 compared with experimental data.

#### 6.4 Lead

The interparticle interaction potential in lead was first calculated in a variant of pairwise interaction [206, 220–222]. In Ref. [206], the pair potential was calculated from the diffraction data (PCF) at 613 and 1023 K, taking into account the Born–Green–Bogoliubov equation. The potentials were considered temperature-dependent. At  $T = 613$  K, the pair

contribution was evaluated [223] using the Schommers algorithm. The authors of Ref. [182] calculated the pair potential for lead by the pseudopotential method and constructed a liquid model at  $T = 650$  K. The model structure factor was consistent with diffraction-based data (although the height of the first peak was overestimated by 0.8), but the melting temperature was overestimated up to 860 K).

The EAM potential for fcc-lead was calculated in Ref. [224] and utilized to simulate liquid lead in Refs [141, 223, 225–229]. The pair contribution to the potential (see Fig. 17) was described by formula (17) with  $k = 3$ ,  $L = 8$  [141]. The embedding potential was chosen in Ref. [141] in the form (5)–(8), and compressed states were not considered. Parameters of the embedding potential were selected with reference to experimental lead density, energy, and bulk compression modulus under standard pressure and temperatures varying from 613 to 1500 K. The resulting dependence  $\Phi(\rho)$  is plotted in Fig. 18. Liquid lead models were constructed in Ref. [141] by the MD method using the EAM potential for 613–3000 K temperature range with the density equal to that of real lead. The models contained 2000 atoms in the basic cube. The cutoff radius of all the contributions to the potential was put to 9.01 Å.

The characteristics of the lead states studied are listed in Table 21. It is evident that model pressure is very low on the atomic scale (pressure unit in the MD method is  $1 \text{ eV } \text{\AA}^{-3} \approx 160 \text{ GPa}$ ). Discrepancies between model and diffraction PCFs are equally small, and the difference between them in terms of shape does not exceed the usual errors of a diffraction experiment. Calculations by formulas (11) at 2000 K give electron thermal corrections of 0.09 GPa and 3.638 kJ mol<sup>−1</sup> for pressure and energy, respectively (the ionic charge being 4). However, the calculated energy is consistent with experiment at all temperatures up to 2000 K without electron correction. The temperature dependence of the self-diffusion coefficient in the 613–3000 K interval is described by the power-like formula  $D = 6.91 \times 10^{-11} T^{1.96495} [\text{cm}^2 \text{s}^{-1}]$ .

The interaction potential inferred in Refs [225–228] fairly well describes the properties of fcc-lead at absolute zero but does not fit equally well to simulate liquid lead. The volume under zero pressure, energy, coordinate and height of the first PCF peak for 600–1173 K are considerably different from the respective experimental data.

The interaction potential from Ref. [224] was used in work [101] to simulate cavitation in liquid lead under negative pressures.

## 7. Elements of group V of the Periodic Table

### 7.1 Phosphorus

Liquid phosphorus models under high pressures were constructed and studied by the *ab initio* method in Refs [204, 230, 231].

### 7.2 Arsenic

Liquid arsenic models under high pressures were constructed and studied by the *ab initio* method in Ref. [204].

### 7.3 Antimony

Antimony is an element from the group of anomalous metals. Liquid antimony models with a density of 6.95 g cm<sup>−3</sup> were

developed using the *ab initio* method in Ref. [232]. Heating from  $T = 1000$  K to  $T = 2000$  K eliminated the small ‘shoulder’ to the right of the first PCF peak. The same method was used to study the antimony structure at temperatures ranging 913–1193 K [233].

#### 7.4 Bismuth

Bismuth is an element from the group of anomalous metals as well. The EAM potential for bismuth calculated in Ref. [234] was utilized to simulate solid Bi–Pb solutions. However, this potential is not sufficiently accurate for liquids [201]. The Bi model constructed for the volume of  $20.835 \text{ cm}^3 \text{ mol}^{-1}$  at  $T = 573$  K brought in the following parameters: pressure  $-1.568$  GPa, and energy  $-142.6 \text{ kJ mol}^{-1}$ . Real pressure was close to zero and energy equaled  $-158.2 \text{ kJ mol}^{-1}$ . The actual volume of the melt at 1223 K was  $22.30 \text{ cm}^3 \text{ mol}^{-1}$  versus  $21.20 \text{ cm}^3 \text{ mol}^{-1}$  obtained by the MD method, thus implying that the EAM potential calculated for a crystal does not fit to adequately describe the liquid phase.

The pair contribution to the interaction potential was found from the known PCFs [89, 90] applying the Schommers algorithm in the form of a numerical table [201]. Parameters of the potential were selected taking account of bismuth’s compressibility and the dependences of density and energy on temperature. Good agreement was achieved between the theoretically predicted and experimental energies at temperatures of up to 1800 K. Movement along the line of constant density of  $7.496 \times 10^{-3}$  atoms per  $\text{\AA}^3$  in a temperature range of 4000–4400 K revealed a heat capacity ( $C_V$ ) peak at  $T \approx 4225$  K, suggesting passage through the critical point. The following critical parameters of bismuth were found:  $T_c = 4225$  K,  $V_c = 80.34 \text{ cm}^3 \text{ mol}^{-1}$  (accordingly, density of  $2.60 \text{ g cm}^{-3}$ ),  $p_c = 0.0076$  GPa, and  $Z_c = p_c V_c / RT_c = 0.0174$ .

The bismuth critical temperature  $T_c = 3780$  K proposed in paper [235] was derived based on the law of corresponding states and sufficiently differs from an above-given value (4225 K). The bismuth critical density was estimated as  $3.07 \text{ g cm}^{-3}$  [235] that also differs noticeably from the relevant result calculated by the EAM method.

The pair contribution to the potential was approximated by formula (17) in Ref. [141]. The cutoff radius of interaction was set to  $9.01 \text{ \AA}$ . The pair contribution to the potential is shown in Fig. 17. The embedding potential was chosen in the form (5)–(8), and only low-pressure states were considered. The parameters of the potential were chosen so as to have near-zero pressure at all temperatures between 573 and 1800 K. The embedding potential is depicted in Fig. 18.

The results of bismuth simulations are listed in Tables 2 and 18. They suggest excellent agreement with experiment on density. At a temperature close to the melting point, the discrepancy  $R_g$  does not exceed 0.0184, but it significantly increases during heating. Similar discrepancies are reported in Ref. [201].

The data in Table 18 indicate that heating causes a faster increase in actual energy than the appropriate simulation procedure, because the heat capacity of natural bismuth ( $\approx 31 \text{ J mol}^{-1} \text{ K}^{-1}$ ) is higher than model thermal capacity ( $\approx 24 \text{ J mol}^{-1} \text{ K}^{-1}$ ), which is usually close to the classical value of  $3R$ . Excess heat capacity of actual bismuth is supposed to be due to the contribution from electron thermal capacity. An estimation using formulas (11) is possible on the formal assumption that each atom accounts for five electrons. At a temperature of 1500 K and bismuth density of

$8.879 \text{ g cm}^{-3}$ , the values of interest are  $E_{eT} = 2.072 \text{ kJ mol}^{-1}$  and  $p_{eT} = 0.06$  GPa. These contributions only partly eliminate the discrepancy with experimental findings.

The temperature dependence of the self-diffusion coefficient in bismuth models is practically linear and can be described by the following expression  $D \times 10^5 = 0.0133T - 4.26 \text{ [cm}^2 \text{ s}^{-1}]$ . The calculated values of the self-diffusion coefficient in the temperature range 573–773 K are much higher than experimental ones [214]. Such a relationship between experiment and MD calculations is rather unusual, because the presence of convection in real measurements results in an overestimation of  $D$ .

## 8. Elements of group VI of the Periodic Table

### 8.1 Selenium

Models of liquid selenium under high pressures were constructed by the *ab initio* method in Refs [236–239].

### 8.2 Tellurium

Models of liquid tellurium under high pressures were constructed by the *ab initio* method in Ref. [204].

## 9. Transition metals

### 9.1 Iron

Pair interaction potentials for iron atoms in the form of a polynomial are proposed in Refs [240, 241]. Their application yielded good results in calculations of iron elastic properties but not energy. The potential from Ref. [240] was used to simulate the structure and thermodynamic properties of iron by the MD method in Refs [242–244]. In Refs [245, 246], the pair potentials in liquid nickel and iron were calculated from the diffraction data using the Percus–Yevick equation.

Later on, the different EAM potentials were proposed for bcc-iron (see, e.g., Refs [31, 247] and liquid iron. In Ref. [248], the EAM potential was chosen in the form resembling the Sutton–Chen potential [249]; its parameters were deduced from quantum-chemical calculations, and the melting curve was plotted for pressures from 60 GPa ( $T = 2500$  K) to 360 GPa ( $T = 7500$  K). A similar EAM potential was utilized in Ref. [250] to calculate the liquid iron structure at pressures of up to 58 GPa and temperatures of up to 2900 K. Iron density proved to be roughly  $1 \text{ g cm}^{-3}$  higher than in the preliminary reference earth model (PREM) [251]. Self-diffusion coefficients at temperatures of up to 7000 K were calculated in the same work [250]. The temperature difference at the outer Earth core was estimated at 2100 K [252]; the authors emphasized the importance of taking account of electron thermal capacity in MD calculations.

Parameters of the EAM potential were selected in Ref. [46] based not only on crystalline iron properties but also on the structural characteristics of the fluid near the melting point. This potential leads to a good agreement between the structure factor and PCFs and the respective experimental values, but a change in the volume during melting is overestimated by a factor of 1.5. The EAM potential from Ref. [46] was tapped in Refs [253, 254] for calculating liquid iron viscosity at temperatures of up to 2000 K and standard pressure with the use of the Green–Kubo relations; reasonable agreement with experimental data was obtained.

**Table 23.** Calculated properties of iron and nickel obtained by the MD method with EAM potential [208, 257, 258]. Density data are from Refs [260, 261], energy from [260], and electron thermal capacity from [262, 263].

No.	$T$ , K	$d$ , g cm <sup>-3</sup>		$\langle\rho\rangle^*$	$R_g$	$U$ , kJ mol <sup>-1</sup> , Expt.	$E_{\text{el}}$ , kJ mol <sup>-1</sup>	$U_{\text{exp}} - E_{\text{el}}$ , kJ mol <sup>-1</sup>	$U$ (EAM), kJ mol <sup>-1</sup>	$U_{\text{exp}} - E_{\text{el}} - U$ , kJ mol <sup>-1</sup>
		EAM	Expt.							
Iron										
1	298	7.742**	7.97	1.116	—	−410.3	0.348	−410.6	−388.41	—
2	1820	6.991**	7.01	0.999	0.0199	−316.5	11.46	−328.0	−327.80	0.0
3	1923	6.933**	6.94	0.991	0.0816	−311.8	12.50	−324.3	−324.50	0.2
4	2023	6.891**	6.86	0.981	0.0814	−307.2	13.52	−320.7	−321.65	0.9
5	2173	6.800**	6.73	0.968	—	−300.4	14.56	−315.0	−316.99	2.0
6	3000	6.124***	6.221	0.849	—	−262.8	24.11	−286.9	−289.55	2.6
7	4000	5.637***	5.572	0.761	—	−217.2	35.86	−253.1	−261.16	8.1
Nickel										
1	298	8.418	8.908	1.060	—	−428.5	0.406	−428.9	−437.07	—
2	1730	7.857	7.867	1.000	0.0264	−359.3	5.992	−365.3	−365.36	0.00
3	1773	7.836	7.840	0.994	0.0215	−357.5	6.124	−363.6	−363.80	0.20
4	1873	7.784	7.775	0.989	0.0359	−353.2	6.424	−359.6	−360.33	0.73
5	2073	7.652	7.646	0.972	—	−344.7	7.785	−352.5	−353.38	0.88
7	2573	7.301	7.324	0.920	—	−323.5	10.987	−334.5	−337.36	2.86
8	3073	6.938	7.002	0.920	—	−302.3	14.688	−317.0	−322.74	5.74
10	4073	6.383	6.358	0.796	—	−259.9	23.606	−283.5	−296.95	13.45
11	4273	6.248	6.230	0.785	—	−251.4	25.546	−276.9	−291.20	14.30
* Dispersion of $\rho$ increases (from top to bottom of the column) from 0.02 to 0.10.										
** Pressure $p = 0$ was maintained in simulation.										
*** Pressure $p = 0.2$ GPa was maintained during simulation.										

The above-mentioned studies were not designed to adequately describe such thermodynamic properties of liquid iron as energy and heat capacity. This issue was considered in Refs [208, 255–257]. In Ref. [255], the pair contribution to the EAM potential was calculated applying the Schommers algorithm (with discrepancy  $R_g = 0.0237$ ). Parameters of the embedding potential were found from data on ion evaporation heat, compressibility, temperature, density, and pressure at the center of Earth (according to PREM) [251]. It was assumed that Earth's center is composed of pure solid iron, but contributions from electron thermal capacity were disregarded. MD calculations demonstrated that iron heating from 1820 to 2500 K causes the model energy to increase more slowly than in natural iron, the difference amounting to 7.8 kJ mol<sup>-1</sup> at  $T = 2500$  K. At a density of 12.5 g cm<sup>-3</sup> and temperature of 5000 K, the model pressure was 360 GPa (in accordance with the PREM data), whereas the interparticle potential from Ref. [46] gave the value of 184 GPa under the same conditions.

The potential developed in Ref. [255] was applied not long after in Refs [258, 259] to calculate the thermodynamic properties of liquid iron and iron–sulfur solutions at high pressures and temperatures. The pair contribution to the EAM potential was approximated by expression (17) with  $k = 4$ ,  $L = 6$ . The cutoff radius of interaction was set to 7.35 Å (the middle of the right slope of the third PCF peak at  $T = 1820$  K). The pair contribution to the potential is displayed in Fig. 17. The embedding potential was chosen in the form (5)–(10) (see Fig. 18).

Liquid iron models with pressure values of 0 or 0.2 GPa at temperatures ranging up to 4000 K were constructed (Table 23). The energies of natural liquid Fe and simulated iron are almost identical at  $T = 1820$  K, and the difference between them reaches 44 kJ mol<sup>-1</sup> at  $T = 4000$  K. This discrepancy was explained by the contribution from electron

thermal energy. In the case of iron, this inference can be verified by taking into account theoretically predicted electron thermal capacity  $C_{el}$  [262, 263]. Integration of heat capacity over temperature gives electron thermal energy  $E_{el}$  equaling 35.9 kJ mol<sup>-1</sup> at  $T = 4000$  K. Then, the difference between predicted and experimental energies reduces to 8.1 kJ mol<sup>-1</sup>. Thus, accounting for electron thermal energy significantly improves the agreement between the results of MD calculations and experimental data, even if it does not completely eliminate the discrepancy. Moreover, an electron thermal pressure of 2.4 GPa at 4000 K and density 5.637 g cm<sup>-3</sup> needs to be taken into account in calculations.

A disadvantage of the potential derived in Refs [255, 258] is that it inadequately describes bcc-iron. For example, it gives a pressure of 3.5 GPa for bcc-iron, 5.5 GPa for fcc-iron, and 3.5 GPa for amorphous iron. In contrast, the EAM potential from Refs [46, 48] fairly well describes the properties of bcc-iron at absolute zero. For this reason, the authors of Ref. [256] simulated iron under the conditions in Earth's core leaned upon potential No. 2 from Ref. [46] corrected so as to adequately describe the iron shock Hugoniot. Electron contributions were disregarded in Ref. [256]. The volume dependence of the pressure along the shock Hugoniot obtained, for example, in Refs [85–87, 150, 167, 169, 170, 264] is described by the following series

$$\begin{aligned}
 p \text{ [GPa]} = & -9.33426249 \times 10^4 Z^5 \\
 & + 3.95863936 \times 10^5 Z^4 - 6.74599715 \times 10^5 Z^3 \\
 & + 5.79152527 \times 10^5 Z^2 - 2.51513311 \times 10^5 Z \\
 & + 4.44392206 \times 10^4,
 \end{aligned}$$

$Z = V/V_0$ , where  $V_0 = 7.0926$  cm<sup>3</sup> mol<sup>-1</sup>. Embedding potential No. 2 in Ref. [46] has the form  $\Phi_1(\rho) = -\rho^{1/2} + D\rho^2$ , where  $D = -3.53871 \times 10^{-4}$ . We supplemented it by the

**Table 24.** Iron ‘cold pressure’.

$Z = V/V_0$	0.9	0.8	0.7	0.6	0.55	0.5	0.45	0.4
$P_{\text{EAM}}, \text{ GPa}$	17.41	44.68	104.4	267.7	352.0	417.6	689	1041
$p_{\text{stand}} [57], \text{ GPa}$	—	42.7	127.5	254.2	365.7	542.2	818	1235

expressions

$$\Phi_1(\rho) = a_7 + b_7(\rho - \rho_6) + c_7(\rho - \rho_6)^m \text{ for } \rho_6 < \rho < \rho_7,$$

$$\Phi_1(\rho) = a_8 + b_8(\rho - \rho_7) + c_8(\rho - \rho_7)^n \text{ for } \rho_7 < \rho, \quad (26)$$

where  $\rho_6 = 38.00$ ,  $\rho_7 = 60.00$ ,  $c_7 = 0.00275 \text{ eV}$ ,  $c_8 = -0.00020 \text{ eV}$ ,  $m = 1.73$ , and  $n = 1.80$ . As a result, good agreement between the model pressure and shock Hugoniot for iron was achieved in Ref. [256]. The average discrepancy between model and experimental data was 1.44 GPa. However, this potential somewhat less adequately describes the properties of liquid iron at  $T = 1820 \text{ K}$  ( $R_g = 0.0442$  instead of 0.0244 for the potential prepared in Ref. [255]).

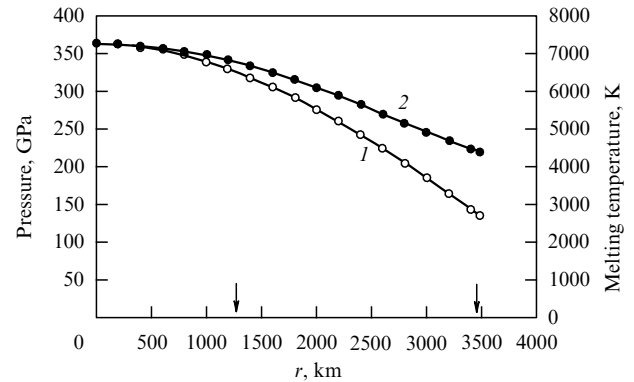
EAM potential [256] permits constructing models of bcc-iron near absolute zero and thereby calculating iron ‘cold pressure’ ( $p_{\text{EAM}}$ ) in order for it to be compared with the results of the standard method ( $p_{\text{stand}}$ ) [57]. This comparison is illustrated in Table 24, showing that the standard method systematically overestimates cold pressure for  $Z < 0.6$ .

According to PREM [251], the density in Earth’s center is around  $13 \text{ g cm}^{-3}$ , with a temperature of 5000–6000 K and pressure of about 360 GPa. Moreover, the inner core is known to be solid, so its temperature is wittingly below the melting temperature. The model constructed with the potential from Ref. [256] at  $T = 5000 \text{ K}$  and a density of  $12.5 \text{ g cm}^{-3}$  had a pressure equal to 251.9 GPa. In Refs [265, 266], the pressure of  $\approx 270 \text{ GPa}$  was obtained by the *ab initio* method at  $T = 5000 \text{ K}$  and a density of  $12.5 \text{ g cm}^{-3}$ ; this value is somewhat higher than our data, meaning that the pressure of pure iron with a density of  $12.5 \text{ g cm}^{-3}$  in Earth’s center would be significantly lower than that predicted by PREM. Were the hypothesis of a purely iron core correct, there would be a marked discrepancy between shock compression results and geophysical data about hypothetical conditions at the center of Earth. The discrepancy between our pressure values and PREM data can be explained by the fact that Earth’s central region is composed of a solution having properties different from those of iron rather than of pure iron.

The iron melting temperature under high pressure was estimated in Ref. [256] by heat-up method for a defective bcc-lattice. Stepwise heating of the bcc-iron model was combined with prolonged isothermal holding under isobaric conditions. The melting temperature values were fixed from an abrupt decrease in the maximum value of the structure factor. The results are presented in Table 25.

**Table 25.** Melting temperature of iron models.

$Z$	1	0.900	0.838	0.800	0.750	0.700	0.659	0.600	0.558	0.550	0.500
$p, \text{ GPa}$	0	31	50	69.5	100	151.5	200	307	400	421	584
$T_m, \text{ K}$	2028	2990	3388	3606	3972	4625	5104	6497	7745	7863	9823

**Figure 19.** The plot of pure iron melting temperature versus distance  $r$  to the Earth’s centre in the hypothetical variant of a purely iron core: 1 — pressure (PREM data [251]), 2 — melting temperature of pure iron [256] depending on the distance to the Earth’s centre. Left arrow shows the boundary between inner and outer cores, and right arrow indicates the core–mantle boundary (PREM).

In this table,  $Z = V/V_0$  stands for reduced iron volume, where  $V$  is the molar volume, and  $V_0 = 7.0926 \text{ cm}^3 \text{ mol}^{-1}$  is the volume at  $T = 298 \text{ K}$ . The value of  $T_m$  is overestimated under standard pressure. At a density of  $12.5 \text{ g cm}^{-3}$ , the results are:  $Z = 0.6298$  and  $T_m \approx 5800 \text{ K}$ . The dependence of  $T_m$  on  $p$  can be approximated by the expression

$$T_m [\text{K}] = -3.553257 \times 10^{-3} p^2 + 1.459459 \times 10^1 p + 2.445713 \times 10^3, \quad (27)$$

where  $p$  is the pressure in GPa. These data agree fairly well with other estimates [248, 267]. For example, the iron melting temperature was 5800 K at  $p = 250 \text{ GPa}$  and 6700 K at  $p = 300 \text{ GPa}$  in Ref. [248], whereas in Ref. [267] the relevant values were as follows: 5500 K at 250 GPa and 6200 K at 300 GPa. The known dependence of pressure on the distance  $R$  to the center of Earth (PREM model) can be used to calculate the  $R$ -dependence of melting temperature in the hypothetical variant of the purely iron core (Fig. 19).

Under Earth’s center conditions ( $p = 364 \text{ GPa}$  [251]), the melting temperature of iron is 7265 K [256]. According to PREM, the density in Earth’s center is  $13.09 \text{ g cm}^{-3}$ . However, if the inner core consisted of pure iron and had the potential as proposed in Ref. [256], its temperature at 364 GPa and a density of  $13.09 \text{ g cm}^{-3}$  would equal 12,430 K (or even 20,500 K at  $12.5 \text{ g cm}^{-3}$ ). Under these conditions, the core cannot be solid. Next, at 4400 K and  $9.903 \text{ g cm}^{-3}$  (PREM, core–mantle boundary), the pressure of liquid iron with the potential of Ref. [256] equals 78.93 GPa (instead of 136 GPa according to PREM). This means that the hypothesis for a purely iron core is in conflict with PREM; hence the conclusion that Earth’s core is composed of an iron-based solution.

The results of iron simulation with EAM potentials are, on the whole, similar to the data obtained by the *ab initio*



**Table 26.** Self-diffusion coefficients of liquid iron models at 6000 K.

Density, g cm <sup>-3</sup>	6.00	7.01	7.79	8.77	9.35	10.02	10.79	11.69
Pressure, GPa	7.19	17.2	50.2	87.0	119.5	165.9	229.0	313.8
$D \times 10^5$ , cm <sup>2</sup> s <sup>-1</sup>	34.8	31.8	19.2	15.6	12.5	10.4	8.20	6.45

method. This method was employed to calculate the properties of both pure iron [198, 265, 268, 269] and iron–sulfur solutions [270, 271]. In the case of pure iron at 6000 K and a density of 13.3 g cm<sup>-3</sup>, its pressure comes to (358 ± 6) GPa and the model exhibits a dense structure with coordination number of 13.8 and self-diffusion coefficient equal to  $(4-5) \times 10^{-5}$  cm<sup>2</sup> s<sup>-1</sup>, i.e., around that typical for liquids under usual pressure. Iron simulation with the potential derived in Ref. [256] at the same temperature and density [with correction (26)] yields a pressure of 329.3 GPa and self-diffusion coefficient of  $6.26 \times 10^{-5}$  cm<sup>2</sup> s<sup>-1</sup>, consistent with the *ab initio* data obtained.

Table 26 presents detailed results on the pressure (density) dependence of the self-diffusion coefficient in iron models with the EAM potential from Ref. [256] and correction (26) at 6000 K.

In the pressure interval from 7.2 to 314 GPa, the self-diffusion coefficient decreases by a factor of 5.4. Values of this coefficient on the order of  $10^{-5}$  cm<sup>2</sup> s<sup>-1</sup> are typical of simple liquids [20] near the melting point. Stokes–Einstein relation (22) is known to be perfectly well fulfilled at high densities. Therefore, iron viscosity must increase within the above interval only by a factor of 5.4.

Usually, the pressure dependence of the self-diffusion coefficient in an activation model is described by the formula  $D = D_0 \exp(-p\Delta V/k_B T)$ , where  $p$  is pressure, and  $\Delta V$  is the activation volume. The  $p$ -dependence of  $\ln D$  is roughly linear with a slope of  $-4.089 \times 10^{-3}$  GPa<sup>-1</sup>, barring the low-pressure region (below 39 GPa). Whence, the value of  $\Delta V = 0.3386$  Å<sup>3</sup> at 6000 K, which accounts for 0.0256 of the atomic volume at a density of 7.14 g cm<sup>-3</sup>, corresponding to the normal melting temperature of iron (1820 K).

Thus, calculations of viscosity in simulation modeling both with EAM potentials and by the *ab initio* method give values for liquid iron viscosity in Earth's core conditions, which are close to those near the melting point under standard pressure. However, estimates [272–274] based on different grounds (with the use of the viscosity activation model and Arrhenius formula or data on the oscillations of Earth's core) amount to viscosities on the order of  $10^{11}$  Pa s at the inner–outer core boundary. Such a value is only possible in crystalline or amorphous phases. In my opinion, the aforementioned independent simulation by two different methods yields more plausible estimates (see also review [275]), because they agree with the results obtained in direct shock compression experiments.

The pure iron melting curve calculated by the *ab initio* method in Ref. [198] under pressures of up to  $\approx 300$  GPa ( $T_m \approx 5700$  K at  $p=250$  GPa and  $T_m \approx 6200$  K at  $p=300$  GPa) is in line with the above estimates. The authors of Ref. [265] used this method to find the Helmholtz energy, changes in volume and entropy during melting, and other properties of iron under the conditions in Earth's core. Also, the iron melting curve was calculated under pressures of up to

350 GPa (6500 K). Consideration of electron thermal capacity reduces this curve by roughly 100 K. The error in calculated melting temperature is estimated as  $\pm 300$  K. In Ref. [198], the shock Hugoniot was constructed separately for solid and liquid iron in agreement with experimental data. The pressures corresponding to the beginning and end of melting along the shock Hugoniot equaled 243 and 298 GPa, respectively. The Grüneisen coefficient in the pressure interval from 280 to 340 GPa was almost constant at 1.51–1.52.

It is worthwhile to compare the results of calculations by different methods. An iron model with the EAM potential [256] at a temperature of 6000 K and density of 13.3 g cm<sup>-3</sup> has a pressure of 329 GPa, i.e., 8% lower than 358 GPa obtained by the *ab initio* method (see above). Furthermore, results obtained with the EAM potential suggest that the melting temperature of iron at 300 GPa is 6500 K [256], whereas the *ab initio* method gives 6200 K [198]. In other words, this last method overestimates the liquid pressure by 8% in comparison with its value in EAM models and, on the contrary, underestimates the melting temperature by 5% (*ab initio* data in Ref. [269] additionally underestimate the iron melting temperature).

According to PREM, the boundary between the inner and outer cores lies 1221.5 km away from the center; the pressure here is  $\sim 329$  GPa. Under this pressure,  $T_m$  of pure iron comes to 6792 K [256] or 6863 K (see interpolation of expression (27) above). In order for the hypothesis of a purely iron solid core to be correct, the temperature closer to the center must run below the plot in Fig. 19 and intersect it with  $R = 1221.5$  km. In the outer core, the temperature must run above the  $T_m$  plot if it is to be liquid. Therefore, the temperature in the inner core may vary within the range of 6792–7265 K and may be close to 7000–7200 K at the center of Earth. At the core–mantle boundary, one finds  $T_m \approx 4401$  K under 136 GPa; therefore, the core temperature in this region must be higher than this value (see Fig. 19) and exceed the melting temperature of pure iron under standard pressure ( $T_m = 1811$  K) by  $\approx 2590$  K. Conversely, mantle matter must be solid under these conditions, as is suggested by the available seismic data (PREM). At such temperatures and standard pressure, the basic oxides of which the mantle is composed would be in the liquid state (e.g.,  $T_m = 2825$  K for pure MgO, and 2570 K for pure CaO, while complex oxides melt at lower temperatures), but their melting points under 136 GPa may be higher than 4400 K.

The main difficulty encountered in calculations of the properties of matter under extreme conditions arises from the indeterminate electron contribution to heat capacity at high temperatures. The method could be improved based on the experimental data about the temperature on shock Hugoniot or by sufficiently precise calculation of an additional contribution to electron thermal capacity and, correspondingly, electron contribution to energy and pressure.

## 9.2 Iron-based solutions. Earth's core

It is generally supposed that Earth's core is composed of a solution of Ni and light elements (Si, S, O, H, C) in iron. A number of solid iron-containing compounds, besides Fe-based solid and liquid solutions, may exist under the conditions formed in Earth's core. Specifically, it is found in Ref. [276], where the properties of various iron carbides and hydrides in the core are calculated, that the most stable among them include Fe<sub>2</sub>C, FeH, FeH<sub>3</sub>, and FeH<sub>4</sub>. However, the calculation of phase diagrams for iron–admixture



**Table 27.** Results of MD calculations [257] in comparison with PREM data.

Level*	R, km, PREM	T, K, MD	S concentration, at. %		Pressure, GPa		Density, g cm <sup>-3</sup>		Speed of sound, km s <sup>-1</sup>	
			MD	PREM	MD	PREM	MD	PREM	MD	PREM
Center	0	6700	5.0	?	364	363.85	13.16	13.088	10.69	11.266
Boundary 1, solid phase	1221.5	6325	5.0	?	329.0	328.85	12.81	12.763	10.35	11.028
Boundary 1, liquid phase	1221.5	6325	11.7	?	329.0	328.85	12.22	12.166	—	10.356
Boundary 2, core	3480	4325 3300?	11 12	? ?	136.0	135.75	9.903	9.903	8.86 8.48	8.065

\* Boundary 1 — inner core–outer core, and boundary 2 — core–mantle.

systems under such extreme conditions is a rather laborious process and very little to date has been done toward this end. It was mentioned in Section 9.1 that Fe–S solutions had been simulated by the *ab initio* method [270, 271].

Reference [257] adopts in the first approximation the two-component variant of the core composition in which iron and sulfur are believed to be the main constituents. The EAM potential for such system was proposed in Ref. [256] and more accurately specified in recent Ref. [257], so as to achieve the best agreement with PREM data on pressure and density at key sites, such as the Earth's center, inner–outer core and outer core–mantle boundaries.

The pair potential for Fe–Fe pairs was taken in Ref. [257] as in Ref. [46], but with correction (26) included. The potentials for Fe–S and S–S pairs were chosen in the form

$$\varphi_{12}(r) = 4\varepsilon_{12} \left[ \left( \frac{\sigma_{12}}{r} \right)^{12} - \left( \frac{\sigma_{12}}{r} \right)^6 \right], \quad \varphi_{22}(r) = \varepsilon_{22} \left( \frac{\sigma_{22}}{r} \right)^6,$$

where  $\sigma_{12} = 2.366 \text{ \AA}$ ,  $\varepsilon_{12} = 0.262 \text{ eV}$ ,  $\sigma_{22} = 2.236 \text{ \AA}$ , and  $\varepsilon_{22} = 1.0767 \text{ eV}$ . The embedding potential for sulfur has the form:

$$\Phi_2(\rho) = \alpha\rho^{1/2} + \beta\rho \quad \text{for } 0 < \rho \leq \rho_3,$$

$$\Phi_2(\rho) = a_3 + b_3(\rho - \rho_3) + c_3(\rho - \rho_3)^p \quad \text{for } \rho_3 < \rho < \rho_4,$$

$$\Phi_2(\rho) = a_4 + b_4(\rho - \rho_4) + c_4(\rho - \rho_4)^q \quad \text{for } \rho_4 < \rho.$$

Function  $\Phi_2$  and its first derivative must be continuous at  $\rho = \rho_3$  and  $\rho = \rho_4$ . The reference point for adjusting the parameters in Ref. [256] was counted upon the conjecture that the temperature and pressure in Earth's center are 5000 K and 360 GPa, respectively, while the concentration of the Fe–S solution is 10 atomic percent (at. %) of sulfur. Moreover, it was assumed that the effective electron density created by sulfur takes the form  $\psi(r) = 89.80 \exp(-1.3860r)$ , where  $r$  is expressed in angströms. In the end, the following values of the parameters were found:  $\alpha = -0.85$ ,  $\beta = 0.2842$ ,  $\rho_3 = 12.00$ ,  $\rho_4 = 40.00$ ,  $c_3 = 0$ ,  $c_4 = -0.002$ , and  $p = q = 1.5$ . A further correction of the EAM potential for sulfur was made in Ref. [257] by varying a single coefficient,  $c_4$ , with the remaining parameters being constant. The EAM potential had a cutoff radius of interaction set to 5.30 Å, as in Ref. [46]. The best agreement with PREM data was achieved with  $c_4 = -0.0505$  and a sulfur concentration in the inner core equaling 5 at. %. The temperature at the boundary between the inner and outer cores was close to 6325 K.

Results of the calculation are presented in Table 27. Evidently, the data of MD calculations and the PREM model are in good agreement at all critical levels of Earth's core. The speed of sound is predicted somewhat less accurately (to within 5–10%). Concentration over the entire inner core is close to 5 at. % and varies by 11–12 at. % in the outer core. Were sulfur distribution by depth in equilibrium, the whole amount of sulfur would accumulate near the core–mantle boundary (by virtue of the interplay between partial molar volumes of Fe and S). However, real localization of sulfur in the inner core suggests nonequilibrium sulfur distribution by depth due to convective melt circulation. The variant shown in Table 27 with temperatures of 6325 and 4325 K at the boundaries is self-consistent, and the said temperature difference can be almost exactly explained by the adiabatic drop. The difference (1920 K) in these temperatures is close to the estimate (2100 K) obtained earlier [252], but the distinction lies in the fact that temperatures at the boundaries of the outer core are calculated in Ref. [272] almost unambiguously.

Reference [257] reports the construction of an Fe–S phase diagram section under a pressure of 329 GPa, corresponding to the boundary between the inner and outer cores. Gibbs energies of solid and liquid phases at the boundary were calculated, and the concentration of the equilibrium liquid phase (10–12 at. % of sulfur) was determined by the common tangent method in accord with the results given in Table 27. Thus, the MD calculations proved self-consistent.

To sum up, the two-component variant of Earth's core makes it possible to obtain good agreement with PREM data. The main results of the calculations performed in Ref. [257] are as follows:

- the pressures in Earth's center, at the inner–outer core boundary and at the core–mantle boundary agree with the PREM data;

- the sulfur concentration is around 5 at. % over the entire inner Earth's core, the temperature in which varies from 6700 K at the center to 6325 K at the boundary with the outer core. The fall in temperature within the inner core equals  $6700 - 6325 = 375 \text{ K}$ ;

- in the outer core, the temperature changes from 6325 K at the boundary with the inner core to 4325–3300 K (depending on the choice of S concentration) at the boundary with the mantle. Sulfur concentration in the outer core weakly depends on the distance to the center. Calculations give its value from 10.7 at. % near the boundary with the inner core to 11–12 at. % on the mantle boundary. Such a small change in concentration suggests effective convective mixing of the melt. Calculation of the adiabatic drop indicates that the

temperature reaches 4325 K, and the sulfur concentration is roughly 11 at.%;

— in the framework of the accepted approximations with respect to core composition, the possible error of the calculated concentration at the key points is rather small ( $\pm 0.5$  at.%)

— the calculated densities at all critical levels are slightly higher than in PREM (by  $0.05 \text{ g cm}^{-3}$  at the most). The discrepancy may be due either to an insufficiently high accuracy of the EAM potential or to the presence of other solution components, besides sulfur;

— the calculated speeds of sound are underestimated by 6–7% in Earth's center and at the inner–outer core boundary compared with the same values in PREM, and overestimated by 5–10% at the boundary with the mantle. The discrepancy may be caused by deviations from the two-component core model;

— the shape of the Fe–S diagram at 329 GPa and 6325 K is in excellent agreement with the above calculations of the composition of the equilibrium liquid phase (11–12 at. % S), but the accuracy of calculations is not high enough for the elucidation of the equilibrium solid phase composition.

Several *ab initio* calculations were done for the Fe–S system. In the case of an S solution in Fe (18.75 at. % S) at 6000 K and  $12.33 \text{ g cm}^{-3}$  (64 particles in the basic cube), the pressure was  $(345 \pm 6) \text{ GPa}$  and the iron self-diffusion coefficient  $D(\text{Fe}) = (4-6) \times 10^{-5} \text{ cm}^2 \text{ s}^{-1}$ ; the sulfur self-diffusion coefficient was of the same value [270]. An estimation based on the Stokes–Einstein relation gives a melt viscosity value of around 13 mPa s, or only 2–3 times higher than the value typical of liquid metals at temperatures close to the melting point ( $\sim 1 \text{ mPa s}$ ). The viscosity of the Fe–S melt found in Ref. [271] under same conditions was roughly 9 mPa s, in good agreement with the Stokes–Einstein relation. Such an order of magnitude for viscosity is obviously at variance with the value found by extrapolation from the low-pressure region ( $10^3 - 10^6 \text{ Pa s}$  in the outer core [271]).

Another object playing an important role in metallurgy is the Fe–C system. Fe–C melts were simulated in Ref. [277] at carbon concentrations of up to 20 at. % and a temperature of up to 2500 K. The EAM potential for Fe–Fe pairs was borrowed from Ref. [225]; the corresponding potentials for Fe–C and C–C pairs were chosen in the form

$$\varphi_{12}(r) = \varepsilon_{12} \left\{ \exp \left[ -2\alpha \left( \frac{r}{r_{12}} - 1 \right) \right] - 2 \exp \left[ -\alpha \left( \frac{r}{r_{12}} - 1 \right) \right] \right\},$$

$$\varphi_{22}(r) = \varepsilon_{22} \left( \frac{r_{22}}{r} \right)^6,$$

where  $\alpha = 4.2$ ,  $\varepsilon_{12} = 0.5450 \text{ eV}$ ,  $r_{12} = 2.23 \text{ Å}$ ,  $\varepsilon_{22} = 1.8767 \text{ eV}$ , and  $r_{22} = 2.236 \text{ Å}$ . Simulation was performed by the MD method. No peculiarities in the behavior of the thermodynamic properties in the temperature range from 1500 to 2500 K were observed. Both the density and molar volume of the melts decreased with increasing carbon concentration at a temperature of 1873 K, while density versus temperature plots undergo an almost parallel shift. Interatomic distances in 1–1 and 1–2 pairs and the sum of coordination numbers of these pairs alter but insignificantly after the addition of carbon. Segregation of C atoms is absent, and the distribution of constituent atoms in the first coordination sphere of Fe–C melts is close to statistical.

In Ref. [278], this system was investigated by the *ab initio* method and subjected to statistical structural analysis. The short-range order in the arrangement of carbon atoms changes with increasing concentration from the statistical one to that reminiscent of their position in cementite ( $\text{Fe}_3\text{C}$ ).

### 9.3 Nickel

The effective pair interaction potential for liquid nickel was calculated from the diffraction data using the Percus–Yevick equation in Ref. [246]. EAM potentials for the description of fcc-nickel properties were proposed in Refs [130, 226, 279, 280]. The pair potential and the embedding potential are presented in the form of the sums of cubic splines. The modified EAM potential for fcc-nickel was proposed in Ref. [39], and for liquid nickel in Ref. [35]. The authors of Ref. [128] used this EAM potential to calculate, with the help of the modified hyperchain equation of the theory of liquids, the structure factors of liquid Ni and some other metals near the melting point. In addition, the structure factors for liquid Ni, Pd, Pt, Cu, Ag, and Au were calculated in Ref. [129] from the results of MD simulation with the EAM potential like those in Refs [33, 34], in good agreement with experimental results. A detailed description of the calculation of the EAM potential for fcc-nickel can be found in Ref. [186]. The EAM potential [249] was tapped in Ref. [281] to simulate nickel nanoclusters on a graphene substrate [282].

The mechanism of crystallization of liquid nickel with the EAM potential from Refs [226, 279, 280] was investigated in Ref. [98]. The structure of crystallizing fluid was judged from the number of atoms with CN = 12. The concentration of such atoms in a stable and metastable fluids increases with decreasing temperature. The equilibrium nickel crystallization temperature under zero pressure comes to 1415 K. The lower overcooling limit for liquid nickel is found, as in the cases of rubidium [72] and silver [153]. The liquid nickel undergoes crystallization via the cluster mechanism under isothermal conditions at temperatures below 850 K under zero pressure and below 1075 K at a constant volume ( $6.588 \text{ cm}^3 \text{ mol}^{-1}$ ) with the predominant formation of a closely packed structure. A crystallization mechanism unlike that adopted in the classical nucleation theory consists in an increase in the number of atoms with CN = 12 in the bulk, the formation of connected groups (12-clusters) from these atoms, and their enlargement, as in rubidium and silver crystallization in response to strong overcooling and admixture coagulation from the oversaturated solution [114–116]. A rise in the number of model nickel atoms with CN = 12 under isothermal simulation run and their clusterization are shown in Fig. 20. Connected groups have an initially loose structure and contain a large number of atoms having different CN, with the maximum group size rapidly tending toward the size of the basic cube. The atoms with CN = 12 play a key role in the crystallization process and activate the transition of atoms included in connected atomic groups of a different coordination into the coordination of the closely packed lattice.

Transit time (during cooling) through the interval from the lower overcooling limit to the temperatures at which diffusion practically stops determines the structure of the resulting solid: either crystalline (when the time is longer than critical) or amorphous (at a shorter time). In the case of Ni, the critical time was  $\approx 7.8 \times 10^{-11} \text{ s}$ , and the critical cooling rate reached  $4.4 \times 10^{12} \text{ K s}^{-1}$ . Indeed, the authors of Ref. [283] did not observe crystallization in the continuous

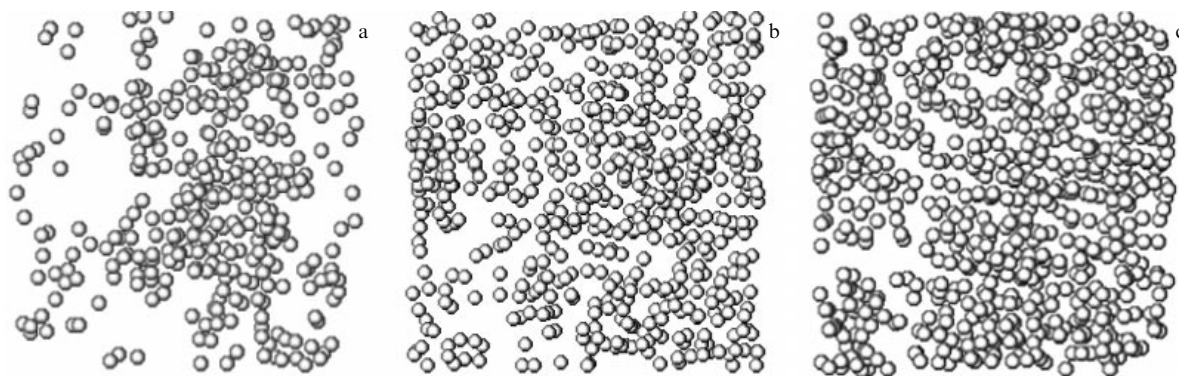


**Figure 20.** (a) Arrangement of atoms with CN = 12 (12-atoms) in a nickel model after rapid cooling from  $T = 2500$  K in the  $p \approx 0$  regime to  $T = 843$  K and relaxation over 48,000 steps. The number of atoms in the model is 2048, cube edge length is 28.886 Å, radius of the nearest-neighbor sphere is 2.95 Å, and number of atoms in the model  $m(12) = 346$ . (b) The same at a step of 54,000, and  $m(12) = 581$ . (c) The same at a step of 60,000, and  $m(12) = 693$ .

cooling regime even at a model cooling rate of  $5 \times 10^{12}$  K s $^{-1}$ .

The pair contribution to the EAM potential was calculated applying the Schommers algorithm from diffraction PCFs at 1773 K and approximated by function (17). The cutoff radius of interaction was put to 7.05 Å (the middle of the right slope of the third PCF peak at  $T = 1773$  K). The pair contribution to the EAM potential for liquid nickel is depicted in Fig. 17. The embedding potential was chosen in the form (5)–(10) (see Fig. 18).

Results of MD calculations for nickel are presented in Table 23. Good agreement with experiment was obtained for the structure (low  $R_g$ ) at temperatures up to 1873 K. The discrepancy between energies at 4000 K amounts to 33 kJ mol $^{-1}$ . A substantial part of this discrepancy is due to the contribution from electron thermal energy. The discrepancy of 14.3 kJ mol $^{-1}$  remaining after subtraction of this electron contribution may be due in part to the some inadequacy of the EAM potential for describing wide temperature intervals.

#### 9.4 Other metals

The EAM potentials have been proposed for many metals, such as Al, Cu, Ag, Au, Ni, Pd, Pt [284], Cu, Ag, Au, Ni [128], Ni, Pd [32], Cu, Ag, Au, Nb, Ta, V [53], V, Nb, Ta, Cr, Mo, W, Fe [31], Nb [285], Zr [286], Cu, Ag, Au, Al, Ni, Pd, Pt [35, 129, 287], Al, Ti [288], Mo [289], Cu, Ag, Au, Al, Ni, Pd, Pt [290], Mo, W, V, Nb, Ta, Fe [40], and other 14 metals with an fcc-lattice [291]. However, not all of them have been utilized to simulate the liquid phase. This list is certainly far from complete. In certain cases, good agreement with experimental data was achieved for melting temperature [287], but it proved impossible to select adequate EAM potentials for crystalline metals with the hexagonal closely packed (HCP) lattice (Cd, Zn, Be, Y, Zr) [292]. Such metals can be adequately described using the not spherically symmetric EAM potential. The liquid structure near the melting point was calculated, for example, in Refs [35, 128, 129, 202]. Much less attention is given to a comparison of the thermodynamic properties with experiment. The same refers to studies relying on the *ab initio* method.

There are relatively few reports on the simulation of liquid uranium. The EAM potential for uranium was selected in Ref. [293] at temperatures up to 6000 K under standard pressure, and at temperatures up to  $\approx 9000$  K (pressure of 360 GPa) under shock compression. Marked discrepancies

between calculated and actual energies of the metal due to electron contribution emerge at temperatures above 1000 K. The electron thermal energy for 5000–6000 K is close to 100 kJ mol $^{-1}$ . The liquid structure above 1500 K is loose and contains voids (pores). The temperature dependence of the self-diffusion coefficient along isobar  $p \sim 0$  is well described by the power-law formula  $D = 5.17 \times 10^{-12} T^{2.1029}$  [cm $^2$  s $^{-1}$ ].

Uranium energy and pressure at temperatures of up to 1200 K and the degrees of compression  $0.55 \leq Z \leq 1$  have been calculated. The EAM potential for solid uranium was developed in Ref. [294], and for the triple U–Mo–Xe system (by the *ab initio* force-matching method) in Ref. [295] (see Section 2.1). The potential is suited to application when simulating both pure components and U–Mo solutions, and also U $_2$ Mo compound.

Calculations somewhat overestimate the melting temperature for uranium (1530 K instead of 1408 K), and underestimate it for molybdenum (2690 K instead of 2890 K).

#### 10. Comparison of results of calculations with different potentials

The properties of liquids depending largely on the short-range repulsive part of the interparticle potential are usually equally well described by pair and EAM potentials. These properties comprise the structure (PCFs, static structure factor), dynamic characteristics (autocorrelation functions, dynamic structure factor, vibrational spectrum, etc.), self-diffusion coefficient, and viscosity. For these properties, many MD calculations with pair potentials yield good results [5, 20, 30, 296]. However, the thermodynamic properties of a metal (first and foremost energy) are sensitive to the shape of the interparticle interaction potential. For this reason, the use of pair potentials does not usually permit obtaining meaningful results. Moreover, EAM potentials suitable for the description of liquid metals are not accurate enough to characterize a crystalline one and vice versa. This makes difficult the achievement of agreement with experiment, e.g., for melting heat, leading instantaneously to discrepancies between theoretical and experimental data on the pressure dependence of melting temperature. This issue awaits detailed investigation. Difficulties encountered in the calculation of surface properties are due to marked changes in density associated with passage across the interface and pose a major challenge to the adequacy of EAM potentials.

The validity of EAM potentials is equally poorly known for broad temperature variations. These potentials for the example of mercury were shown to fairly well describe the temperature dependence of energy over intervals of around 1000 K without consideration of additional effects. In the case of alkali metals, good agreement with experiment can be achieved only by taking account of the thermal energy of collective electrons. However, the cause of discrepancies in the case of group II–V and transition metals remains to be elucidated; as it is, it may be speculated that EAM potentials are inadequate either entirely or in the form they are used.

Of special interest is the simulation of shock compression when temperatures are as high as a few dozen thousand kelvins [297]. In principle, it is possible to select such parameters of EAM potentials [in formulas (9) and (10)] at which good agreement between calculated and experimental pressures and energies on the shock Hugoniot can be achieved both taking account of electron thermal contributions and without them. These two description variants lead to different temperatures on the adiabat and different dependences of cold pressure on metal volume. Further studies along these lines are hampered by the lack of experimental data on shock wave temperature, cold pressure, and X-ray diffraction measurements [298].

## 11. Simulation of binary systems

The simulation of two- and many-component systems requires the modification of the EAM scheme [36]. If pure components possess different average effective electron densities, it is desirable to preliminarily ‘unify’ this parameter,  $\psi(r)$ , so as to equalize the density of both components. In such cases, it is convenient to introduce transformation (3) for each component:

$$\psi_i^*(r) = \lambda_i \psi_i(r), \quad \rho_i^* = \sum_j \psi_j^*(r_{ij}),$$

$$\Phi_i^*(\rho^*) = \Phi_i\left(\frac{\rho^*}{\lambda_i}\right), \quad U = \sum_i \Phi_i^*(\rho^*) + \sum_{i < j} \varphi(r_{ij}),$$

where  $\lambda_i$  is the positive sorting coefficient for the  $i$ th atom. Variations of solution concentration affect only  $\rho^*$  values. For single-component systems, this expression leads to the same energy value as expression (2). Accordingly, formula (4) holds true after the substitutions  $\psi \rightarrow \psi^*$  and  $\Phi \rightarrow \Phi^*$ . In addition, it is necessary to introduce the pair contribution to the EAM potential for those pairs with subscript 12. In the simplest cases, the pair contribution  $\varphi_{12}(r)$  is chosen in the form of the arithmetical mean or geometric mean of  $\varphi_{11}(r)$  and  $\varphi_{22}(r)$  contributions.

The following systems have been simulated with the employment of EAM potentials: Al–Mg [31], Al–Pb [227, 299], Cu–Bi [234], Cu–Pb [134], Cu–Ni [33, 300], Fe–Cr [301], Ni–Nb [302], Pb–Bi and Pb–Ni [226], Ti–Al [287], Fe–C [277], Fe–S [208, 256, 259], Mo–Si [303], Cu–Ni, Cu–Ag, Au–Ni [304], Ni–Al [305], (Ni, Al, Ti, Zr, Fe)–H [306], and some others. A modified EAM scheme was employed for the systems with a large proportion of covalent bonds, taking account of contributions depending on valence angles [36, 42]. The transferability of the EAM potential is realized if the character of the chemical bond does not change with the formation of a solution or a compound.

Certain binary systems have been investigated by the *ab initio* method, e.g., Fe–C [278], Fe–S [270, 271], Li–Na [307].

Special attention was given to alkali metal–group IV and V metal systems. The relevant data are available for Li–Pb [308], Na–Pb [309, 310], K–Pb [311], (Li, Na, K)–Pb [312], K–(Sn, Sb, Te) [313], K–Te [314], and Rb–Te [315, 316] systems, and As<sub>2</sub>S<sub>3</sub> [317, 318] and As<sub>2</sub>Te<sub>3</sub> [319] compounds, and some other melts. Such systems are characterized by electron density transfer from alkali metal atoms to the second constituent. As a result, the type of bonding strongly depends on the composition and may turn into ionic bonding (as in Li<sub>4</sub>Pb and similar melts). In such cases, the adequacy of EAM potentials may prove to be insufficient.

## 12. Conclusions

Of course, the tapping of pair potentials  $\varphi(r)$  in MD simulation provides a wealth of useful information about static and dynamic structures, self-diffusion coefficients and viscosity, autocorrelation functions, etc. These potentials were extensively used in the second half of the 20th century. Interparticle forces in pair interaction models are expressed simply as  $f(r) = -d\varphi(r)/dr$ . Simulation modeling allowed the results of the theory of simple liquids to be verified and significantly promoted its development. However, the pair interaction model yields good results only for a few substances (in fact, for argon alone).

The reason for refusing to utilize pair interaction potentials was the impossibility of simultaneously describing both the structural (static, dynamic) and thermodynamic properties of liquid metals. Transition to many-particle potentials was predetermined. The choice of such potentials in the EAM form should be regarded as successful. When all atoms are in equivalent conditions, the interparticle force has the form  $f(r) = -d\varphi(r)/dr - 2(d\Phi/d\rho)(d\psi/dr)$ . Analysis of computer simulation of liquid metals in the present review indicates that the application of EAM potentials makes it possible to construct sufficiently adequate models by the MD technique, especially in combination with the *ab initio* method, which permits, besides solving specific problems (e.g., calculating electronic structure), yielding additional information needed to find interparticle forces and potentials. It appears reasonably safe to suggest that, for a given combination of parameters (temperature, pressure), the EAM potential for a liquid metal can be parametrized so that the main properties of a large model agree well with experimental findings. However, the question arises as to whether this potential is suitable for constructing good models with other external parameters?

The data reviewed in this publication show that the heat capacity of practically all models increases with temperature more slowly than that of the respective real metal; hence, the discrepancy appears between the energies of model and real metals upon heating by 1000 K, which amounts to a few kJ mol<sup>−1</sup> in the simplest cases, and more than tens of kJ mol<sup>−1</sup> for transition metals. This review shows that such discrepancies are mostly due to the contribution of collective electrons to energy and pressure. For simple liquid metals, e.g., alkali metals, in which these electrons are approximately described by a free-electron model, most discrepancies can be eliminated by using the respective formulas. However, this is sometimes infeasible, and the discrepancy between energies persists even after consideration of electron contributions. It is still unclear whether the discrepancies stem from the choice of an inadequate shape of the EAM potential or from its intrinsic unfitness to work in a wide range of parameters.

**Table 28.** Temperatures at which discrepancies between model and diffraction PCFs emerge.

Metal	Na	K	Cs	Cu	Ag	Hg	Bi
$T_x$ , K	823	723	1673	1873	1573	523	773
$R_g$ at $T_x$	0.071	0.072	0.100	0.067	0.050	0.082	0.068

**Table 29.** Comparison of calculated and actual bulk compression moduli.

Metal	Na	K	Rb	Cs	Ag	Hg
$T$ , K	1500	1500	1000	1373	1800	1273
$K_T^{\text{EAM}}$ , GPa	1.24	0.50	0.88	0.28	32.50	5.22
$K_T^{\text{expt}}$ , GPa	1.40	0.58	0.89	0.35	42.70	5.51

A test for the adequacy of EAM potentials at high temperatures is the degree of agreement between PCFs in liquid metal models and diffraction data. Unfortunately, publications dealing with liquid structure characteristics measured in a wide temperature range (from the melting point to critical values) are scanty. The procedure for the choice of EAM potentials as described in this review ensures small discrepancies  $R_g$  (less than 0.03–0.04) between model PCFs and diffraction data near the melting point. In certain cases, excellent agreement between model and diffraction PCFs was obtained over the entire range of diffraction measurements: for zinc (up to 933 K), lead (up to 1173 K), tin (up to 1373 K), and gallium (up to 1273 K, with the exception of  $T = 473$  K, at which  $R_g = 0.072$ ). In the case of cesium, good agreement was reached at all temperatures below 1673 K (tables of structural data were generously donated by Prof. F Hensel, Marburg). However, discrepancies grow in many cases of metal heating. Temperatures  $T_x$  at which significant discrepancies between two PCFs emerge (the author's EAM-data) are listed in Table 28.

Discrepancies between two PCFs are usually apparent as different heights of the first peak and distortions of the remaining PCF peaks. However, the accuracy of diffraction PCFs is insufficient to explain all discrepancies by potential inadequacy. The case of cesium shows that excellent agreement between model and diffraction PCFs is possible at temperatures up to almost the critical value.

Another test is to verify the accuracy of the calculation of the bulk compression modulus  $K_T$ . By condition, the calculated modulus is very similar to the actual one near the melting point. Table 29 compares calculated,  $K_T^{\text{EAM}}$ , and actual,  $K_T^{\text{expt}}$ , moduli for certain metals at elevated temperatures (the author's EAM-data). The agreement is, on the whole, satisfactory, barring the case of silver. Based on these results, it can be concluded that the EAM potential is, in principle, suitable to describe the properties of liquid metals in a broad temperature range.

The application of EAM potentials looks very promising for describing strongly compressed liquid metals, e.g., under conditions of shock compression. The present review describes methods for the extension of EAM potential applications over the realm of enhanced densities and considers several examples of the calculation of metal properties taking into account the known form of the shock Hugoniot. Simulation of liquid metals by the MD technique permits clarifying information extracted from shock wave data. However, of even greater importance here are electron

contributions that are easy to calculate for simple (but not transition) metals by formulas (11) and (12). Measurement of shock wave temperatures would greatly promote here data analysis. It is certainly possible to select such parameters of EAM potentials at which they would adequately describe the shock Hugoniot without consideration of electron contributions, but this approach leads to the overestimation of temperatures on the adiabat and underestimation of cold pressure.

The search for EAM potentials equally well describing the properties of both liquid and solid phases has not yet brought the desired result. Errors in calculations of melting-related changes in energy and volume are responsible for incorrect values of melting temperatures at high pressure. The needed EAM potentials can be selected both with invoking the *ab initio* data and without them, but this line of research is developing too slowly.

Finally, it is worthwhile to draw attention to certain interesting results of studies on the solidification mechanism, such as the discovery of the lower limit of overcooling for rubidium, nickel, and silver (see Sections 3.1.4, 3.2.2, 9.3). As temperature decreases to below this limit, solidification occurs through the cluster mechanism having nothing in common with classical nucleation. When the cooling rate is too high for nucleation to develop, a liquid reaches the lower overcooling limit and thereby triggers the cluster solidification mechanism. This leads to crystallization, provided diffusion had enough time to ensure structural transformation. Conversely, crystallization fails to occur if the cooling rate exceeds a definite limit, and the process ends in the formation of the amorphous phase.

## References

1. Metropolis N et al. *J. Chem. Phys.* **21** 1087 (1953)
2. Metropolis N, Ulam S *J. Am. Stat. Assoc.* **44** 335 (1949)
3. Alder B J, Wainwright T E *J. Chem. Phys.* **27** 1208 (1957)
4. Lomdahl P S, Germann T C, Kadau K *Bull. Am. Phys. Soc.* **50** 106 (2005)
5. Polukhin V A, Ukhov V F, Dzugutov M M *Komp'yuternoe Modelirovanie Dinamiki i Struktury Zhidkikh Metallov* (Computer Simulation of Dynamics and Structure of Liquid Metals) (Moscow: Nauka, 1981)
6. Gel'chinskii B R, Mirzoev A A, Vorontsov A G *Vychislitel'nye Metody Mikroskopicheskoi Teorii Metallicheskich Rasplavov i Nanoklastrov* (Computational Methods of the Microscopic Theory of Metallic Melts and Nanoclusters) (Moscow: Fizmatlit, 2011)
7. Polukhin V A, Vatolin N A *Modelirovanie Razuporyadochennykh i Nanostrukturirovannykh Faz* (Simulation of Disordered and Nanostructured Phases) (Ekaterinburg: Inst. Metallurgii UrO RAN, 2011)
8. Norman G E, Stegailov V V *Mat. Modelirovanie* **24** (6) 3 (2012)
9. Car R, Parrinello M *Phys. Rev. Lett.* **55** 2471 (1985)
10. Psakhie S G et al. *Crystallogr. Rep.* **54** 1002 (2009) [*Kristallografiya* **54** 1053 (2009)]
11. Norman G E, Starikov S V, Stegailov V V *JETP* **114** 792 (2012) [*Zh. Eksp. Teor. Fiz.* **141** 910 (2012)]
12. Norman G E et al. *Contrib. Plasma Phys.* **53** 129 (2013)
13. Temperley H N V, Rowlinson J S, Rushbrooke G S *Physics of Simple Liquids* (New York: Wiley, 1968) [Translated into Russian (Moscow: Mir, 1973)]
14. Henderson R L *Phys. Lett. A* **49** 197 (1974)
15. Chayes J T, Chayes L J *Stat. Phys.* **36** 471 (1984)
16. Schommers W *Phys. Lett. A* **43** 157 (1973)
17. Schommers W *Phys. Rev. A* **28** 3599 (1983)
18. Reatto L, Levesque D, Weis J J *Phys. Rev. A* **33** 3451 (1986)
19. Evdokimenko O A, Shteinberg A S, Alekhin V P *Metallofizika* **9** 124 (1987)

20. Belashchenko D K *Komp'yuternoe Modelirovanie Zhidkikh i Amorfnykh Veshchestv* (Computer Simulation of Liquid and Amorphous Substances) (Moscow: MISIS, 2005)
21. Belashchenko D K *Russ. J. Phys. Chem.* **75** 387 (2001) [*Zh. Fiz. Khim.* **75** 453 (2001)]
22. Belashchenko D K *Inorg. Mater.* **37** 416 (2001) [*Neorg. Mater.* **37** 501 (2001)]
23. Belashchenko D K, Strykh G F *Inorg. Mater.* **40** 483 (2004) [*Neorg. Mater.* **40** 564 (2004)]
24. Belashchenko D K, Gelchinski B R *J. Non-Cryst. Solids* **353** 3515 (2007)
25. Harrison W A *Pseudopotentials in the Theory of Metals* (New York: W.A. Benjamin, 1966) [Translated into Russian (Moscow: Mir, 1968)]
26. Temperley H N V, Rowlinson J S, Rushbrooke G S *Physics of Simple Liquids* (New York: Wiley, 1968) [Translated into Russian (Moscow: Mir, 1971)]
27. Khar'kov E I, Lysov V I, Fedorov V E *Fizika Zhidkikh Metallov* (Physics of Liquid Metals) (Kiev: Vishcha Shkola, 1979)
28. March N H, Tosi M P *Atomic Dynamics in Liquids* (New York: Wiley, 1976) [Translated into Russian (Moscow: Metallurgiya, 1980)]
29. March N H, Parrinello M *Collective Effects in Solids and Liquids* (Bristol: Hilger, 1982) [Translated into Russian (Moscow: Mir, 1986)]
30. Hansen J P, McDonald I R *Theory of Simple Liquids* (Amsterdam: Elsevier/Academic Press, 2006)
31. Finnis M W, Sinclair J E *Phil. Mag. A* **50** 45 (1984)
32. Daw M S, Baskes M I *Phys. Rev. B* **29** 6443 (1984)
33. Foiles S M *Phys. Rev. B* **32** 7685 (1985)
34. Foiles S M, Baskes M I, Daw M S *Phys. Rev. B* **33** 7983 (1986)
35. Foiles S M *Phys. Rev. B* **32** 3409 (1985)
36. Baskes M I *Phys. Rev. B* **46** 2727 (1992)
37. Daw M S, Foiles S M, Baskes M I *Mater. Sci. Rep.* **9** 251 (1993)
38. Plimpton S J *Comput. Phys.* **117** 1 (1995)
39. Baskes M I *Mater. Chem. Phys.* **50** 152 (1997)
40. Yuan X et al. *J. Phys. Condens. Matter* **15** 8917 (2003)
41. Jelinek B et al. *Phys. Rev. B* **75** 054106 (2007)
42. Dongare A M, Neurock M, Zhigilei L V *Phys. Rev. B* **80** 184106 (2009)
43. Lee B-J et al. *Calphad* **34** 510 (2010)
44. Liu X-Y, Ercolessi F, Adams J B *Modelling Simul. Mater. Sci. Eng.* **12** 665 (2004)
45. Mishin Y et al. *Phys. Rev. B* **63** 224106 (2001)
46. Mendelev M I et al. *Phil. Mag. A* **83** 3977 (2003)
47. [http://potfit.itap.physik.uni-stuttgart.de/wiki/Main\\_Page](http://potfit.itap.physik.uni-stuttgart.de/wiki/Main_Page)
48. Mendelev M I, Srolovitz D J *Phys. Rev. B* **66** 014205 (2002)
49. Stillinger F H, Weber T A *Phys. Rev. B* **31** 5262 (1985)
50. Tersoff J *Phys. Rev. B* **37** 6991 (1988)
51. Katayama Y et al. *Nature* **403** 170 (2000)
52. Hohl D, Jones R O *Phys. Rev. B* **50** 17047 (1994)
53. Doyama M, Kogure Y *Comput. Mater. Sci.* **14** 80 (1999)
54. Belashchenko D K, Smirnova D E *Russ. J. Phys. Chem. A* **85** 1908 (2011) [*Zh. Fiz. Khim.* **85** 2048 (2011)]
55. Belashchenko D K *Inorg. Mater.* **48** 79 (2012) [*Neorg. Mater.* **48** 87 (2012)]
56. Belashchenko D K *High Temp.* **50** 331 (2012) [*Teplofiz. Vys. Temp.* **50** 354 (2012)]
57. Zharkov V N, Kalinin V A *Equations of State for Solids at High Pressures and Temperatures* (New York: Consultants Bureau, 1971) [Translated from Russian: *Uravneniya Sostoyaniya Tverdykh Tel pri Vysokikh Davleniyakh i Temperaturakh* (Moscow: Nauka, 1968)]
58. Landau L D, Lifshitz E M *Statistical Physics* (Oxford: Pergamon Press, 1969) [Translated from Russian: *Statisticheskaya Fizika* (Moscow: GITTL, 1951)]
59. Landau L D, Lifshitz E M *Fluid Mechanics* (London: Pergamon Press, 1959) [Translated from Russian: *Mekhanika Sploshnykh Sred* (Moscow: GITTL, 1953)]
60. Belashchenko D K *High Temp.* **51** 626 (2013) [*Teplofiz. Vys. Temp.* **51** 697 (2013)]
61. Marx D, Hutter J, in *Modern Methods and Algorithms of Quantum Chemistry* (NIC Ser., Vol. 1, Ed. J Grotendorst) (Jülich: John von Neumann Institute for Computing, 2000) p. 301
62. Tuckerman M E *J. Phys. Condens. Matter* **14** R1297 (2002)
63. Kresse G, Furthmüller J *Comput. Mater. Sci.* **6** 15 (1996)
64. Maksimov E G, Lepeshkin S V, Magnitskaya M V *Crystallogr. Rep.* **56** 676 (2011) [*Kristallografiya* **56** 725 (2011)]
65. Lepeshkin S V et al. *JETP* **115** 105 (2012) [*Zh. Eksp. Teor. Fiz.* **142** 115 (2012)]
66. Maksimov E G, Magnitskaya M V, Fortov V E *Phys. Usp.* **48** 761 (2005) [*Usp. Fiz. Nauk* **175** 793 (2002)]
67. Belashchenko D K, Polyanskii R A, Pavlov R N *Russ. J. Phys. Chem.* **76** 454 (2002) [*Zh. Fiz. Khim.* **76** 533 (2002)]
68. Belashchenko D K, Ostrovskii O I *High Temp.* **47** 211 (2009) [*Teplofiz. Vys. Temp.* **74** 231 (2009)]
69. Belashchenko D K *High Temp.* **47** 494 (2009) [*Teplofiz. Vys. Temp.* **47** 522 (2009)]
70. Belashchenko D K *Russ. J. Phys. Chem. A* **83** 260 (2009) [*Zh. Fiz. Khim.* **83** 329 (2009)]
71. Belashchenko D K *Russ. J. Phys. Chem.* **80** 1567 (2006) [*Zh. Fiz. Khim.* **80** 1767 (2006)]
72. Belashchenko D K *Russ. J. Phys. Chem.* **80** 1968 (2006) [*Zh. Fiz. Khim.* **80** 2207 (2006)]
73. Belashchenko D K *High Temp.* **48** 646 (2010) [*Teplofiz. Vys. Temp.* **48** 679 (2010)]
74. Ginzburg A S, Belashchenko D K *Izv. Vyssh. Uchebn. Zaved. Chernaya Metallurg.* (1) 74 (1998)
75. Belashchenko D K, Ginzburg A S *JETP* **88** 28 (1999) [*Zh. Eksp. Teor. Fiz.* **115** 50 (1999)]
76. Mirzoev A A et al. *Metally* (1) 23 (1999)
77. Belashchenko D K, Ginzburg A S, Mendelev M I *Russ. J. Phys. Chem.* **74** 577 (2000) [*Zh. Fiz. Khim.* **74** 669 (2000)]
78. Belashchenko D K, Nikitin N Yu *Russ. J. Phys. Chem. A* **82** 1283 (2008) [*Zh. Fiz. Khim.* **82** 1445 (2008)]
79. Canales M, González L E, Padró J À *Phys. Rev. E* **50** 3656 (1994)
80. Li Y, Blaisten-Barojas E, Papaconstantopoulos D A *Phys. Rev. B* **57** 15519 (1998)
81. Bystrov P I et al. *Liquid-metal Coolants for Heat Pipes and Power Plants* (Ed. V A Kirillin) (New York: Hemisphere Publ. Corp., 1990) [Translated from Russian: *Zhidkometallicheskie Teplonositeli Teplovyykh Trub i Energeticheskikh Ustanovok* (Moscow: Nauka, 1988)]
82. Vaidya S N, Getting I C, Kennedy G C *J. Phys. Chem. Solids* **32** 2545 (1971)
83. Rice M H *J. Phys. Chem. Solids* **26** 483 (1965)
84. Bakanova A A, Dudoladov I P, Trunin R F *Sov. Phys. Solid State* **7** 1307 (1965) [*Fiz. Tverd. Tela* **7** 1615 (1965)]
85. van Thiel M (Ed.) "Compendium of shock wave data", Report UCRL-50108 (Livermore, Calif.: Lawrence Livermore Laboratory, Univ. of California, 1977) p. 323
86. Marsh S P (Ed.) *LASL Shock Hugoniot Data* (Berkeley, Calif.: Univ. of California Press, 1980)
87. Shock wave database, <http://www.ihed.ras.ru/rusbank>
88. Grover R et al *J. Phys. Chem. Solids* **30** 2091 (1969)
89. Waseda Y *The Structure of Non-crystalline Materials: Liquids and Amorphous Solids* (New York: McGraw-Hill, 1980)
90. IAMP database SCM-AXS, <http://res.tagen.tohoku.ac.jp/~waseda/scm/AXS/index.html>
91. Salmon P S et al. *J. Phys. Condens. Matter* **16** 195 (2004)
92. Belashchenko D K *Inorg. Mater.* **47** 654 (2011) [*Neorg. Mater.* **47** 732 (2011)]
93. Animalu O E *Intermediate Quantum Theory of Crystalline Solids* (Englewood Cliffs, N.J.: Prentice-Hall, 1977) [Translated into Russian (Moscow: Mir, 1981)]
94. Information about potassium, <http://chemfiles.narod.ru/element/k/k.html>
95. Metya A K, Hens A, Singh J K *Fluid Phase Equilibria* **313** 16 (2012)
96. Guillaume Ch L et al. *Nature Phys.* **7** 211 (2011)
97. Lepeshkin S V, Magnitskaya M V, Maksimov E G *JETP Lett.* **89** 586 (2009) [*Pis'ma Zh. Eksp. Teor. Fiz.* **89** 688 (2009)]
98. Belashchenko D K, Ostrovskii O I *Russ. J. Phys. Chem. A* **82** 364 (2008) [*Zh. Fiz. Khim.* **82** 443 (2008)]
99. Tonkov E Yu *Fazovyie Diagrammy Elementov pri Vysokom Davlenii* (Phase Diagrams of Elements under High Pressure) (Moscow: Nauka, 1979)
100. Kresse G *J. Non-Cryst. Solids* **192–193** 222 (1995)

101. Bazhironov T T, Norman G E, Stegailov V V *J. Phys. Condens. Matter* **20** 114113 (2008)
102. Polukhin V A, Bratkovskii A M, Vaks V G *Phys. Status Solidi B* **130** 87 (1985)
103. McMahon M I et al. *Proc. Natl. Acad. Sci. USA* **104** 17297 (2007)
104. Lai S K, Li W, Tosi M P *Phys. Rev. A* **42** 7289 (1990)
105. Shimkevich A L, Shimkevich I Yu, Preprint FEI-2830 (Obninsk: Institute for Physics and Power Engineering, 2000)
106. Anderson M S, Swenson C A *Phys. Rev. B* **28** 5395 (1983)
107. Winzenick M, Vijayakumar V, Holzapfel W B *Phys. Rev. B* **50** 12381 (1994)
108. Munejiri Sh et al. *J. Non-Cryst. Solids* **205–207** 278 (1996)
109. Munejiri Sh, Shimojo F, Hoshino K *J. Phys. Condens. Matter* **12** 4313 (2000)
110. Hosokawa S et al. *J. Non-Cryst. Solids* **250–252** 159 (1999)
111. Bundy F P *Phys. Rev.* **115** 274 (1959)
112. Belashchenko D K *Int. J. Thermophys.* **29** 2169 (2008)
113. Hsu C S, Rahman A J. *Chem. Phys.* **70** 5234 (1979)
114. Lobanov E S, Belashchenko D K *Inorg. Mater.* **42** 622 (2006) [*Neorg. Mater.* **42** 689 (2006)]
115. Belashchenko D K, Lobanov E S, Syrykh G F *Russ. J. Phys. Chem.* **79** (Suppl. 1) S135 (2005)
116. Belashchenko D K, Lobanov E S, Syrykh G F *J. Alloys Compounds* **434–435** 577 (2007)
117. Zempo Y et al. *Comput. Mater. Sci.* **14** 19 (1999)
118. Shimojo F et al. *J. Non-Cryst. Solids* **353** 3492 (2007)
119. Mirzoev A A et al. *J. Phys. Condens. Matter* **20** 114104 (2008)
120. Belashchenko D K, Nikitin N Yu *J. Phys. Conf. Ser.* **98** 042020 (2008)
121. Winter R et al. *Ber. Bunsenges. Phys. Chem.* **91** 1327 (1987)
122. Falconi S et al. *Phys. Rev. Lett.* **94** 125507 (2005)
123. Kennedy G C, Jayaraman A, Newton R C *Phys. Rev.* **126** 1363 (1962)
124. Gómez S et al. *J. Non-Cryst. Solids* **250–252** 163 (1999)
125. Gelchinski B R et al. *J. Non-Cryst. Solids* **353** 3480 (2007)
126. Katayama Y, Tsuji K *J. Phys. Condens. Matter* **15** 6085 (2003)
127. Belashchenko D K *Phys. Usp.* **42** 297 (1999) [*Usp. Fiz. Nauk* **169** 361 (1999)]
128. Bhuiyan G M et al. *J. Non-Cryst. Solids* **250–252** 45 (1999)
129. Alemany M M G et al. *J. Non-Cryst. Solids* **250–252** 53 (1999)
130. Cai J, Ye Y Y *Phys. Rev. B* **54** 8398 (1996)
131. Belashchenko D K *Inorg. Mater.* **48** 940 (2012) [*Neorg. Mater.* **48** 1062 (2012)]
132. Lutsko J F et al. *Phys. Rev. B* **40** 2841 (1989)
133. Valkealahti S, Manninen M *J. Phys. Condens. Matter* **9** 4041 (1997)
134. Hoyt J J et al. *Modelling Simul. Mater. Sci. Eng.* **11** 287 (2003)
135. Belashchenko D K, Zhuravlev Yu V *Inorg. Mater.* **44** 939 (2008) [*Neorg. Mater.* **44** 1058 (2008)]
136. Mendelev M I et al. *Phil. Mag.* **88** 1723 (2008)
137. Vorontsov A G, Mirzoev A A *Vestn. Yuzhno-Ural'skogo Univ. Ser. Mat. Mekh. Fiz.* (9) 68 (2007)
138. Belashchenko D K *Inorg. Mater.* **49** 450 (2013) [*Neorg. Mater.* **49** 473 (2013)]
139. Belashchenko D K *High Temp.* **50** 61 (2012) [*Teplofiz. Vys. Temp.* **50** 65 (2012)]
140. Belashchenko D K *High Temp.* **51** 40 (2013) [*Teplofiz. Vys. Temp.* **51** 47 (2013)]
141. Belashchenko D K *Russ. J. Phys. Chem. A* **86** 779 (2012) [*Zh. Fiz. Khim.* **86** 872 (2012)]
142. Gathers G R *Rep. Prog. Phys.* **49** 341 (1986)
143. Gathers G R *Int. J. Thermophys.* **4** 209 (1983)
144. Kirshenbaum A D, Cahill J A, Grosse A V *J. Inorg. Nucl. Chem.* **24** 333 (1962)
145. Henderson J, Yang L *Trans. Met. Soc. AIME* **221** 72 (1961)
146. Iida T, Guthrie R I L *The Physical Properties of Liquid Metals* (Oxford: Clarendon Press, 1988)
147. Geysermans P, Mareschal M, Pontikis V *Mol. Phys.* **95** 465 (1998)
148. Leak V, Swalin R A *Trans. Met. Soc. AIME* **230** 426 (1964)
149. Filippov S I, Kazakov N B, Pronin L A *Izv. Vyssh. Uchebn. Zaved. Chernaya Metallurg.* (3) 8 (1966)
150. Al'tshuler L V et al. *J. Appl. Mech. Tech. Phys.* **22** 145 (1981) [*Zh. Priklad. Mekh. Tekh. Fiz.* (2) 3 (1981)]
151. Glushak B L et al. *Sov. Phys. JETP* **69** 739 (1989) [*Zh. Eksp. Teor. Fiz.* **96** 1301 (1989)]
152. Trunin R F et al., in *Eksperimental'nye Dannye po Udarnovolnovomu Szhatiyyu i Adiabaticeskomu Rasshireniyu Kondensirovannykh Veshchestv* (Experimental Data on Shock-wave Compression and Adiabatic Extension of Condensed Matter) (Ed. R F Trunin) (Sarov: RFYaTs-VNIIEF, 2001)
153. Belashchenko D K, Lobanov E S *AIP Conf. Proc.* **999** 202 (2008)
154. Sengül S, González D J, González L E *J. Phys. Condens. Matter* **21** 115106 (2009)
155. Ramprasad R, Hoagland R G *Modelling Simul. Mater. Sci. Eng.* **1** 189 (1993)
156. Braisaz T et al. *Phys. Status Solidi B* **191** 267 (1995)
157. Römer F, Kraska T *J. Chem. Phys.* **127** 234509 (2007)
158. Moitra A et al. *Bull. Am. Phys. Soc.* **53** (2) Q20.008 (2008)
159. Römer F, Braun S, Kraska T *Phys. Chem. Chem. Phys.* **11** 4039 (2009)
160. Vukalovich M P et al. *Teplofizicheskie Svoystva Rtuti* (Thermophysical Properties of Mercury) (Moscow: Izd. Standartov, 1971)
161. Hensel F *MRS Proc.* **22** 3 (1984)
162. Tamura K, Hosokawa Sh *Phys. Rev. B* **58** 9030 (1998)
163. Belashchenko D K *High Temp.* **44** 675 (2006) [*Teplofiz. Vys. Temp.* **44** 682 (2006)]
164. Kozhevnikov V et al. *J. Non-Cryst. Solids* **205–207** 256 (1996)
165. Hoffman R E *J. Chem. Phys.* **20** 1567 (1952)
166. Levin M, Schmutzler R W *J. Non-Cryst. Solids* **61–62** 83 (1984)
167. Walsh J M et al. *Phys. Rev.* **108** 196 (1957)
168. Al'tshuler L V, Krupnikov K K, Brazhnik M I *Sov. Phys. JETP* **7** 614 (1958) [*Zh. Eksp. Teor. Fiz.* **34** 886 (1958)]
169. McQueen R G, Marsh S P *J. Appl. Phys.* **31** 1253 (1960)
170. Al'tshuler L V, Bakanova A A, Trunin R F *Sov. Phys. JETP* **15** 65 (1962) [*Zh. Eksp. Teor. Fiz.* **42** 91 (1962)]
171. Volkov K V, Sibilev V A *Zh. Priklad. Mekh. Tekh. Fiz.* (4) 125 (1984)
172. Trunin R F, Simakov G V *Mat. Model.* **5** (8) 108 (1993)
173. McLaughlin I L et al. *Z. Phys. Chem. Neue Folge* **156** 457 (1988)
174. Jank W, Hafner J *Phys. Rev. B* **42** 6926 (1990)
175. Moriarty J A *Phys. Lett. A* **131** 41 (1988)
176. Munejiri Sh, Shimojo F, Hoshino K *J. Phys. Condens. Matter* **10** 4963 (1998)
177. Sumi T et al. *Phys. Rev. B* **57** 914 (1998)
178. Sumi T, Miyoshi E, Tanaka K *Phys. Rev. B* **59** 6153 (1999)
179. Bomont J-M, Delhommelle J, Bretonnet J-L *J. Non-Cryst. Solids* **353** 3454 (2007)
180. Kresse G, Hafner J *Phys. Rev. B* **55** 7539 (1997)
181. Belashchenko D K *High Temp.* **40** 212 (2002) [*Teplofiz. Vys. Temp.* **40** 240 (2002)]
182. El Mendoub E B et al. *J. Non-Cryst. Solids* **353** 3475 (2007)
183. Voter A F, Chen S P *MRS Symp. Proc.* **82** 175 (1987)
184. Oh D J, Johnson R A *J. Mater. Res.* **3** 471 (1988)
185. Rohrer C L *Modelling Simul. Mater. Sci. Eng.* **2** 119 (1994)
186. Mishin Y et al. *Phys. Rev. B* **59** 3393 (1999)
187. Morozov I V et al. *Comput. Phys. Commun.* **182** 1974 (2011)
188. Ercolessi F, Adams J B *Europhys. Lett.* **26** 583 (1994)
189. Arsent'ev P P, Koledov L A *Metallicheskie Rasplavy i Ikh Svoystva* (Metallic Melts and Their Properties) (Moscow: Metallurgiya, 1976)
190. Veryatin U D et al. *Termodinamicheskie Svoystva Neorganicheskikh Veshchestv* (Thermodynamic Properties of Inorganic Matter) (Ed. A P Zefirov) (Moscow: Atomizdat, 1965)
191. Belashchenko D K *Yavleniya Perenosa v Zhidkikh Metallakh i Poluprovodnikakh* (Transfer Phenomena in Liquid Metals and Semiconductors) (Moscow: Atomizdat, 1973)
192. Al'tshuler L V et al. *Sov. Phys. JETP* **11** 573 (1960) [*Zh. Eksp. Teor. Fiz.* **38** 790 (1960)]
193. McQueen R G et al. "The equation of state of solids from shock wave studies", in *High-Velocity Impact Phenomena* (Ed. R Kinslow) (New York: Academic Press, 1970)
194. Knudson M D et al. *J. Appl. Phys.* **94** 4420 (2003)
195. Mitchell A C, Nellis W J *J. Appl. Phys.* **52** 3363 (1981)
196. Belashchenko D K, Vorotyagin A V, Gelchinsky B R *High Temp.* **49** 656 (2011) [*Teplofiz. Vys. Temp.* **49** 676 (2011)]
197. de Wijs G A, Kresse G, Gillan M J *Phys. Rev. B* **57** 8223 (1998)
198. Alfè D et al. *J. Phys. Condens. Matter* **16** S973 (2004)



199. Stadler R et al. *J. Non-Cryst. Solids* **250–252** 82 (1999)
200. Belashchenko D K, Ginzburg A S *Russ. J. Phys. Chem.* **75** 790 (2001) [*Zh. Fiz. Khim.* **75** 885 (2001)]
201. Belashchenko D K, Ostrovskii O I *Russ. J. Phys. Chem.* **80** 509 (2006) [*Zh. Fiz. Khim.* **80** 602 (2006)]
202. Baskes M I, Chen S P, Cherne F J *Phys. Rev. B* **66** 104107 (2002)
203. Harada A, Shimojo F, Hoshino K *J. Non-Cryst. Solids* **353** 3519 (2007)
204. Hoshino K *J. Phys. Condens. Matter* **21** 474212 (2009)
205. Munejiri S et al. *J. Non-Cryst. Solids* **312–314** 182 (2002)
206. Mendelev M I, Belashchenko D K *Inorg. Mater.* **30** 1316 (1994) [*Neorg. Mater.* **30** 1412 (1994)]
207. Belashchenko D K *Russ. J. Phys. Chem.* **75** 81 (2001) [*Zh. Fiz. Khim.* **75** 89 (2001)]
208. Belashchenko D K *Russ. J. Phys. Chem. A* **87** 615 (2013) [*Zh. Fiz. Khim.* **87** 633 (2013)]
209. Kirshenbaum D, Cahill J A *Trans. ASM* **55** 845 (1962)
210. Wang L et al. *J. Phys. Condens. Matter* **15** 777 (2003)
211. Nücker N Z. *Angew. Phys.* **27** 33 (1969)
212. Gerasimov Ya I, Krestovnikov A N, Shakhov A S *Khimicheskaya Termodinamika v Tsvetnoi Metallurgii* (Chemical Thermodynamics in Non-ferrous Metallurgy) Vol. 2 (Moscow: Metallurgizdat, 1961)
213. Gerasimov Ya I, Krestovnikov A N, Shakhov A S *Khimicheskaya Termodinamika v Tsvetnoi Metallurgii* (Chemical Thermodynamics in Non-ferrous Metallurgy) Vol. 4 (Moscow: Metallurgiya, 1966)
214. Döge G Z. *Naturforsch. A* **20** 634 (1965)
215. Rothman S J, Hall L D *J. Metals* **8** 199 (1956)
216. Frohberg G, Kraatz K-H, Wever H, in *Proc. of the 5th Eur. Symp. on Material Sciences under Microgravity. Schloss Elmau, 5–7 Nov. 1984* (ESA SP-222) p. 201
217. Careri G, Paoletti A, Vicentini M *Nuovo Cimento* **10** 1088 (1958)
218. Mikhailova L E et al., Preprint No. 30.87 (Kiev: Inst. for Metal Physics of Ukraine Academy of Sciences, 1987)
219. Itami T et al. *Phys. Rev. B* **67** 064201 (2003)
220. Yamamoto R, Doyama M *Phys. Rev. B* **8** 2586 (1973)
221. Giró A et al. *J. Chem. Phys.* **73** 2970 (1980)
222. Rycerz Z A, Jacobs P W M *Mol. Phys.* **74** 425 (1991)
223. Belashchenko D K *Russ. J. Phys. Chem. A* **82** 1138 (2008) [*Zh. Fiz. Khim.* **82** 1288 (2008)]
224. Lim H S, Ong C K, Ercolessi F *Surf. Sci.* **269** 1109 (1992)
225. Landa A et al. *Phys. Rev. B* **51** 10972 (1995)
226. Landa A et al. *Acta Mater.* **46** 3027 (1998)
227. Landa A et al. *Acta Mater.* **48** 2557 (2000)
228. Bazhirov T T, Norman G É, Stegailov V V *Dokl. Phys.* **50** 570 (2005) [*Dokl. Ross. Akad. Nauk* **405** 325 (2005)]
229. Bazhirov T T, Norman G E, Stegailov V V *Russ. J. Phys. Chem.* **80** (Suppl. 1) S90 (2006)
230. Senda Y, Shimojo F, Hoshino K *J. Phys. Condens. Matter* **14** 3715 (2002)
231. Senda Y, Shimojo F, Hoshino K *J. Non-Cryst. Solids* **312–314** 80 (2002)
232. Verma A K, Modak P *AIP Conf. Proc.* **1349** 549 (2011)
233. Hao Q-H et al. *Int. J. Mod. Phys. B* **27** 1350012 (2013)
234. Yan M et al. *Phys. Rev. B* **47** 5571 (1993)
235. Martynyuk M M *Zh. Fiz. Khim.* **58** 1896 (1984)
236. Hoshino K, Shimojo F *J. Phys. Condens. Matter* **10** 11429 (1998)
237. Shimojo F, Hoshino K, Zempo Y *J. Non-Cryst. Solids* **312–314** 290 (2002)
238. Shimojo F, Hoshino K, Zempo Y *J. Phys. Condens. Matter* **11** 8829 (1999)
239. Shimojo F et al. *J. Non-Cryst. Solids* **250–252** 542 (1999)
240. Pak H M, Doyama M *J. Fac. Eng. Tokyo Univ. B* **30** 111 (1969)
241. Johnson R A *Phys. Rev.* **134** A1329 (1964)
242. Belashchenko D K *Fiz. Met. Metalloved.* **60** 1076 (1985)
243. Belashchenko D K *Zh. Fiz. Khim.* **61** 3166 (1987)
244. Belashchenko D K, Fed'ko A D *Metallofizika* **10** 86 (1988)
245. Waseda Y, Suzuki K, in *Proc. of the Intern. Conf. Science and Technology of Iron and Steel, Tokyo, 1970 Pt. 1* (Tokyo, 1971) p. 392
246. Belashchenko D K, Magidson I A *Izv. Vyssh. Ucheb. Zaved. Chernaya Metallurg.* (3) 4 (1983)
247. Chamati H et al. *Surf. Sci.* **600** 1793 (2006)
248. Belonoshko A B, Ahuja R, Johansson B *Phys. Rev. Lett.* **84** 3638 (2000)
249. Sutton A P, Chen J *Phil. Mag. Lett.* **61** 139 (1990)
250. Koči L, Belonoshko A B, Ahuja R *Phys. Rev. B* **73** 224113 (2006)
251. Dziewonski A M, Anderson D L *Phys. Earth Planet. Inter.* **25** 297 (1981)
252. Koči L, Belonoshko A B, Ahuja R *Geophys. J. Int.* **168** 890 (2007)
253. Mal'tsev I V, Mirzoev A A *Vestn. Yuzhno-Ural'skogo Univ. Ser. Mat. Mekh. Fiz.* (22) 79 (2009)
254. Mal'tsev I V, Mirzoev A A *Vestn. Yuzhno-Ural'skogo Univ. Ser. Mat. Mekh. Fiz.* (9) 76 (2010)
255. Belashchenko D K *Russ. J. Phys. Chem.* **80** 758 (2006) [*Zh. Fiz. Khim.* **80** 272 (2006)]
256. Belashchenko D K, Ostrovskii O I *Russ. J. Phys. Chem. A* **85** 967 (2011) [*Zh. Fiz. Khim.* **85** 1063 (2011)]
257. Belashchenko D K *Geochemistry Int.* No. 6 (2014) (in press)
258. Belashchenko D K, Kravchunovskaya N E, Ostrovski O I *Inorg. Mater.* **44** 248 (2008) [*Neorg. Mater.* **44** 300 (2008)]
259. Belashchenko D K, Kuskov O L, Ostrovski O I *Inorg. Mater.* **43** 998 (2007) [*Neorg. Mater.* **43** 1113 (2007)]
260. Hixson R S, Winkler M A, Hodgdon M L *Phys. Rev. B* **42** 6485 (1990)
261. Saito T, Shiraishi Y, Sakuma Y *Trans. Iron Steel Inst. Jpn.* **9** 118 (1969)
262. Lin Z, Zhigilei L V, Celli V *Phys. Rev. B* **77** 075133 (2008)
263. Lin Z, Zhigilei L V *Appl. Surf. Sci.* **253** 6295 (2007)
264. Al'tshuler L V, Bakanova A A *Sov. Phys. Usp.* **11** 678 (1969) [*Usp. Fiz. Nauk* **96** 193 (1968)]
265. Alfè D, Price G D, Gillan M J *Phys. Rev. B* **65** 165118 (2002)
266. Vočadlo L et al. *Faraday Discuss.* **106** 205 (1997)
267. Aitta A *J. Stat. Mech.* P12015 (2006)
268. de Wijs G A et al. *Nature* **392** 805 (1998)
269. Laio A et al. *Science* **287** 1027 (2000)
270. Alfè D, Gillan M J *Phys. Rev. B* **58** 8248 (1998)
271. Alfè D, Gillan M J *Phys. Rev. Lett.* **81** 5161 (1998)
272. Brazhkin V V, Lyapin A G *Phys. Usp.* **43** 493 (2000) [*Usp. Fiz. Nauk* **170** 533 (2000)]
273. Smylie D E, Brazhkin V V, Palmer A *Phys. Usp.* **52** 79 (2009) [*Usp. Fiz. Nauk* **179** 91 (2009)]
274. Smylie D E, Brazhkin V V, Palmer A *Phys. Usp.* **52** 96 (2009) [*Usp. Fiz. Nauk* **179** 108 (2009)]
275. Zharkov V N *Phys. Usp.* **52** 93 (2009) [*Usp. Fiz. Nauk* **179** 106 (2009)]
276. Bazhanova Z G, Oganov A R, Gianola O *Phys. Usp.* **55** 489 (2012) [*Usp. Fiz. Nauk* **182** 521 (2012)]
277. Belashchenko D K, Mirzoev A, Ostrovski O *High Temp. Mater. Proc.* **30** 297 (2011)
278. Sobolev A, Mirzoev A *J. Mol. Liquids* **179** 12 (2013)
279. Vitek V, Ackland G J, Cserti J *MRS Symp. Proc.* **186** 237 (1991)
280. Ackland G J et al. *Phil. Mag. A* **56** 735 (1987)
281. Polukhin V A, Kurbanova E D, Galashev A E *Russ. Metallurgy (Metally)* **2012** (8) 696 (2012) [*Raspilvy* (3) 15 (2012)]
282. Eletskii A V et al. *Phys. Usp.* **54** 227 (2011) [*Usp. Fiz. Nauk* **181** 233 (2011)]
283. Cherne F J et al. *Modelling Simul. Mater. Sci. Eng.* **12** 1063 (2004)
284. Feller M R, Park H, Wilkins J W *Phys. Rev. B* **81** 144119 (2010)
285. Mendelev M I, Ackland G J *Phil. Mag. Lett.* **87** 349 (2007)
286. Foiles S M, Adams J B *Phys. Rev. B* **40** 5909 (1989)
287. Zope R R, Mishin Y *Phys. Rev. B* **68** 024102 (2003)
288. Li Y et al. *Phys. Rev. B* **67** 125101 (2003)
289. Voter A F, Los Alamos Unclassified Technical Report LA-UR 93-3901 (Los Alamos, NM: Los Alamos National Laboratory, 1993)
290. Sheng H W et al. *Phys. Rev. B* **83** 134118 (2011)
291. Pasianot R, Savino E J *Phys. Rev. B* **45** 12704 (1992)
292. Chen Sh, Xu J, Zhang H *Comput. Mater. Sci.* **29** 428 (2004)
293. Belashchenko D K, Smirnova D E, Ostrovski O I *High Temp.* **48** 363 (2010) [*Teplofiz. Vys. Temp.* **48** 383 (2010)]
294. Smirnova D E, Starikov S V, Stegailov V V *J. Phys. Condens. Matter* **24** 015702 (2012)
295. Smirnova D E et al. *Modelling Simul. Mater. Sci. Eng.* **21** 035011 (2013)
296. Evans R, Greenwood D A (Eds) *Liquid Metals, 1976: Invited and Contributed Papers from the Third Intern. Conf. on Liquid Metals, Bristol, UK, 12–16 July 1976* (Conference Series, No. 30) (Bristol:



- Institute of Physics, 1977) [Translated into Russian (Moscow: Metallurgiya, 1980)]
297. Trunin R F *Phys. Usp.* **54** 397 (2011) [*Usp. Fiz. Nauk* **181** 416 (2011)]
298. Podurets A M *Phys. Usp.* **54** 408 (2011) [*Usp. Fiz. Nauk* **181** 427 (2011)]
299. Landa A et al. *Acta Mater.* **48** 1753 (2000)
300. Lee B-J, Shim J-H *Calphad* **28** 125 (2004)
301. Konishi T et al. *Comput. Mater. Sci.* **14** 108 (1999)
302. Zhang Q, Lai W S, Liu B X *J. Non-Cryst. Solids* **261** 137 (2000)
303. Baskes M I *Mater. Sci. Eng. A* **261** 165 (1999)
304. Asta M, Foiles S M *Phys. Rev. B* **53** 2389 (1996)
305. Asta M et al. *Phys. Rev. B* **59** 14271 (1999)
306. Ruda M, Farkas D, Abriata J *Phys. Rev. B* **54** 9765 (1996)
307. González D J, González L E, Stott M J *J. Non-Cryst. Solids* **353** 3560 (2007)
308. Senda Y, Shimojo F, Hoshino K *J. Phys. Condens. Matter* **12** 6101 (2000)
309. Senda Y, Shimojo F, Hoshino K *J. Phys. Condens. Matter* **11** 2199 (1999)
310. Senda Y, Shimojo F, Hoshino K *J. Non-Cryst. Solids* **250–252** 258 (1999)
311. Senda Y, Shimojo F, Hoshino K *J. Phys. Condens. Matter* **11** 5387 (1999)
312. Senda Y, Shimojo F, Hoshino K *Comput. Phys. Commun.* **142** 401 (2001)
313. Hafner J, Seifert-Lorenz K, Genser O *J. Non-Cryst. Solids* **250–252** 225 (1999)
314. Shimojo F, Hoshino K, Zempo Y *Comput. Phys. Commun.* **142** 364 (2001)
315. Hoshino K, Shimojo F, Zempo Y *J. Phys. Condens. Matter* **12** A189 (2000)
316. Shimojo F, Hoshino K, Zempo Y *J. Non-Cryst. Solids* **250–252** 547 (1999)
317. Shimojo F, Hoshino K, Zempo Y *J. Non-Cryst. Solids* **312–314** 388 (2002)
318. Shimojo F et al *J. Phys. Condens. Matter* **11** L153 (1999)
319. Shimojo F, Hoshino K, Zempo Y *J. Phys. Condens. Matter* **14** 8425 (2002)